

https://dspace.org/

Binary modelling the milling of UG2 ore

Kime, Méschac-Bill Ilunga Kabamba

2015-05-05
http://hdl.handle.net/10539/17616

Downloaded from a DSpace repository. https://dspace.org/

SCHOOL OF CHEMICAL AND METALLURGICAL ENGINEERING
FACULTY OF ENGINEERING AND THE BUILT ENVIRONMENT
UNIVERSITY OF THE WITWATERSRAND, JOHANNESBURG



BINARY MODELLING THE MILLING OF UG2 ORE

by

M.B. KIME ILUNGA

Student Number: 605891

A dissertation submitted to the Faculty of Engineering and the Built Environment, University of the Witwatersrand, Johannesburg, in partial fulfilment of the requirements for the degree of Master of Science in Engineering

Johannesburg, 2014

Declaration

I declare that this dissertation is my own unaided work. It is being submitted for the Degree of Master of Science in Engineering in the University of the Witwatersrand, Johannesburg. It has not been submitted before for any degree or examination in any other University.

Méschac-Bill KIME ILUNGA

…… day of …….. year ……..

Resume

Platinum group elements (PGE) are mineral resources that serve as strategic economic drivers for the Republic of South Africa. Most of the known to date remaining reserves of PGM's in South Africa are found in the UG2 chromite layer of the Bushveld Igneous Complex. Platinum concentrators experience significant losses of valuable PGE in their secondary milling circuits due to insufficient liberation of platinum-bearing particles. The interlocked texture between chromite and the valuable minerals predisposes the PGM ores to an inefficient froth flotation and thereby leads to drastic problems at the smelters. Entrainment of fine chromite is a major problem, so the reduction of fine chromite content in the UG2 ore prior to flotation is therefore crucial. The Council for Mineral Technology (Mintek) has been aiming at improving the secondary ball milling of the Platinum Group Ores by optimisation of the ball milling parameters from the perspective of a preferential grinding of the non-chromite component in the UG2 ore.

To this end, we looked at determining which one amongst speed, liner profile and ball size better controls the energy consumed. Moreover, this work sought at determining which combination of the above variables maximises the reduction of the chromite sliming of UG2 ores. Prior to the experimental work, preliminary evaluations of the load behaviour and power draw under different milling conditions were performed by use of the Discrete Element Modelling (DEM). The DEM was also used to assess the distributions of tumbling mill's impact energy dissipated between balls and between balls and mill shell. The ability of the Discrete Element Modelling (DEM) to match selected experimental scenarios was appraised as well.

The actual ball milling test results indicated that variables, such as mill liner profile and ball size affect the milling efficiency and the size distribution of the products whereas, the mill rotational speed had little to no effect. Use of 45° lifters and small balls enhanced the grinding efficiency. These results agreed fairly well with the DEM simulation predictions.

A model describing the chromite content within the UG2 ore sample as a function of density and particle size was also developed. The model was found to be reliable in the range of data tested and proved to be a strong function of the ore sample density. The particle size was less relevant but nevertheless important.

The UG2 ore was then assumed to be constituted of a binary mixture: chromite and non-chromite components. The kinetics study was then conducted for each individual component, from the feed sizes: -600+425, -425+300, -300+212, -212+150 μm. With regard to the Selection Function ($\mathbf{S_i}$), when comparing the characteristic a values (slope of Si with respect to particle size), faster breakage was obtained for the chromite component, followed by UG2 ore and the non chromite component. The cumulative breakage distribution function ($\mathbf{B_{i,j}}$) values obtained for these two components were different in terms of the fineness factor **γ**. The value of γ was smaller for the chromite component, indicating that the higher relative amounts of progeny fines were produced from the breakage, while the value of γ was large for the non-chromite component, indicating that less relative amounts of fines were produced.

Finally, a matrix model transformation of a binary UG2 ore was developed for a basic closed ball mill-hydrocyclone circuit. The model described satisfactorily the grinding behaviour of the chromite and non-chromite separately. This model is useful for showing effects of the milling of a binary ore on the ball mill circuit output.

Dedication

This work is dedicated to my little sister, Scharon-Rose Kime, and to all other children who live with life-threatening diseases.

Acknowledgements

I wish to express immeasurable gratitude to:

First and foremost, to you Almighty God, Master of time and circumstances, for your great and timely providences you have never ceased to manifest to me. Without your help and comfort, I would not have made it this far;

My supervisor: Professor Michael H. Moys for his positive attitude and guidance. Your powerful contributions and constructive criticisms assisted me enormously in shaping this project. Without your persistent help this dissertation would not have been possible;

Dr Murray Bwalya for assistance in the development of the Wits DEM mill model;

Ms Elizma Haumann and Mr Carl Bergmann, respectively Head and Specialist Consultant in the Comminution Group at Mintek, for creating an appropriate environment for our research work.

Mr Bernard Joja, Manager of the Comminution Group at Mintek is acknowledged for the financial assistance and for allowing the publication of these results.

All Mintek Engineers and Operators for their friendship.

Last but not least, my family and friends for always supporting me

Table of contents

Declaration I

Resume II

Dedication IV

Acknowledgements V

Chapter 1 Introduction 1

1.1 Background 1

1.2 Statement of problem 2

1.3 Research objectives 3

1.4 Dissertation layout 3

Chapter 2 Literature review 5

2.1 Occurrences and treatment of Pt-bearing ores 5

2.2 Entrainment theory 7

2.3 Breakage and Selection Functions: theoretical background 9

2.4. Milling parameters 16

2.4.1 Influence of liner design on minimization of the rate of production of fines in ball milling 16

2.4.2 Influence of mill speed on fines production in ball milling 17

2.4.3 Mill discharge arrangements 18

2.4.4 Influence of ball size on ball milling rates 19

2.5 Mill load behaviour and power draw 20

2.5.1 Torque-Arm Approach 20

2.5.2 Semi-phenomenological approach 21

2.5.3 Energy balance approach 24

Chapter 3 Discrete Element Modelling 26

3.1 Wits DEM Simulator 26

3.2 DEM prediction of mill power draw 27

3.3 Mill load behaviour prediction 28

3.4 Impact spectrum 34

3.5 Conclusion on the DEM simulations 36

Chapter 4 Experimental Equipment and Programme 37

4.1 Introduction 37

4.2 The mill and lifter dimensions 37
4.3 Process control: MINTEK Ball mill 38
4.3 Feed sample preparation 39
4.4 Experimental method 41
4.5 Sample collection 42
4.6 Density measurement 42
4.7 Experimental programme 43
Chapter 5 Effect of operating variables on the ball milling 44
5.1 Effect of the lifter face angle on the mill power draw 44
5.2 Ball size and power draw sensitivity tests 45
5.3 Effect of percent critical speed 47
5.4 Conclusion 49
Chapter 6 Modelling of chromite grade as a function of density 50
6.1 Mineral distributions in the UG2 ore 50
6.2 Chromite distribution in the UG2 50
6.3 Modelling the chromite grade as a function of particle density 54
Chapter 7 Milling Kinetics 57
7.1 Simulation of the grinding process 58
7.2 Results and discussions 59
7.2.1 Determination of the Selection Function parameters 59
Figure 7.2 First-order plots for various feed sizes of UG2 ore ground in a laboratory-scale ball mill 60
Figure 7.3 First-order plots for various feed sizes of Chromite Component ground in a laboratory-scale ball mill 61
Figure 7.4 First-order plots for various feed sizes of Non-Chromite Component ground in a laboratory-scale ball mill 62
7.2.2 Determination of the breakage function parameters 65
7.2.3 Particle size distributions 70
Chapter 8 Matrix modelling of a closed circuit ball milling 78
8.1 Flowsheet setup 78
8.2 Steady-state mass Balancing 79
8.2.1 Mass balance around point 1 79
8.2.2 Mass balance around point 2 80

8.2.3 Mass balance around the cyclone 82
8.3 Matrix representations 85
8.4 Model calibration 87
8.5 Mass Balancing 88
8.6 Computer simulation 88
8.6.1 Ball milling and cyclone classification options for UG2 ores 89
8.6.2 Simulation results 89
8.7 CONCLUSION 91
Chapter 9 Conclusions and Recommendations 92
References 93
Appendices 99
A.1 Wits DEM Simulator Graphic User Interface (GUI) 99
A.1.2 Formatting input and output data 100
A.1.3 Post simulation steps 101
A.1.4 DEM results collection 102
A.2 Mineralogical data 103
A.3 Ball milling test results data 104
A.4 Milling kinetics data 110
A.5 Matrix data 117
A.6 Cumulative weight percents of grinding circuit streams 121

List of figures

Figure 2.1 Flotation recovery in the froth (mineral: black grains) as well as entrainment (gangue slimes: white grains) 8
Figure 2.2 Correlation between silica recovery in different particle size fractions and the recovery of the water (Zheng et al., 2006) 9
Figure 2.3 Variation of S with particle size and graphical procedure for the determination of the parameters (Austin et al., 1984) 12
Figure 2.4 Cumulative breakage function versus relative size (Austin *et al.*, 1984) 15
Figure 2.5 Load behaviour in a mill; definition of toe and shoulder position 18
Figure 2.6 Effect of ball size on the rate of breakage of quartz particles in a laboratory ball mill (Austin *et al*., 1984) 20
Figure 2.7 Rationale behind the torque-arm approach (Moys, 1993) 21
Figure 2.8 Modelling approaches of load behaviour by Moys (1990) 23
Figure 2.9 Modelling approaches of load behaviour by Fuerstenau *et al.* (1990) 24
Figure 2.10 Active charge of the mill (after Morrell, 1993) 25
Figure 3.1 DEM simulations power draw prediction 28
Figure 3.2 Measuring angles using the MB Ruler protractor 29
Figure 3.3 Variations of the toe and shoulder positions of the media charge with the percent fractional speed of the mill 33
Figure 3.4 Impact energy spectra as a function of ball size 35
Figure 4.1 Photograph of the laboratory mill showing the lifters attached to one segment of the mill 38
Figure 4.2 Particle Size Distribution of UG2 ore, chromite and non-chromite 41
Figure 5.1 Experimentally measured power 45
Figure 5.2 Effect of ball size and specific energy consumption on the non-chromite particle size distributions 46
Figure 5.3 Effect of ball size and specific energy consumption on the chromite particle size distributions 47
Figure 5.4 Effect of percent critical speed on the non-chromite particle size distributions (20 mm balls: dot lines and 30 mm balls: solid lines) 48
Figure 5.5 Effect of percent critical speed on the chromite particle size distributions (20 mm balls: dot lines and 30 mm balls: solid lines) 49
Figure 6.1 Measured density as a function of grain size 53
Figure 6.2 Measured chromite grade (abscissa) versus estimated chromite grade (ordinate) 56
Figure 7.1 Schematic representation of the simulator used 59
Figure 7.2 First-order plots for various feed sizes of UG2 ore ground in a laboratory-scale ball mill 60
Figure 7.3 First-order plots for various feed sizes of Chromite Component ground in a laboratory-scale ball mill 61
Figure 7.4 First-order plots for various feed sizes of Non-Chromite Component ground in a laboratory-scale ball mill 62

Figure 7.5 Specific rates of breakage of UG2 ore, Chromite Component and Non-Chromite Component as a function of particle size (Ball diameter = 20 mm) 63
Figure 7.6 Specific rates of breakage of UG2 ore, Chromite Component and Non-Chromite Component as a function of particle size (Ball diameter = 30 mm) 64
Figure 7.6 Breakage Function Distributions for various sizes of UG2 ore 66
Figure 7.7 Breakage Function Distributions for various sizes of chromite component 66
Figure 7.8 Breakage Function Distributions for various sizes of non-chromite component 67
Figure 7.9 Comparison of the Cumulative breakage distribution functions (UG2 ore, Chromite Component and Non-Chromite Component) 69
Figure 7.10a Measured and predicted particle size distributions corresponding to 20 mm balls and feed size: -212 + 150 µm 71
Figure 7.10b Measured and predicted particle size distributions corresponding to 20 mm balls and feed size: - 300 + 212 µm 71
Figure 7.10c Measured and predicted particle size distributions corresponding to 20 mm balls and feed size: - 425 + 300 µm 72
Figure 7.10d Measured and predicted particle size distributions corresponding to 30 mm balls and feed size: -212 + 150 µm 72
Figure 7.10e Measured and predicted particle size distributions corresponding to 30 mm balls and feed size: - 300 + 212 µm 73
Figure 7.10f Measured and predicted particle size distributions corresponding to 30 mm balls and feed size: - 600 + 425 µm 73
Figure 7.11a Measured and predicted particle size distributions corresponding to 20 mm balls and feed size: -212 + 150 µm 74
Figure 7.11b Measured and predicted particle size distributions corresponding to 20 mm balls and feed size: - 300 + 212 µm 75
Figure 7.11c Measured and predicted particle size distributions corresponding to 20 mm balls and feed size: - 425 + 300 µm 75
Figure 7.11d Measured and predicted particle size distributions corresponding to 30 mm balls and feed size: -212 + 150 µm 76
Figure 7.11e Measured and predicted particle size distributions corresponding to 30 mm balls and feed size: - 300 + 212 µm 76
Figure 7.11f Measured and predicted particle size distributions corresponding to 30 mm balls and feed size: - 600 + 425 µm 77
Figure 8.1 Secondary ball milling closed circuit 79
Figure 8.2 Mixing point mass balance 80
Figure 8.3 Continuous ball milling schematic 81
Figure 8.4 Cyclone mass balance 82
Figure 8.5 Cyclone partition curve (Plitt, 1976) 83
Figure 8.6 Showing chromite and non-chromite particle size distributions in the Cyclone overflow stream for different scenarios 90
Figure A.1.1 (a) DEM Simulator presentation 99
Figure A.1.1 (b) DEM software presentation 100

Figure A.1.2 DEM software presentation 101
Figure A.1.3 DEM software presentation 102
Figure A.1.4 DEM frames, particle paths for consecutive frames, position density plots (PDP) (ball diameter = 30mm) 103

List of tables

Table 3.1 DEM simulation parameters 30
Table 3.2 DEM results showing the occupancy of any point in the mill by ball centres during a revolution at 75 % of critical speed 34
Table 3.3 DEM results showing the particle paths for consecutive frames of different liner profiles at 75 % of critical speed 35
Table 3.4 DEM results showing the flow of the grinding media as stills in the simulated ball mill at 75 % of critical speed 36
Table 3.4 Comparison of dynamic angle of repose at various mill speed and liner type 37
Table 4.1 Laboratory operating conditions 45
Table 6.1 Chemical analysis of the UG2 ore sample 55
Table 6.2 Chromite assays grade (in percent) 56
Table 6.3 Measured densities (g per cm^3) 57
Table 7.1 Selection Function descriptive parameters 68
Table 7.2 The primary breakage distribution parameters obtained for short grinding times (ball diameter = 20 mm) 72
Table 7.3 The primary breakage distribution parameters obtained for short grinding times (ball diameter = 30 mm) 72
Table 7.4 Breakage Function descriptive parameters 73
Table 8.1 Grinding circuit mass balance (tons per hour) 92
Table A.2.1 Mintek internal mineralogical terms 107
Table A.2.2 PGM grains mode of occurrence in the UG2 ore sample 108
Table A.2.3 Volume weight percent of PGM grains mode of occurrence in the UG2 ore sample 108
Table A.3.1a Particle Size Distribution of UG2 ore sample using 30 mm balls 110
Table A.3.1b Particle Size Distribution of UG2 ore sample using 30 mm balls 111
Table A.3.2a Particle Size Distribution of UG2 ore sample using 20 mm balls 112
Table A.3.2b Particle Size Distribution of UG2 ore sample using 20 mm balls 113
Table A.4.1 Mass percent of UG2 ore using 30 mm balls 115
Table A.4.2 Mass percent of UG2 ore using 20 mm balls 116
Table A.4.3 Mass percent of the chromite component using 30 mm balls 117
Table A.4.4 Mass percent of the chromite component using 20 mm balls 118
Table A.4.5 Mass percent of the non-chromite component using 30 mm balls 119
Table A.4.6 Mass percent of the non-chromite component using 20 mm balls 120
Table A.5.1 Binary Selection Function Matrix **S** 122
Table A.5.2 Binary Breakage Function Matrix **B** 123
Table A.5.3 Binary Partition Curve Coefficients Matrix **C** 124
Table A.6.1 Cumulative weight percents of grinding circuit streams 125

Chapter 1 Introduction

1.1 Background

South Africa is the world foremost producer of Platinum at 82 tons per year. South Africa has 95.2 % of the PGMs reserves in the world (USGS, 2011). Most of the known to date remaining reserves of PGMs in South Africa are typically found in the UG2 chromitite layer of the Bushveld Igneous Complex. The interlocked texture between chromite and the valuable minerals predisposes the PGM ores to an inefficient froth flotation and thereby leads to drastic problems at the smelters.

Studies on the froth flotation of PGM ores abound and have highlighted the problem brought by a high proportion of chromite in the PGM concentrates. Entrainment mechanism of chromite has been recognized to be mainly responsible for the contamination of PGMs concentrates. This can be explained by the fact that chromite, by nature, is brittle and reduces in size quite rapidly during the milling (Daellenbach, 1985). The chromite rock often has a very low Bond Ball Mill Work Index (about 7 kWh/t) at coarser mesh sizes as compared to fine mesh sizes (less than 106 μm) where the Bond Ball Work Index can increase to values as high as 16 kWh/t. This implies that the breakage rate of chromite at coarser mesh sizes is higher than it is at fine mesh sizes. Some authors have argued that the Bond Working Index of the PGM ores was misled by the chromite brittleness, this has not been proven so far. However, it has been proven that the high density of chromite hinders efficient classification with fine chromite particles sent to regrind while large silicate particles report to the overflow (Mainza, 2004). The classification is preferentially done by means of screen and not hydrocyclone (Bryson, 2004), since the former cuts on the basis of particle size and not density. Bryson (2004) further stated that chromite builds up in the mill and escapes only once it has been milled fine, as it is generally liberated below 200 microns. Care should thus be required when milling PGMs ores with a relatively high content of chromite. Moreover, the PGMs and Base Metal Sulfides (BMS)

frequently reveal a bimodal distribution of grain size. McLaren *et al.* (1982). Penberthy *et al.* (2000) reported that PGMs in the UG2 are known to be tiny inclusions of an average size of 2 – 4 µm and maximum size of 25 µm in the PGM ores. This requires a very fine grinding to liberate all the PGMs locked in silicates which would lead consequently to the chromite being ground even finer.

To solve this problem of chromite in the UG2 concentrates and downstream smelting process, much research has been performed so far, on froth flotation and smelting. Only partial solutions have been found, and the problem of chromite sliming still remains to this day. Few studies however have been interested in milling to address the difficulty associated with the presence of chromite: (Kendal, 2003; Liddell, 2009 and Maharaj, 2011).

In this project we pursue the minimization of the milling energy consumption while at the same time trying to minimize chromite sliming of UG2 ore. Our investigations were carried out in a mill designed and commissioned at the Council for Mineral Technology (Mintek). The batch test work will be used to explore experimentally the following variables: mill speed, liner profiles, and the ball sizes. After a comprehensive analysis of the data, we will be in a position to propose some recommendations for the milling of the UG2 ores.

1.2 Statement of problem

Electricity costs are skyrocketing and it is becoming increasingly important to reduce energy requirements in mineral processing. Grinding is typically the major cost step in mineral processing. To this is added the problem of recovering PGMs from platinum ores. Particularly, UG2 ore exhibits major problems during flotation because of the sliming of chromite. The liner profile type affects undoubtedly the milling efficiency under different grinding conditions. Besides having the role of protecting the mill shell against wear, abrasion, and impact; liners ensure the transfer of the rotational motion of the mill to the grinding media and charge. Good liner design and selection have positive effect on the milling efficiency. It was decided to test

three liner configurations (45°, 75° and square liners) on a ball mill designed at Mintek and to evaluate the milling of UG2 ore under different grinding conditions.

Further, if the UG2 ore is assumed to be comprised of two components (Chromite and Non-Chromite); it is believed that these two components will have different ball milling behaviour. It was therefore decided to conduct a thorough study of the milling kinetics of chromite and non-chromite components within the UG2 ore, in order to establish the preferential grinding conditions of one another component.

1.3 Research objectives

The global expected outcome from this project will be the contribution towards the establishment of optimum ball milling variables for the milling of UG2 ores.

In this regard, this work is aimed at:

- determining which one amongst mill speed, liner profile, ball size better minimise the energy consumed;
- determining also which combination of the above variables well services the reduction of the chromite sliming of UG2 ores.

1.4 Dissertation layout

Besides the introduction, the dissertation has seven chapters.

The second chapter presents an overview of the occurrences of PGMs and their processing to metals. It also looks at sliming-entrainment during flotation and its relation to milling. This work does not cover the flotation. The flotation is only mentioned because it is downstream process following secondary ball milling. In this chapter, we look also at the influence of mill speed, liner profile, ball size on the rate of production of fines. Theoretical power models are reviewed and

discussed in connection with the ball milling. Finally, the Breakage modelling using the Population Balance Model (PBM) is described and discussed.

In the third chapter, the preliminary evaluation of the load behaviour under different milling conditions is conducted by the Discrete Element Modelling (DEM), prior to the actual experimental test work. The DEM is also used to assess the distributions of the dissipated tumbling mills impact energy between balls and between balls and liners, (i.e. the impact spectrum). The ability of Discrete Element Modelling (DEM) to match selected experimental scenarios is appraised as well.

The fourth chapter presents the equipment and methods used in this research work. The details of the sampling procedures used for data collection techniques are also presented.

Chapter Five covers the analysis of the feed and ball milling product samples for different milling conditions. The milling parameters are discussed and the particle size distributions are compared, in order to establish the optimum milling variables.

In the sixth chapter, a comprehensive model that relates the grade of chromite assays in different size fractions of the UG2 ore milling products to the density of the samples is established using basic physics. This model is aimed at reducing the time and cost of chemical analysis procedures. The data collected from the measurement of the sample densities by use of a gas pycnometer are used for this purpose.

In chapter Seven the milling kinetics of the UG2 ore, using the Population Balance Model are discussed. The UG2 ore is assumed to have a binary composition (chromite and non chromite components). Individual milling kinetics of these components are discussed and relevant parameters are determined. In Chapter Eight, a binary matrix model of a closed milling circuit of the UG2 ore is developed. Finally, the conclusion and recommendations are given in chapter Nine.

Chapter 2 Literature review

This chapter presents an overview of the occurrences of PGMs and their processing to metals. It also looks at sliming-entrainment and its relation to milling. It finally looks at the influence of mill speed, liner profile, ball size on the rate of production of fines.

2.1 Occurrences and treatment of Pt-bearing ores

The platinum-group metals (PGMs) form a family of six chemically alike elements. Depending on their density, they can be divided into heavy metals (Platinum, Iridium and Osmium), and light metals (Palladium, Rhodium and Ruthenium). Owing to their excellent catalytic behaviour, corrosion resistance, relative chemical unresponsiveness and high melting points, PGMs have a strong potential for various engineering applications (Kendall, 2003).

There are three main occurrences of Platinum in South Africa: the Bushveld Complex, the Witwatersrand Supergroup and the dunite pipes associated with the Bushveld Complex. The Bushveld Complex is a large layered mafic to ultramafic igneous body formed mainly of chromitite rocks, which consist of approximately 90% of the mineral chromite. In South Africa, all the PGMs are essentially extracted from three significantly dissimilar zones in the Bushveld Igneous Complex; namely, Plat reef, Merensky reef, and UG2 reef (Bryson, 2004). In terms of the platinum group metals (PGM), the UG2 is the most important zone in that it carries significant platinum values throughout the Bushveld Complex. The gangue in the UG2 reef consists to a large extent of chromite and talc. Talc can successfully be depressed during flotation by the addition of polymeric depressants. Chromite, on the contrary, considered to be hydrophilic, could be recovered by entrainment in the water in the flotation concentrates (Mailula *et al.*, 2003). However, the contamination of the PGM concentrates by chromite particles cannot be avoided. The problem of chromite in PGM concentrates is very critical. Chromite belongs to the spinel group which forms stable compounds at temperatures approaching 2000°C (Mckenzie, 1996). A high content of chromite in the concentrate impacts negatively on smelting efficiency. Chromite level of the final product has to be kept as low as

possible because of the downstream processing limitation mentioned above. To do this, chromite should not be milled beyond a certain limit to avoid the slime (Bryson, 2004). We mentioned previously that PGM minerals occur mainly made of minute inclusions; hence, PGM liberation requires fine milling. Chromite instead requires a coarse grinding. The main challenge in the treatment of UG2 ore is to try and limit the content of chromite concentrate PGM to below 2.5 % Cr_2O_3 (Mckenzie, 1996.).

Since the early 70s, many studies have been undertaken for the development of the mining and processing of the UG2 reef. Liddell (2009) conducted a review of the 25 years of UG2 concentrator design and highlighted all the developments over the years including possible future research. He showed that the current standard circuit design to concentrate PGMs from the UG2 ore is a mill-float/mill-float approach designated under the acronym MF2. The motivation of this approach is to perform a first flotation while keeping chromite as coarse as possible. Liddell stated also that recent developments could consider up to three sequential steps, MF3.

Though everyone agrees that chromite content should be substantially reduced in PGM concentrates, there's still no universal limit of chromite content in the concentrate. The primary grinding generally includes a Run-of-Mine (ROM) ball mill, milling occurs in the region of 30-40%-75µm followed by flotation. As in the case of Western Platinum Mine concentrator, MF1 could achieve roughly 73% of PGM recovery with about 3% chromite content in the concentrate at the time it was commissioned (Liddell, 2009). Tailings of the primary flotation are thickened and separated in a hydrocyclone and hydrocyclone underflow is fed to the secondary open circuit ball mill. The feed of the secondary ball mill usually includes large amounts of liberated chromite and silicate-rich particles containing most of the locked platinum. The secondary ball mill grinds relatively finer than 80% -75µm. The Northam Platinum is a good example where the MF2 makes a recovery of approximately 85% with 2% chromite content PGE in the concentrate (Hay and Schroeder, 2005).

2.2 Entrainment theory

Froth flotation relies almost entirely on the degree of hydrophobicity of minerals (Güler and Akdemir, 2011), which is the major criterion of efficiency. The separation performance depends strongly on particle size. Particle size measurements are used to monitor roughly the extent of liberation. Therefore, liberation size should be taken into consideration in the reduction of fine gangue recovery in froth flotation. There should therefore be a balance between the correct size range and the maximum liberation of minerals to be floated as these two requirements are antagonistic as discussed below.

The main mechanism responsible for the gangue recovery in the flotation froth product is "entrainment". The fine particles liberated are conveyed out in a thin water layer surrounding air bubbles, and recovered together with the concentrate, regardless of their degree of hydrophobicity. This is depicted in **Fig. 2.1.** When the particles are overground, the liberation of the valuable mineral is pushed to a high limit; unfortunately, at the same time gangue minerals are also ground finer. Güler and Akdemir (2011) stated that since the gravity effect of tiny particles is negligible they are very susceptible to follow water into the concentrate. It is thus very clear that the degree of entrainment is directly associated with water recovery and fines, and will shrink at coarser grain size. Suffice to say that coarser grinding means that unliberated locked gangue particles are attached to air bubbles by their hydrophobic parts. This results in the concentrate to be contaminated by the gangue minerals. The unliberated locked valuable minerals in the gangue will also follow the tailings stream, causing loss of valuable minerals to tailings.

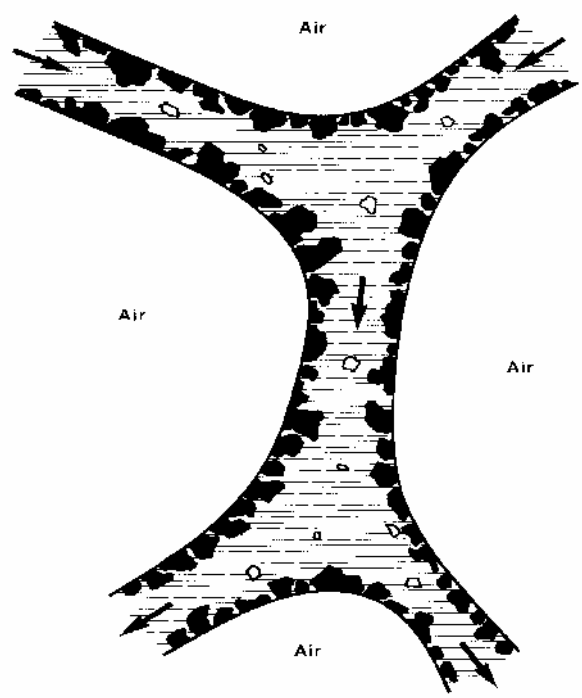


Figure 2.1 Flotation recovery in the froth (mineral: black grains) as well as entrainment (gangue slimes: white grains)

It's widely accepted that the amount of gangue entrained is proportional to the water recovery, according the Kirjavainen's model (Güler & Akdemir, 2011). Zheng et al. (2006) presented also the same result based on the experiments they did on the flotation of silica. The correlation between the silica recovery and water recovery appears to show a non-linear relationship at low water recovery followed by a linear one at higher water recovery, as shown **Fig. 2.2.**

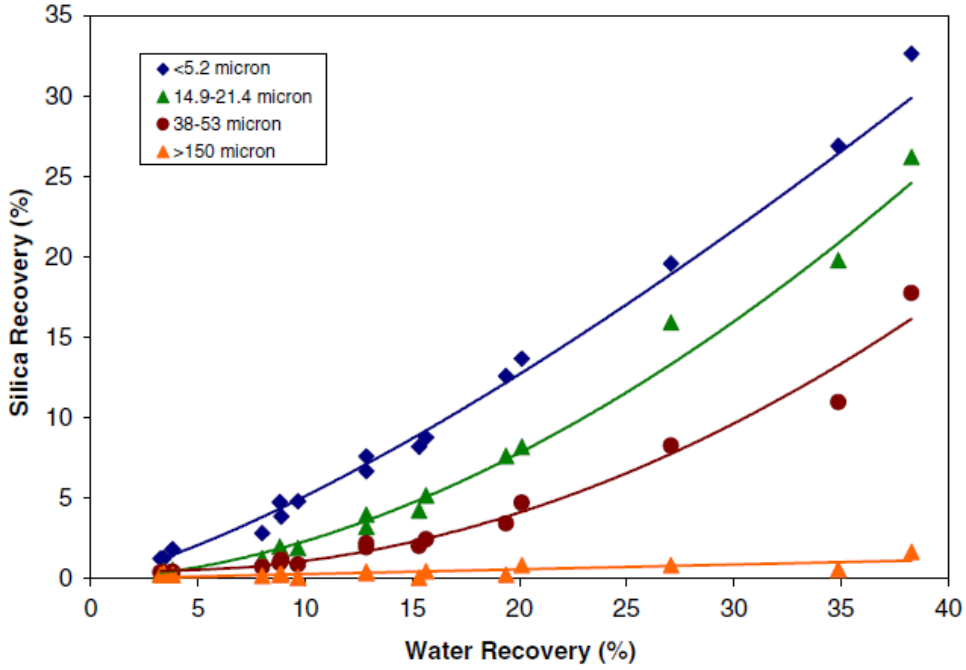


Figure 2.2 Correlation between silica recovery in different particle size fractions and the recovery of the water (Zheng et al., 2006)

2.3 Breakage and Selection Functions: theoretical background

The conventional ball mill model is based on the so-called "Modern Theory of Comminution". In this theory the comminution operation, such as ball milling, is regarded as the sum of many repetitive individual comminution events (Schuhmann, 1960; Lynch *et al.,* 1986) and calls up two probabilistic sets of parameters: the Selection Function S and the Breakage Function B. The former, also called grindability refers to the grinding kinetics of each independent particle. The latter, also called distribution of primary fragments characterizes the size distribution of the resulting fragments following the breakage events. The Austin *et al.* (1984) method for measuring the Selection and Breakage Functions is often used.

2.3.1 Selection Function

It is generally accepted that the disappearance rate of particles through milling is directly proportional to the amount of particles present. In other words, the breakage of a given size fraction of material is assumed to follow the first-order law (Napier-Munn et al., 1996). Although no theory objectively justifies this behaviour so far, this law has proven to be applicable to many materials over a wide range of operation, especially for fine size materials (Austin *et al.*, 1984; Napier-Munn *et al.*, 1996).

Mathematically, the breakage rate of material which is in the top size is given as follows:

$$\frac{dw_i}{dt} = -S_i \cdot w_i(t) \qquad (2.1)$$

The solution of this differential **Eq. (2.2)** is:

$$\log\left(w_i(t)\right) = -\log\left(w_i(0)\right) = \frac{s_i t}{2.3} \qquad (2.2)$$

where $w_i(t)$ and $w_i(0)$ are respectively the weight fraction of size i at times t and 0. S_i is the selection function of the size i. The largest size class is class no 1.

In some cases, deviations due to the material characteristics and grinding conditions used from the first-order can occur (Austin, 1982; Gardner, 1975).

In order to define the variation of the specific rate of breakage function with the particle size, the following empirical model can be used (Austin *et al.*, 1984):

$$S = \frac{a x_i^{\alpha}}{1 + \left(\frac{x_i}{\mu}\right)^{\Lambda}} \qquad (2.3)$$

where x_i is the upper limit of the particle size interval under consideration; the model parameters a and μ are mainly functions of the grinding conditions while α and Λ are material properties.

The parameter α is a positive number normally in the range 0.5 to 1.5. It is mainly dependent on the material properties and does not vary with mill rotational speed, ball load, ball size or mill hold-up over the normal recommended test ranges (Austin and Brame, 1983) for dry milling. The value of a in turn will depend upon mill conditions. The denominator term $Q(x_i)=\frac{1}{1+\left(\frac{x_i}{\mu}\right)^{\Lambda}}$ is actually a correction factor. μ defines the particle size at which $Q(x_i) = 0.5$. Λ is an index that shows how rapidly the rate of breakage decreases as the particle size increases. This leads to the conclusion that the value of $Q(x_i)$ will be 1 for smaller sizes (normal breakage) and less than 1 (abnormal breakage) for particles too large to be nipped and fractured by the ball size in the mill.

Fig. 2.3 shows the first-order breakage law for a given material. The initial straight line portion of the curve which shows the normal breakage behaviour is the area where S has not passed through the maximum. The second portion, area where S has passed the maximum, shows the abnormal breakage behaviour. According to Griffith theory of breakage (Austin *et al.*, 1984) this trend can be explained in that very fine particles are hard to break. This suggests that the breakage rate increases with increase in particle size. However, for too large particles that cannot be correctly nipped and fractured by the balls, the rate of breakage steadily drops and tends to zero.

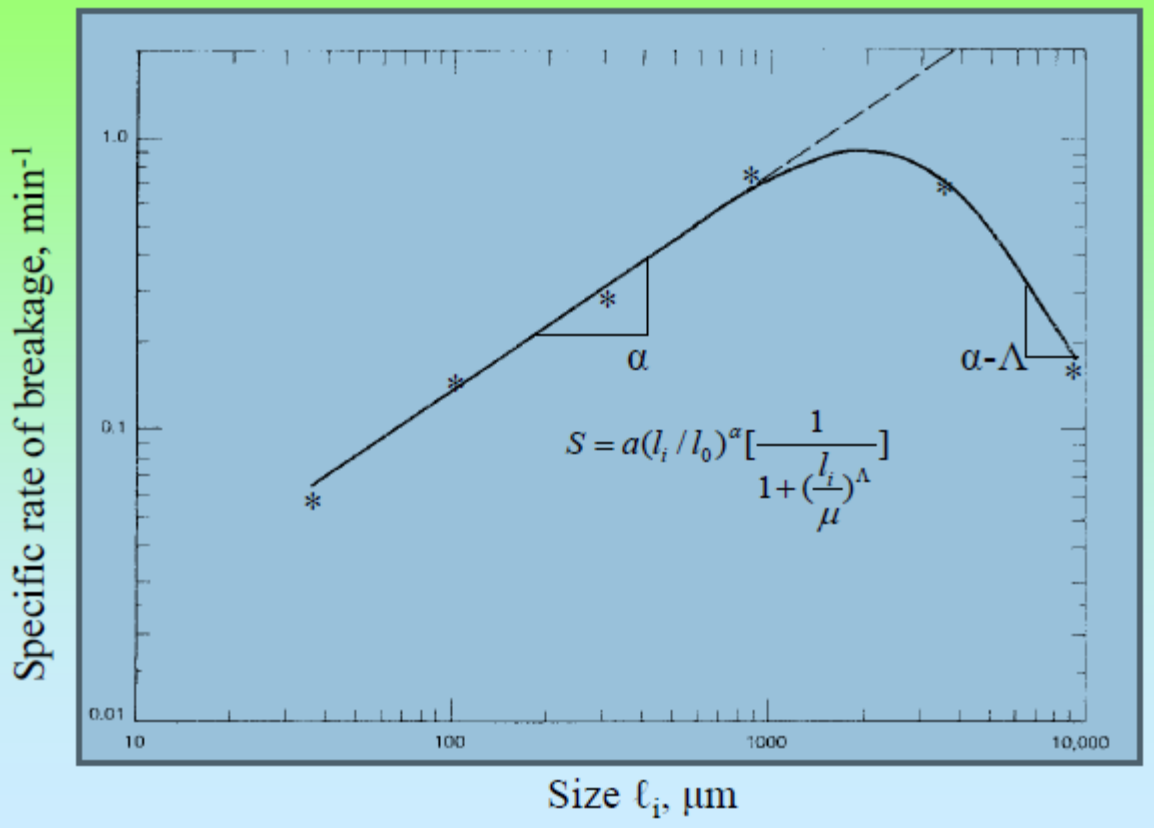


Figure 2.3 Variation of S with particle size and graphical procedure for the determination of the parameters (Austin et al., 1984)

2.3.1.1 Selection Function Scale-up

The Selection Function varies with mill design and operating variables. Therefore, the Si determined from laboratory test works need to be scaled to large-scale mills. Austin et al. (1984) suggested the following equation for the Selection Function scale-up.

$$S=\frac{ax_i^{\alpha}}{1+\left(\frac{x_i}{C_1\mu}\right)^{\Lambda}}C_2C_3C_4C_5 \qquad (2.4)$$

The multipliers C_1, C_2, C_3, C_4 and C_5 are given by

$$C_1 = \left(\frac{D}{D_T}\right)^{N_2}\left(\frac{d}{d_T}\right)^{2} \quad (2.5)$$

$$C_2 = \left(\frac{d_T}{d}\right)^{N_0} \quad (2.6)$$

$$C_3 = \left(\frac{D}{D_T}\right)^{N_1} \quad \text{for D < 3.81 and} \quad (2.7)$$

$$C_3 = \left(\frac{D}{D_T}\right)^{N_1}\left(\frac{D}{3.81}\right)^{N_1-\Delta} \quad \text{for D>= 3.81} \quad (2.8)$$

$$C_4 = \left(\frac{1+6.6J^{2.3}}{1+6.6J_T{}^{2.3}}\right)e^{-c(U-U_T)} \quad (2.9)$$

$$C_5 = \left(\frac{\phi_c - 0.1}{\phi_{cT} - 0.1}\right).\left(\frac{1+e^{15.7(\phi_{cT}-0.94)}}{1+e^{15.7(\phi_c-0.94)}}\right) \quad (2.10)$$

where D is the mill diameter (m), d is the ball diameter (m), J is fractional load volume, U is the fractional void filling and Φ is the mill speed fraction of critical speed. The Subscript T refers to laboratory test mill conditions. N_0, N_1, N_2 and Δ are constants ($N_0 \approx 1$, $N_1 \approx 0.5$, $N_2 \approx 0.1$ to 0.2 and $\Delta = 0.2$ for larger mills).

2.3.2 Breakage Function

The primary breakage distribution function $b_{i,j}$ is the sum of the mass fractions of material broken out of size j that is smaller than the upper size of interval i (Tangsathitkulchai, 2003).

Mathematically

$$b_{i,j} = \frac{\text{mass of particles broken into size i from class j}}{\text{mass of class j broken}} \quad (2.11)$$

The cumulative breakage distribution function $B_{i,j}$ is defined as

$$B_{i,j} = \sum_{k=n}^{i} b_{k,j} \quad (2.12)$$

The breakage function $B_{i,j}$ can be fitted using the following empirical function (Austin *et al.*, 1984)

$$B = \phi_j \left(\frac{X_{i-1}}{X_j}\right)^{\gamma} + (1 - \phi_j)\left(\frac{X_{i-1}}{X_j}\right)^{\beta} \quad (2.13)$$

$$\phi_j = \phi_1 \left(\frac{X_j}{X_1}\right)^{-\delta} \quad (2.14)$$

where δ, ϕ_j, γ and β are the model parameters that depend on the properties for a given ore. The values of *γ* are typically found to be between 0.5 and 1.5 while the values of β range from 2.5 to 5. ϕ_j represents the fraction of fines that are produced in a single fracture event.

The B_{ij} values are said to be normalisable if the breakage distribution function is independent of the initial particle size (Austin et al., 1984). In other words, the fraction which appears at sizes less than the starting size is independent of the starting size. For normalized B values, δ=0 and the B_{ij} can be superimposed on each other.

A graphical illustration of the cumulative breakage distribution function based on **Eq. (2.13)** is given in **Fig. 2.4**. The distribution is in fact a simple weighted sum of two Schuhmann distributions (straight line plots on a log-log scale). The slope of the lower portion of the curve gives the value of γ , the slope of the upper portion of the curve gives the value of β , and ϕ_j is the intercept of the lower portion of the curve at x_j (Austin et. al., 1984).

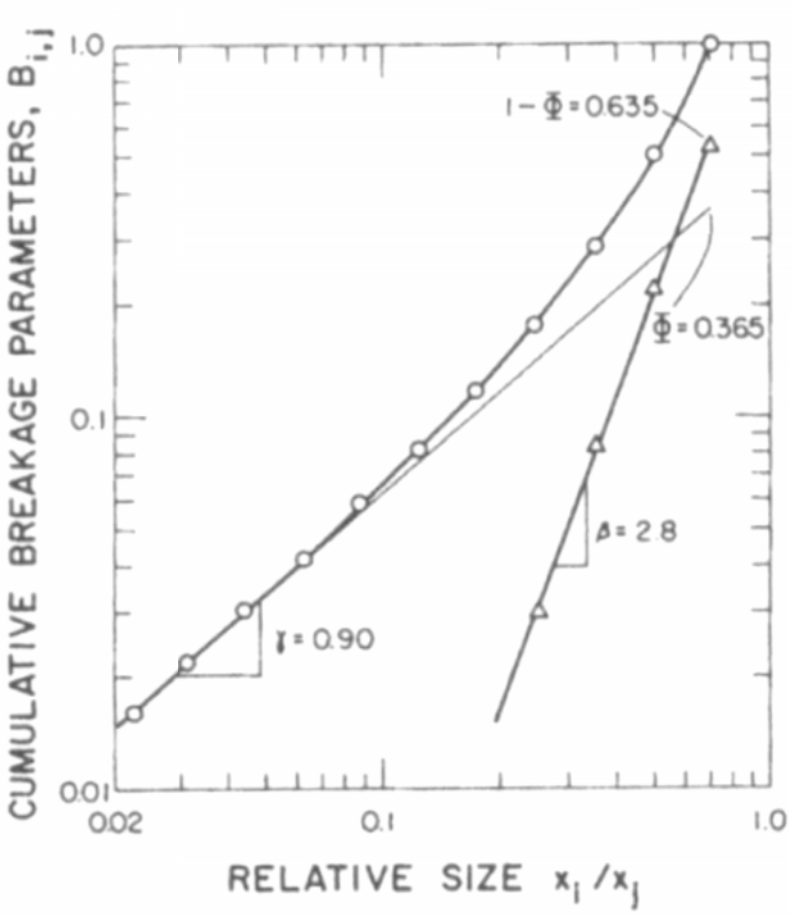


Figure 2.4 Cumulative breakage function versus relative size (Austin *et al.*, 1984)

2.3.3 Batch Grinding Equation

The Selection and Breakage functions are the basis for prediction of particle size distributions for a given ore sample. The Austin *et al.* (1984) procedure which involves a series of laboratory tests in a small mill using a one-size-fraction method is often used. The material is loaded in the mill together with the ball media. Then the grinding is performed for several suitable grinding time intervals. After each interval, the product is sieved. Thus the disappearance rate of feed size material is calculated for the different grinding time intervals.

By performing a population balance at size class i in which the selection and breakage functions are incorporated, one gets:

$$\frac{dw_i(t)}{dt} = -S_i w_i(t) + \sum_{\substack{j=1 \\ i>1}}^{i-1} b_{i,j} S_j w_j(t)\,,\ n \geq i \geq j \geq 1 \qquad (2.15)$$

2.4. Milling parameters

2.4.1 Influence of liner design on minimization of the rate of production of fines in ball milling

The role of liners is to protect the mill against wear, abrasion, and impact, on the one hand, and to transfer the rotational motion of the mill to the grinding media and charge on the other. In view of the role played by liners in a mill, very strong attention should then be paid to the modelling and design of liners to avoid untoward consequences. In their study, Meaders and MacPherson (1964) showed the influence of mill design characteristics on the performance of autogenous mills. They found a noticeable influence of spacing to height ratio variations of the lifter bars on the operation of the mill. Powell (1993) detected that changes in the liner designs caused marked variations in the rate of production of fines and the energy efficiency of a mill. His batch trials were conducted in a 1.8 m autogenous mill, with three different liner profiles (smooth lining, grid lining and lifter bars). He noticed also that the height and spacing (SH ratio) of the lifters were intimately correlated, SH ratios considered were 4.5 and 7.9.

Makokha and Moys (2006) assessed the effect of liner/lifter profile on batch milling kinetics and milling capacity in general using mono-size quartz material of 30 $\times$ 40 mesh (– 600 + 425 μm) as feed. By using cone-lifters, the results indicated a significant improvement of the specific rate of breakage values.

Kalala *et al.* (2007) investigated the influence of liner wear on the load behaviour of an industrial dry tumbling mill used for grinding of coal at Kendal power station in South Africa using the Discrete Element Method (DEM). The results showed that the mill load behaviour was a function of liner wear and liner modifications. The simulated and the measured profiles were

in very good agreement. The DEM was demonstrated to be a powerful tool for the design of grinding equipment.

Powell (2011) used the EDEM software package to perform a 3D DEM simulation of the grinding process. This has allowed the prediction of the rate of wear of lifter geometry and has enabled progressive updating of worn lifter profiles. He finally derived a simplified model for the breakage rate that correlates the liner profile to the mill performance.

2.4.2 Influence of mill speed on fines production in ball milling

Critical speed of the ball mill is defined as theoretical number of revolutions per minute at which the load in contact with the mill shell will just centrifuge assuming no slip between it and the lining of the shell. The South African mills operate at relatively high speeds varying between 70 and 80 percent of critical, whereas autogenous and semi-autogenous mills can operate at speeds as high as 90 percent of critical (Powell, 1988). But where this happens it is probably because slippage is occurring between the load and the liners, and the mill has to be run at a higher speed to overcome this and to rotate the load at an acceptable speed.

Liddell and Moys (1988) examined the factors that affect the load behaviour in terms of positions of the toe and shoulder. The load profile can be approximated by a chord drawn between the toe and the shoulder, forming an angle with the horizontal. The latter is the dynamic angle of repose of the load. The total mass of the load is assumed to be below the chord. The mass of the load acts through its centre of gravity. Among the factors studied were speed and load mill filling levels. The authors have observed that the positions of the toes were affected by changes of speed in excess of 80 % of critical, while the shoulder position was found to be dependent on the speed of the mill and mill filling levels.

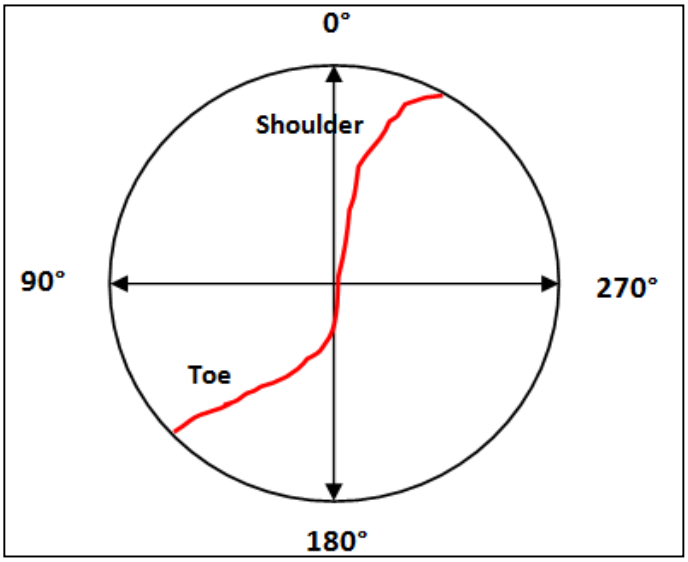


Figure 2.5 Load behaviour in a mill; definition of toe and shoulder position

Liddell (2009) showed that the fineness desired of the PGM products from the UG2 is 80 % – 75 µm and the fines more or less inferior to 20 µm should be avoided, due to the problem of entrainment of chromite in the PGM's concentrates. Unfortunately fines will form in any case.

2.4.3 Mill discharge arrangements

The different mill configurations do not always lead to perfectly mixed pulps, which affects the efficiency of the grinding. Therefore, the choice of the mill discharge arrangement is very important depending on the specificity of the desired product. The mill discharge end acts as a classifier which selectively discharges smaller particles and recycles the larger in the mill load. Fuerstenau *et al.* (1986) studied the material transport in ball mills by considering two typical types of mill discharge arrangements, namely a grate discharge versus an overflow discharge ball mill. They found that the grate discharge was designed to retain oversize material and balls in the mill, by allowing the desired product to discharge. Maharaj (2011) further stated that the grate discharge is favoured where a fairly coarse product is required and when it is necessary to avoid extreme fines in downstream processes. The overflow discharge arrangement for its part is designed for a finer grind. But the difficulty with this latter type of discharge is the creation of

a slurry pool in the conventional secondary open-circuit ball milling circuits for the platinum-rich silicates Bryson (2004). One can simply define the "slurry pooling" as an excessive accumulation of slurry in the mill, around the toe region of the media charge. This leads to a loss of throughput and possibly over-grinding. Hinde and Kalala (2009) indicated that slurry pooling effects with overflow discharge arrangement are enhanced by the large density difference between the silicates and chromite particles. It is therefore clear that the overflow discharge design will encourage the retention of chromite in the mill, thus aggravating the sliming of chromite at flotation.

2.4.4 Influence of ball size on ball milling rates

The selection of the grinding media composition that optimizes the ball milling circuits has been widely studied. Bond (1961) stated that the selection of the grinding media is based on the media size that will just break the largest feed particles. The equation used to determine the largest size ball required is given below:

$$d_B = 25.4 \sqrt{\frac{F_{80}}{K}} \sqrt{\frac{SG \times W_i}{\%C_s \sqrt{3.281 \times D}}} \qquad (2.16)$$

In **Eq. (2.16)** above, d_B is the ball diameter (mm), F_{80} is the 80% passing size of the feed (mm), K is an empirical constant equal to 350 for wet grinding and 335 for dry grinding, SG is the specific gravity of the material being milled, W_i is the Bond Ball Work Index of the ore, % Cs fraction of the critical speed, and D is the diameter of the mill inside liners (m).

Austin *et al.* (1984) conducted dry milling tests of quartz using ceramic balls as grinding medium. The objective was to find the relationship between ball size and rate of breakage at each particle size. The results are presented in **Fig. 2.6**. One can notice that large media are effective for the grinding of coarse particles whereas small media are effective for the grind of small particles. However, it is worth mentioning that use of small balls (20 mm or less) is not

cost effective in most mineral processing operations, because of both the higher cost of small balls and shorter life span as they reach disposable size quicker (Loveday, 2010).

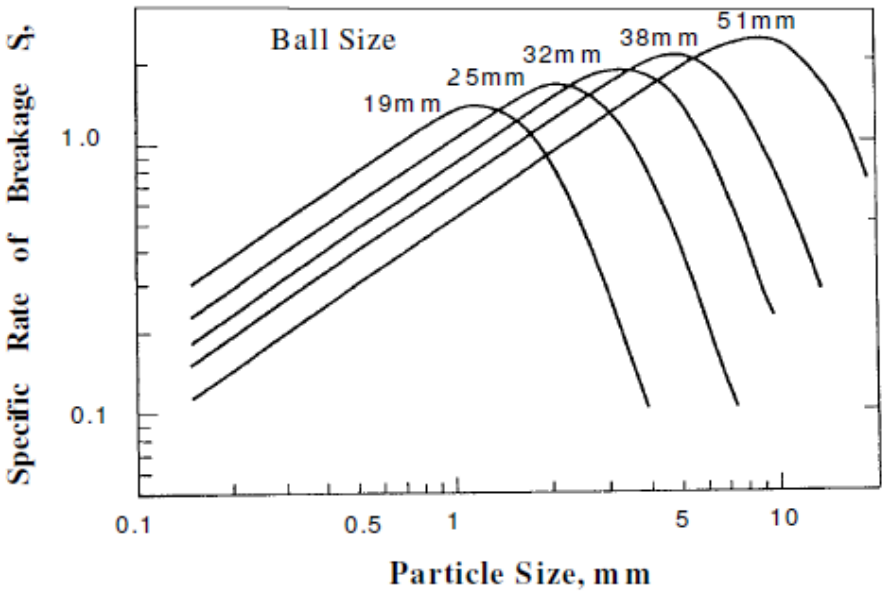


Figure 2.6 Effect of ball size on the rate of breakage of quartz particles in a laboratory ball mill (Austin *et al*., 1984)

2.5 Mill load behaviour and power draw

The efficient management of mill power defines operations profitability, because milling is energy intensive and relatively inefficient in terms of energy consumption. A great number of initiatives have been conducted to find a mathematical conceptualisation that better models power consumption and charge behaviour during the milling process. Some of the models that have been developed so far and have received much attention due to their viability are briefly reviewed.

2.5.1 Torque-Arm Approach

A widely accepted approach involves considering the shape of the load as a rigid circular segment inclined at an angle equal to the dynamic angle of repose of the mill load. In **Fig. 2.7**, the chord joining the toe shoulder of the load and referred to as the surface of the idealised

load is shown. The method assumes that the mass of the load lies below the chord and the centre of gravity of the load through which the load weight acts could easily be established. The torque of the load is derived about the centre of rotation of the mill and finally the mill power is calculated. This model is often referred to as Power Model of Hogg & Fuersteneau (1972) and Harris et al, 1985. The Achilles' heel of this model resides in that the load is considered to be locked inside a circular segment. This assumed load orientation, despite being helpful, is different from the actual load behaviour as revealed by different measurement techniques. This makes models developed based on this assumption of limited accuracy in estimating power drawn by the mill.

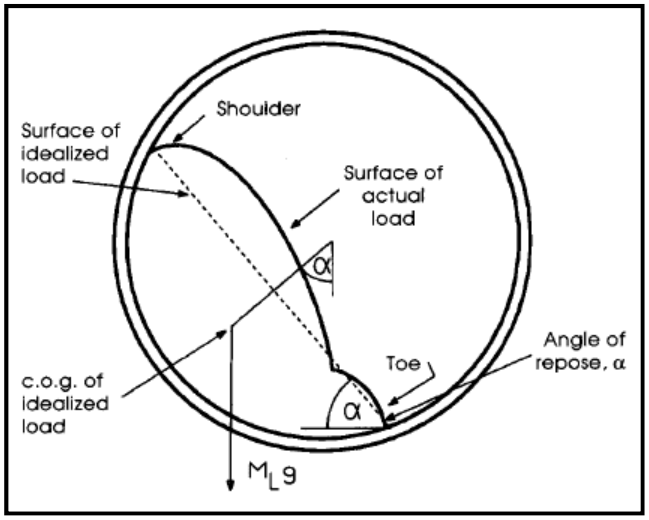


Figure 2.7 Rationale behind the torque-arm approach (Moys, 1993)

2.5.2 Semi-phenomenological approach

Beyond the fact that the mill load under a wide range of operating conditions can be cascading (flow is close to the circular segment shape); the mill load can be also cataracting, or centrifuging, or even some combination of the three. This explains why there exist a number of mill power equations. Among attempts that have shed light so far on the matter, the following may be mentioned:

Moys (1990) developed a power model that assumes that the load is divided into cascading and centrifuging fractions see **Fig. 2.8**. This model combined the conventional torque arm model with a tendency of a fraction of the load to centrifuge at high speed. The model dealt with the effect of lifter bar design, mill speed and filling ratio. Cataracting is ignored.

$$P=K_2 D_{eff}^2 \quad L \quad eff \quad \left(\quad eff \right) \quad eff \qquad (2.16)$$

where K_2 is a constant (actually strongly affected by liner design and slurry properties), ρ_L is the bulk density of the load (kg/m^3), α is the dynamic angle of repose of the load, L is the mill length (m), D is mill diameter (m), N is mill speed (percentage of critical), β is a parameter given a value of 0.937 by Bond (implying that maximum power is drawn at J = 1/2β, = 0,53).

In the formulation of this model, the cascading fraction J_{eff} is modelled using a modified version of the mill power by Bond (1962). J_{eff} is (volume of cascading load) / (volume of mill inside the surface of the centrifuged ore):

$$J_{eff} = \frac{4V_{eff}}{\pi D_{eff}^2 L_{eff}} = \frac{J - 4\delta_c(1-\delta_c)}{1-2\delta_c^2} \qquad (2.17)$$

where $V_{eff,}$ Vc and D_{eff}, reduced volume, centrifuged volume and reduced mill diameter respectively, are given by:

$$V_{eff} = \frac{J\pi D^2}{4} L - V_c \qquad (2.18)$$

$$V_c = \frac{\pi}{4}(D^2 - D_{eff}^2)L \qquad (2.19)$$

$$D_{eff} = (1-2\delta_c)D \qquad (2.20)$$

The centrifuging fraction has thickness $\delta_C D$. Mathematically the following empirical equation is used to model δ_C

$$\delta_c = J^{\Delta_J} e \frac{N_{100} - N}{\Delta_N} \tag{2.21}$$

At low speed; δc=0, the model reduces to Bond's model.

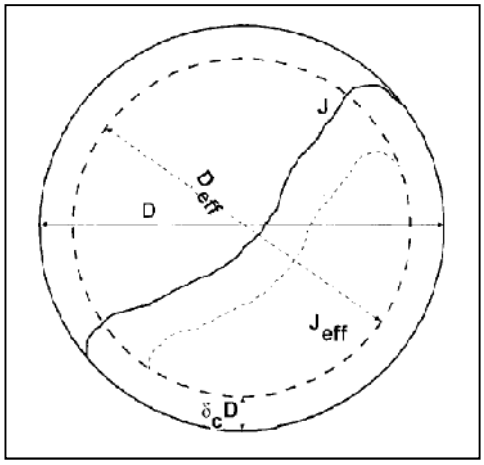


Figure 2.8 Modelling approaches of load behaviour by Moys (1990)

Following the same idea, Fuerstenau et al. (1990) suggested that the load was comprised of a cataracting fraction and a cascading fraction, see **Fig. 2.9**. The latter is approximated by the idealised load profile, as discussed above.

Nevertheless, both Moys and Fuerstenau models are semi-phenomenological, since they are based on a mechanistic description of the load behaviour in conjunction with physically meaningful milling parameters determined from experiments coupled with some empiricism (Wills and Napier-Munn, 2005).

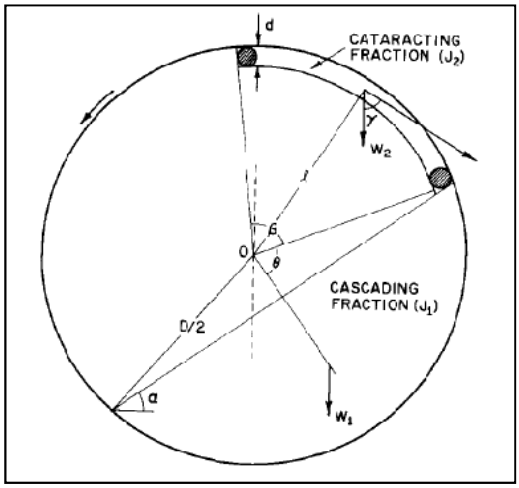


Figure 2.9 Modelling approaches of load behaviour by Fuerstenau *et al.* (1990)

2.5.3 Energy balance approach

Morrell (1993) developed a comprehensive model of power based on the actual motion of charge, using a glass-sided laboratory mill. This model assumes as in the previous ones that the load motion is contained between fixed shoulder and toe angular positions. He further assumed that the active zone of the charge (See **Fig. 2.10** below) occupies the region between an inner radius (r_i) and the mill radius (r_m). The extent of this region is limited by the toe (θ_T) and shoulder (θ_S) of the media charge. The author used the snapshot images to describe particle trajectories. If the angular speed of the balls is N_r units, the power draft of a mill of length *L (m)* and bulk density ρ_L of the charge is given by

$$P_{net} = 2\pi gL\rho_L . \int_{r_i}^{r_m} \int_{\theta_T}^{\theta_S} N_r . r^2 . \cos\theta . d\theta . dr \qquad (2.22)$$

In **Eq. (2.22)**, the variables r_i, r_m, θ_T and θ_S are calculated for given operating conditions using a few empirical correlations. In addition, Morrell carefully included slippage between layers of balls by expressing N_r as a function of radial position *r*. The model can also be used for charges with materials of different densities. The crescent-like shape of the load which is the foundation of Morrell's model of mill power could be the main reason for such a success. This model has

been applied successfully to many Australian mills, mainly with a high *D*/*L* ratio and with mill speeds near 75 % of critical speed. Moys and Smit (1998), stated that the model needed testing on tube mills (low *D*/*L*) and mills operating at high speed (e.g. 90 % of critical as is typical in the South African gold industry; Powell *et al.*, 2001).

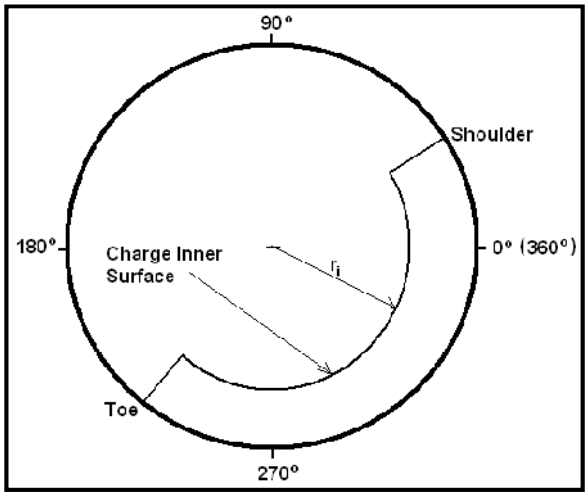


Figure 2.10 Active charge of the mill (after Morrell, 1993)

The power models are numerous in the literature and the list above is not exhaustive.

This Chapter has highlighted the main findings published in the field of wet ball milling. This included a review of ball milling variables, milling power models and milling kinetics theory. Milling kinetics are often time consuming and simulation can be used to reduce the amount of time taken in experimental programme. In the next chapter, DEM numerical method will be used to reduce number of the milling variables and the milling test time.

Chapter 3 Discrete Element Modelling

Discrete element method modelling (DEM) has proven over many years to be a powerful tool for design and optimization within the mineral processing industry. Examples are numerous, where results obtained from the DEM simulations were valid over a wide range of mill operating conditions: Cundall *et al*. (1997), Kalala *et al*. (2007), Powell *et al*. (2009). Work has been done at Wits to investigate how mill rotational speed, liner type and ball size affect the energy consumption of an experimental laboratory scale ball mill at Mintek. Moreover, the DEM simulations results were intended at reducing number of variables to take into account in actual ball milling tests. The DEM simulation was configured to match the environment inside the laboratory scale ball mill at Mintek, using the parameters given in **Table 3.1**.

Table 3.1 DEM simulation parameters

Parameters	Ball-Ball contact	Ball-Wall contact
Coefficient of friction	0.4	0.5
Coefficient of restitution	0.4	0.5
Normal stiffness (kNm^{-1})	400.0	400.0
Shear stiffness (kNm^{-1})	300.0	300.0

3.1 Wits DEM Simulator

This section presents the simulator used for our DEM investigations. The procedure was used to identify trends that would help select the best milling configuration. **PFC^{3D}** (Particle Flow Code in 3 Dimensions) is a generalised code for DEM purposes developed by the Itasca Consulting Group. Murray Bwalya has developed a DEM software for the simulation of load behaviour in mills. The software offers many options for designing mills with variable liner profiles, mill

speed, mill dimensions, load volume, etc. Details on the Wits DEM Simulator Graphic User Interface (GUI) are presented in **Appendix A.1**.

3.2 DEM prediction of mill power draw

The effects of liner profile, mill speed and ball size on the mill power draw were analysed. The DEM prediction power draw results in **Fig. 3.1** show that the power draw was sensitive to liner profile types at chosen mill speed. The power draw increased with increase in rotational speed at lower percent critical speed; but quickly decreased beyond 70-80 % of the critical speed. The highest power draw corresponded to 80 % of critical speed, which is in the speed range that most PGM mills are operated. The decrease in power draw with higher speeds was mainly due to that large proportion of the mill load was cataracting at higher speed. This will be further elaborated by examining the position density plot (PDP) snapshots and the particle paths for consecutive frames. Additionally, the power draw was higher for the mill simulated with small balls. It is obvious that this was due to an increase in the surface area.

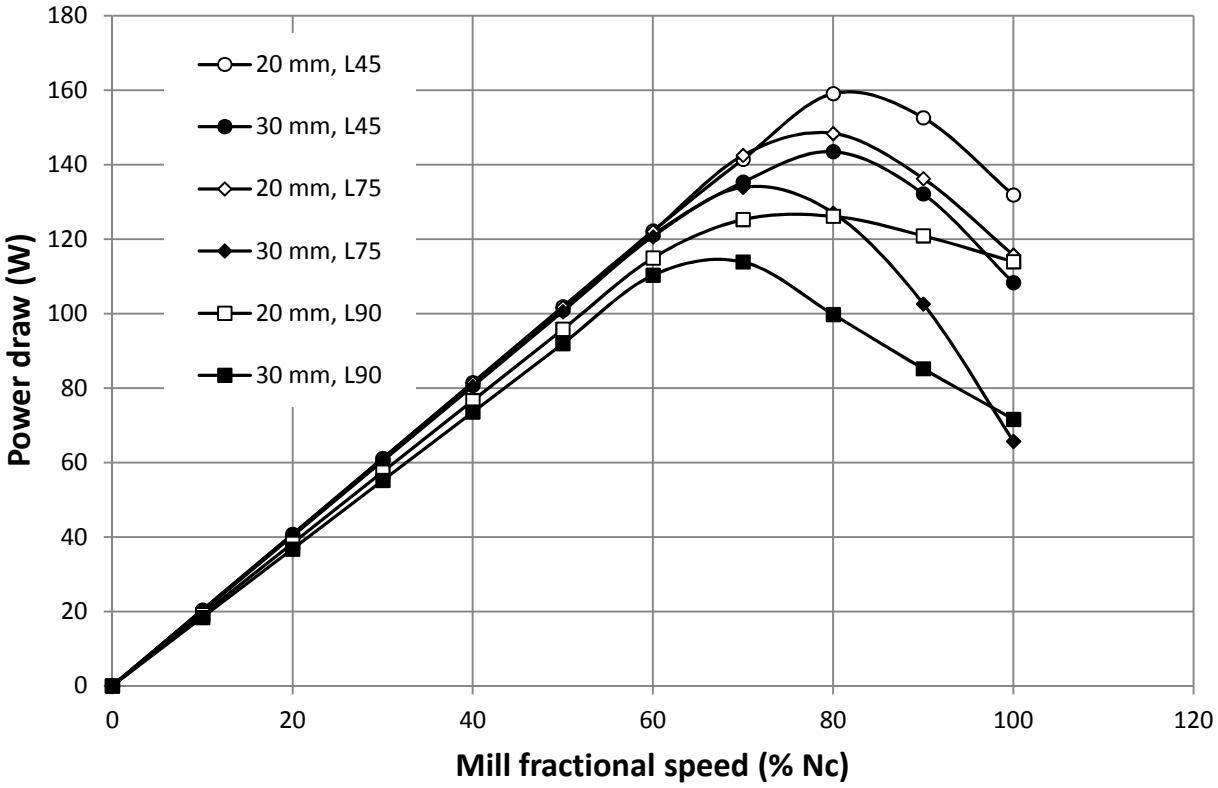


Figure 3.1 DEM simulations power draw prediction

3.3 Mill load behaviour prediction

The statistical record of ball positions referred to as position density plots (PDP) of balls in motion were analysed for the three liner profile scenarios. This was done in order to determine whether different ball sizes exhibited different tumbling behaviours and motions at three different liner profiles and different mill rotational speeds inside the mill. The first two mill revolutions were not important because the mill motion was still unstable. Therefore, the PDP analyses were considered for 3 consecutive mill revolutions, starting at the third revolution when the mill was running at steady state conditions.

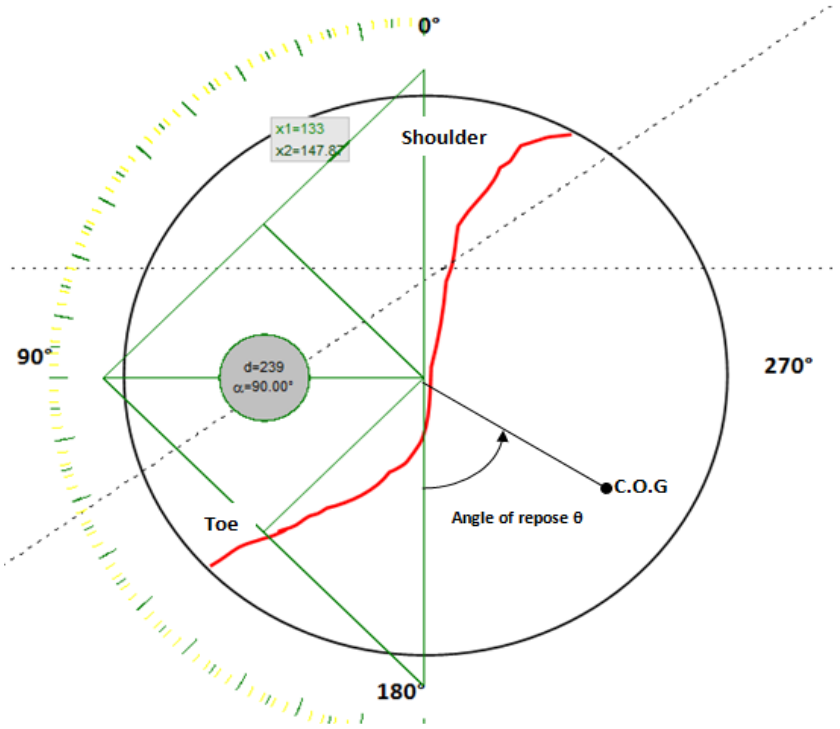
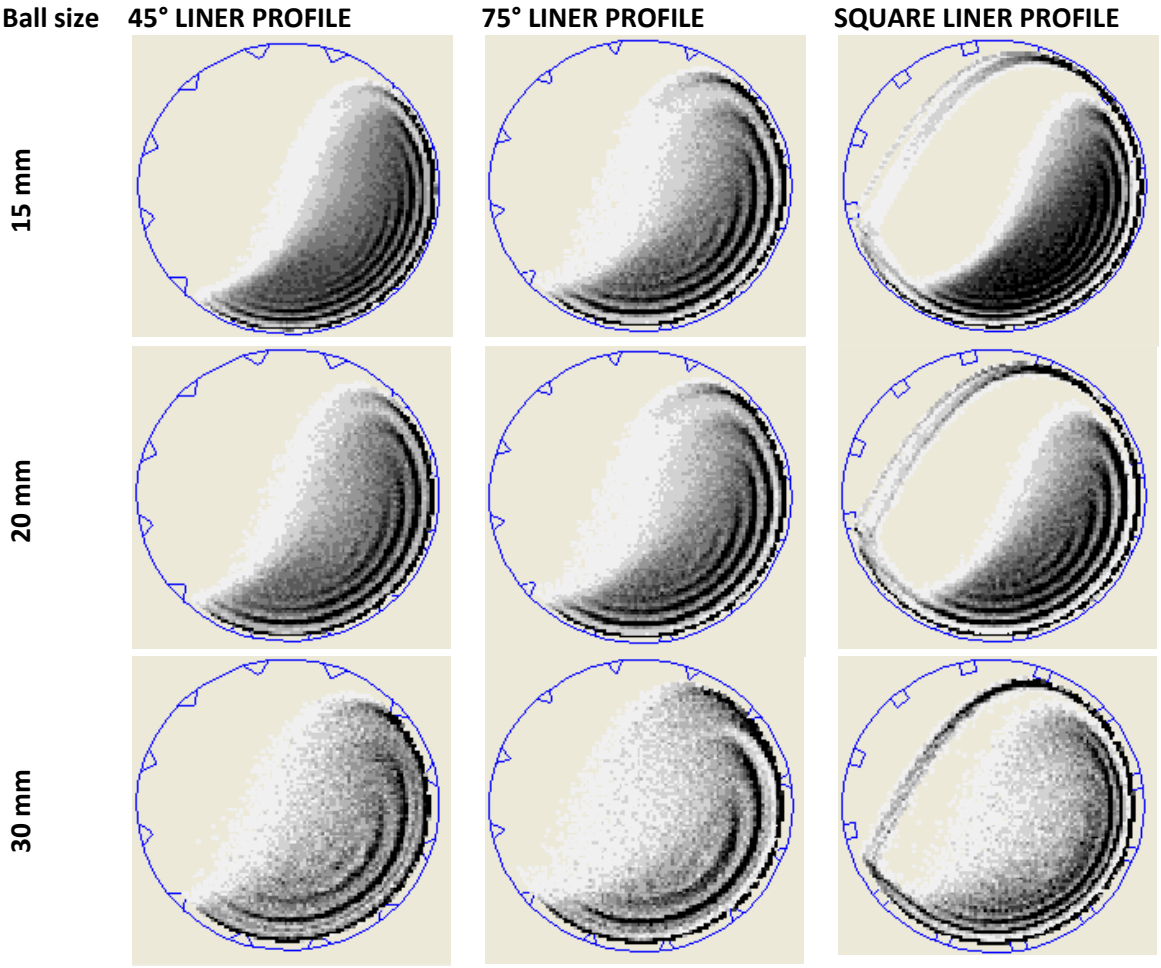


Figure 3.2 Measuring angles using the MB Ruler protractor

For each and every frame retained for analysis, a set of axes was superimposed onto the corresponding photograph. With the help of an electronic protractor, as shown in **Fig. 3.2**, the key angular positions (dynamic angle of repose, toe and shoulder positions) of the charge were accurately measured with the 12 o'clock position being 0° (reference) while the 9 o'clock position was used as 90°. The table below represents the DEM simulation showing the occupancy of any point in the mill by ball centres during a revolution at 75 % of critical speed. The migration of particles from the cataracting to the cascading zone and vice-versa can be appreciated. Individual motions of particles can also be studied in details from this type of information. Additionally, the dynamic angle of repose, the shoulder and toe positions can be accurately measured. It can be seen that with the mill simulated with 45° liner profile, part of the load and the media is thrown far and impact on the mill shell at lower angular displacement. In other words, the energy is returned to the mill as a result of balls being projected to the mill shell. This explains why the mill simulated with 90° liner drew less power.

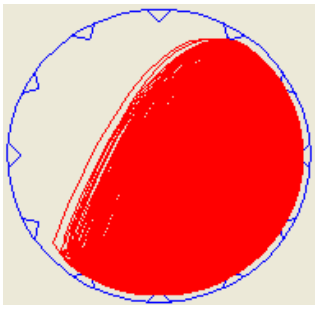
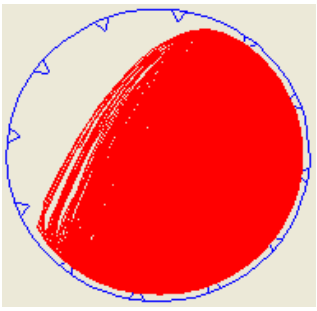
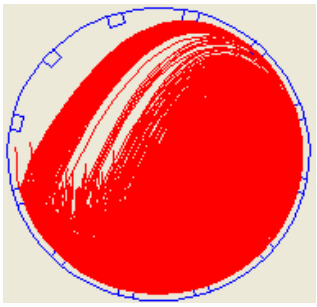
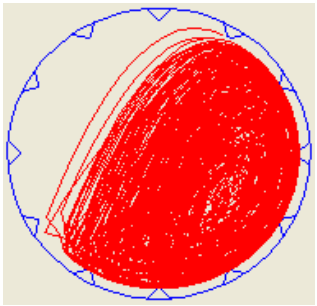
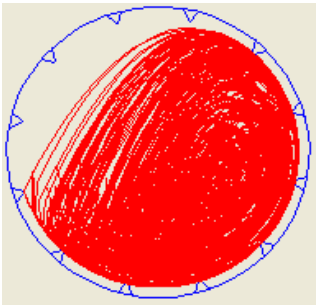
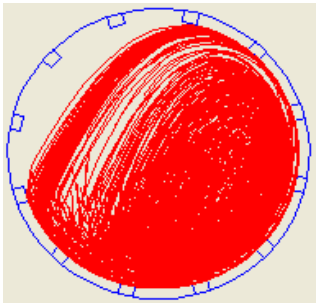
Table 3.2 DEM results showing the occupancy of any point in the mill by ball centres during a revolution at 75 % of critical speed



The power draw trends in **Fig. 3.3** can also be explained by examining particle paths for consecutive frames, as shown in **Table 3.3**. It is obvious that by using of 90° liner profile, cataracting of balls onto the liners is unavoidable. Therefore, with further increase in mill rotational speed, the problem will be enhanced. It can be seen in all the cases that the shoulder position decreases as the ball diameter increases from 15 mm to 30 mm. Since the ball filling was kept constant (J = 30%), the diminution of the shoulder position can be explained by the sliding of the load charge. The particle paths of balls for one full revolution are given in **Table 3.3**. It can be seen that small balls were lifted higher than the large balls explaining why the

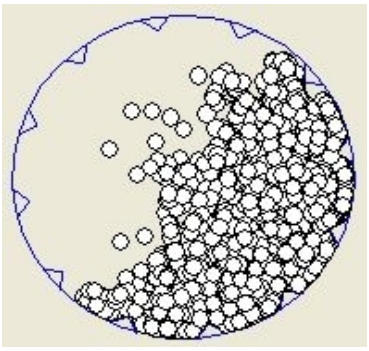
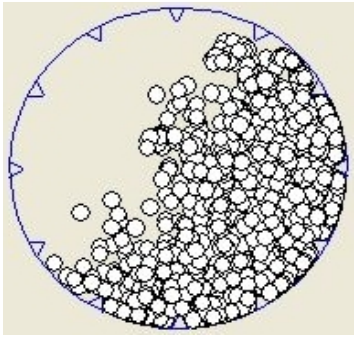
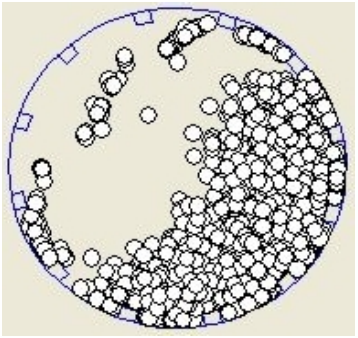
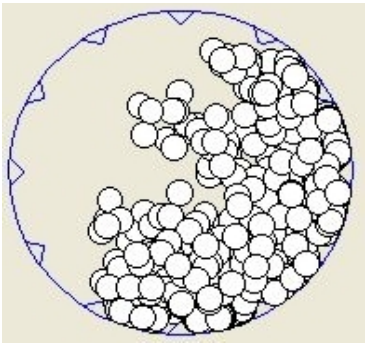
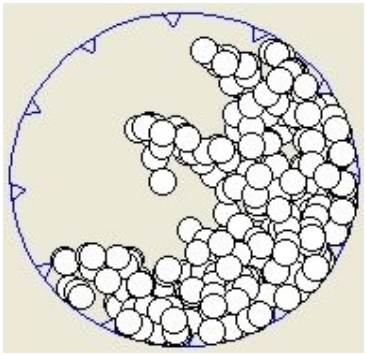
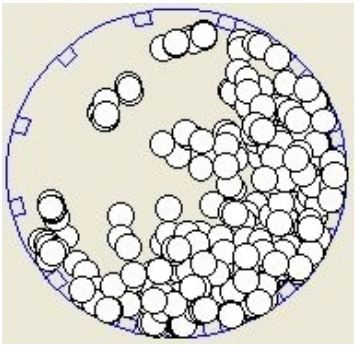
power draw obtained when we simulated the mill with 20 mm balls is larger than when we simulated the mill with 30 mm balls.

Table 3.3 DEM results showing the particle paths for consecutive frames of different liner profiles at 75 % of critical speed

	45° liner profile	**75° liner profile**	**90° liner profile**
20 mm balls			
30 mm balls			

The movement of the grinding media can also be represented by still images, as shown in the **Table** below.

Table 3.4 DEM results showing the flow of the grinding media as stills in the simulated ball mill at 75 % of critical speed

	45° liner profile	**75° liner profile**	**90° liner profile**
20 mm balls			
30 mm balls			

The comparison of dynamic angle of repose at various mill speed and liner type is shown in **Table 3.4**. For all the three liner types considered, larger balls exhibited higher dynamic angles of repose, as compared to smaller balls. This is explained in that there's a large dynamic (slippage) between large ball layers as compared to smaller ones. The dynamic angle of repose increased also with increase in mill speed.

Table 3.4 Comparison of dynamic angle of repose at various mill speed and liner type

Liner type	45° liner profile			75° liner profile			Square liner profile		
Ball size (mm)	65% crit.	70% Crit.	75% crit.	65% crit.	70% Crit.	75% crit.	65% crit.	70% Crit.	75% crit.
15	57.1	60.5	65.0	58.5	60.1	62.9	46.4	48.3	68.1
20	58.8	64.6	65.0	59.1	65.4	66.6	56.6	61.2	71.3
30	59.3	65.1	65.0	60.2	63.3	63.4	65.8	66.6	72.9

The toe and shoulder positions were also plotted against the mill fractional speed, as shown in **Fig. 3.3**. This shows that the toe and shoulder positions were less sensitive with change in mill speed and liner profiles.

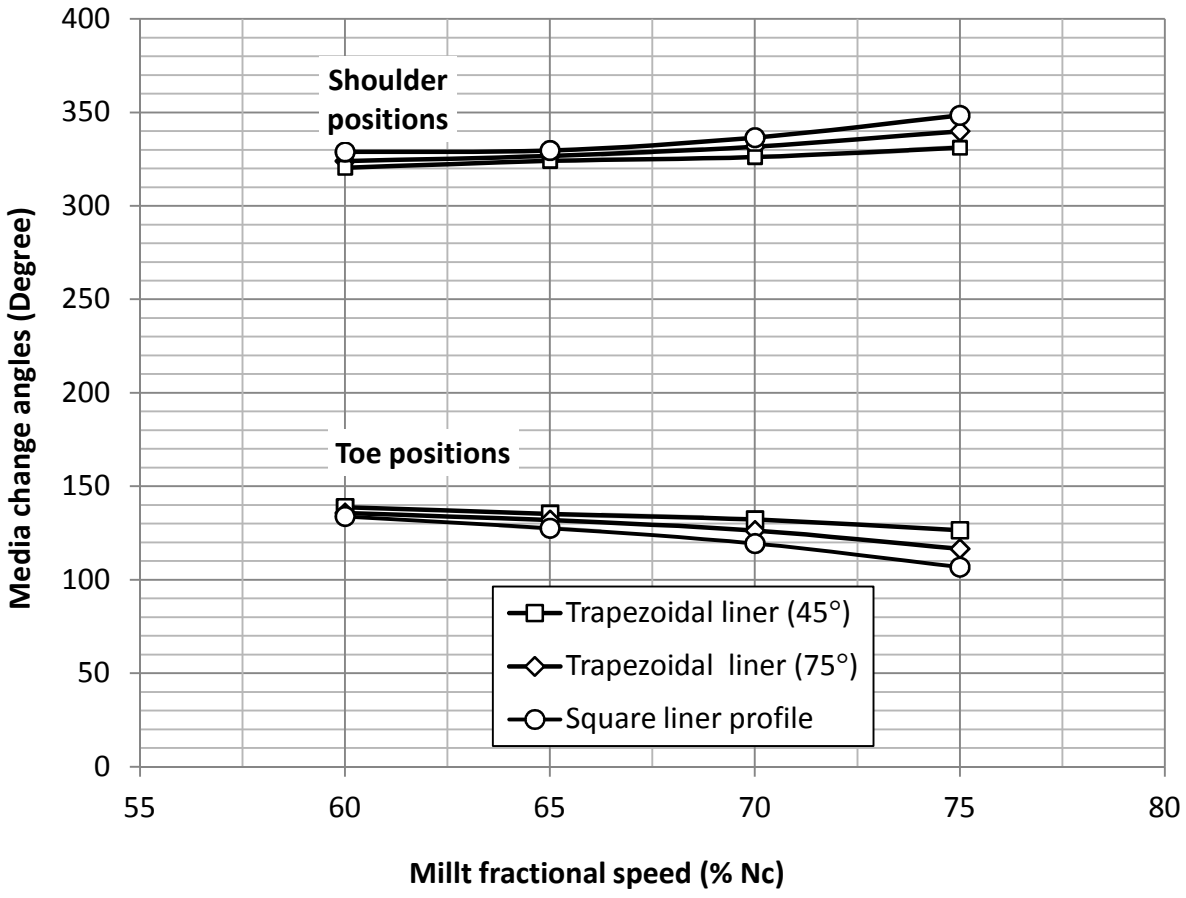


Figure 3.3 Variations of the toe and shoulder positions of the media charge with the percent fractional speed of the mill

3.4 Impact spectrum

The other valuable information that the DEM can deliver is the distribution of the dissipated tumbling mills impact energy between balls and between ball and liner. This is very useful to determine the kinetics of the comminution process in the mill and to estimate the grinding effectiveness (King, 2000). Agrawala *et al.* (1997) stated that tumbling mill events are efficient when they occur in a region of the mill where the probability of finding an ore particle is higher. Moreover, impact energies should be in the range that can break the ore particle. Very high energy impacts are not profitable to the mill as part of the impact energy generated is wasted, causing rather ball and liner wear than the grinding itself. The impact energy spectra or the distribution of impacts energy is obtained by plotting the collision frequency against the collision intensity of ball media on the mill shell**.** It can be seen in **Fig. 3.4** that impact energy events are located in the lower energy regions for the mill simulated using 20 mm balls, when compared with 30 mm balls. This was observed at any speed and liner-type considered. The impact energy events were also similar for different mill speeds and ball sizes. This means that mill speed doesn't affect the impact energy spectra significantly. The impact energies were also found to be proportional to the steel ball size weight. The maximum impact energy recorded when using 20 mm balls and 30 mm balls were in the following ratio:

$$\frac{m_{d_{20}}}{m_{d_{30}}} = \frac{\rho \frac{\pi}{6} 20^3}{\rho \frac{\pi}{6} 30^3} = \left(\frac{20}{30}\right)^3 = \frac{8}{27}.$$

The density of impacts energy d_i (J) is the scalar product of the frequency of collisions and the impact energy intensity. The density of impacts energy expresses the total mill impacts energy at different energy classes. It is expressed as follows:

$$d_i(J) = f_i I_i \qquad (3.1)$$

where I_i is the impact energy (J) and f_i is the frequency (Hz) of collisions

This function can be conveniently represented in its cumulative form as follows

$$D_j(J) = \sum_{i=1}^{j} f_i I_i \qquad (3.2)$$

$D_j(J)$ gives an idea of the ball milling with accumulation of tumbling impacts. **Fig. 3.4** shows also the plot of the cumulative impact energy against the impact energy for both ball sizes. The mill rotational speed was varied, while the ball filling (J = 30 %) was kept constant. The total cumulative impact energy decreased essentially due to a reduction in events of high energy impact. Larger balls exhibited more impacts energy as compared to smaller ones.

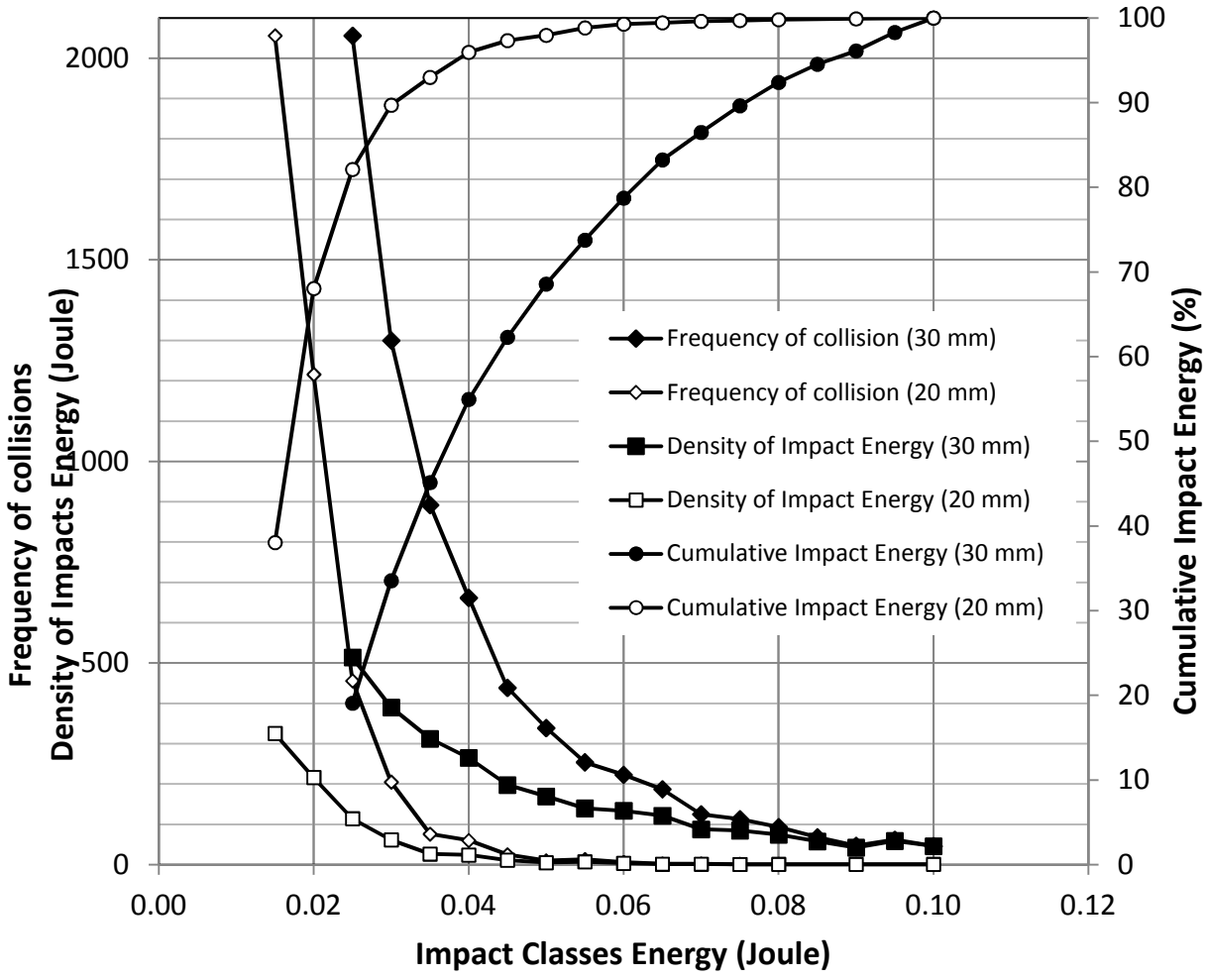


Figure 3.4 Impact energy spectra as a function of ball size

3.5 Conclusion on the DEM simulations

In tumbling ball mills, parameters affecting the dynamic motion of balls, such as liner face angle and mill rotational speed are very important. Moreover, the dynamic motion of balls affects the mill power draw and the distribution of the impact forces. The DEM simulations did not involve the actual ore samples. The ball charge filling percentage was kept constant and equal to 30 % of the total volume of the ball mill. For all the three liner face angles considered in this work, there was not a direct correlation between the power draw, the toe and shoulder positions. The peak power draw was found to have occurred at different toe or shoulder oppositions for different liner types. The mill simulated with 90° liner face angle drew the lowest power, due to a significant proportion of balls cataracting. Some of their momentum was imparted to the mill shell resulting in a loss of power. Besides having the role of transferring rotational motion of the mill to the grinding media and charge, liners should protect the mill against wear, abrasion, impact, etc. The actual wet ball milling tests described in Chapter 4 involving the PGM ore sample were then conducted with trapezoidal liner types (45 deg. and 75 deg. face angles). On the other hand, the load behaviour and mill power draw were found to be strong functions of ball size. However, since the DEM simulation did not take into account material properties, such as particle strength, these findings need to be backed by actual experiment involving an ore sample.

Chapter 4 Experimental Equipment and Programme

4.1 Introduction

This chapter describes all equipment and methods that were used to generate the experimental data analysed and discussed in chapters that follow. Sampling procedures and size-by-size assay analyses are also described.

4.2 The mill and lifter dimensions

An experimental laboratory scale ball mill designed and built at Mintek was used in this project. The ball mill measured 0.4 m in diameter with four independent sections of length 0.2 m each, one of which is shown in **Fig. 4.1**. It allows the use of variable liner types along the mill axial length. It was fitted with 12 lifters spaced circumferentially around the mill shell, with an average spacing-to-height ratio (S/H) of ± 0.6. It was driven by an asynchronous motor rated with power close to 10 kW, connected to a variable speed gear-box, provided with accurate measurement devices for the torque and the mill load with respect to time by means of load cells strategically placed under the mill bearings. All these key-parameters were connected to a computer data acquisition system. Additionally, in open continuous circuit, the mill allowed two discharge configurations, either grate or overflow discharge.



Figure 4.1 Photograph of the laboratory mill showing the lifters attached to one segment of the mill

4.3 Process control: MINTEK Ball mill

The Measurement and Control Division within Mintek has developed an advanced stabilisation and optimisation process control platform, StarCs that integrates the Mintek Ball Mill control system. All the key-parameters were connected to StarCs, the computer data acquisition system that helped to stabilise the mill rotational speed. The torque was instantaneously and accurately measured. The power draw, the energy consumption and the specific energy consumption, referred to as outputs were calculated automatically. Upon launching StarCs, a self-explanatory and straightforward window pops up with several functionalities, in which the "form text box" is to be filled with information pertaining to milling conditions. StarCs applies the following equations:

$$P=\frac{2}{60} \qquad (4.1)$$

$$E=\frac{2}{60t}\frac{}{3600} \qquad (4.2)$$

where:

P: Gross power, kW

E: Energy Consumption, kWh/ton

N: mill rotational speed, rpm

T: mill torque, Nm

M_L: mill load, kg

t: milling time, second

Eq. (4.2) shows that the power and the torque beam are closely related. To calibrate the mill power, the torque beam was regularly calibrated to ensure that information displayed on the gear-box was the real representation of torque exerted by the charge in the mill. To this end, a known weight suspended on a rod at a known distance was used. The net torque and net power at the particular speed were obtained as follows:

Net Torque = Gross Torque − Zero load Torque (4.3)

Net Power = Gross power –Zero load power (4.4)

Zero load power and Zero load Torque are obtained when the mill is running without any charge.

4.3 Feed sample preparation

The PGM ore used in the actual test work was obtained from the feed to the primary mill (run of mine) at Lonmin's Marikana Mine. It was then crushed down in closed circuit with a 600 µm limiting screen, using a Koppern High Pressure Grinding Roll (HPGR). The ball mill feed content mass was calculated using following Equations:

$$M_{feed} = V_{mill} \times \rho_{bulk} \times f_c \quad (4.6)$$

The f_c value was calculated from **Eq. (4.7)** by first setting the slurry filling U.

$$f_c = \left[\frac{\text{mass of powder}}{\text{powder density}} \right] \times \frac{1.0}{1-\varepsilon'} \quad (4.7)$$

$$J = \left[\frac{\text{mass of ball}}{\text{ball density}} \right] \times \frac{1.0}{1-\varepsilon} \quad (4.8)$$

$$U = \frac{f_c}{\varepsilon \times J} \quad (4.9)$$

Where:

Slurry filling (U) is the fraction of the spaces between the balls at rest which is filled with slurry. Slurry volume fraction (fc) is expressed as the fraction of the mill volume filled by slurry bed using a slurry bed porosity **ε**. Ball filling (J) is expressed as the fraction of the mill volume filled by the ball bed at rest, assuming a bed porosity **ε'**. In this work, the slurry bed porosity and ball bed porosity were chosen equal to 0.4 that is the conventionally formal bed porosity.

To prepare samples of similar feed size distribution, conventional splitting methods were used. A total of 500 kilograms of the UG2 ore sample, previously ground with an HPGR was split into 7.9 kg batches using the Jones Riffle sampler. A rotary splitter was then used to get 3 sub-samples of 102.7g each out of one randomly chosen batch, for particle size analysis. Through this iterative process, it was possible to obtain 62 samples of similar size distribution in the margin of

experimental errors inherent to the sampling method. This was determined using a root 2 series of sieves mounted on a sieving machine. The feed d_{80} size was 390 µm as shown in **Fig. 4.2**.

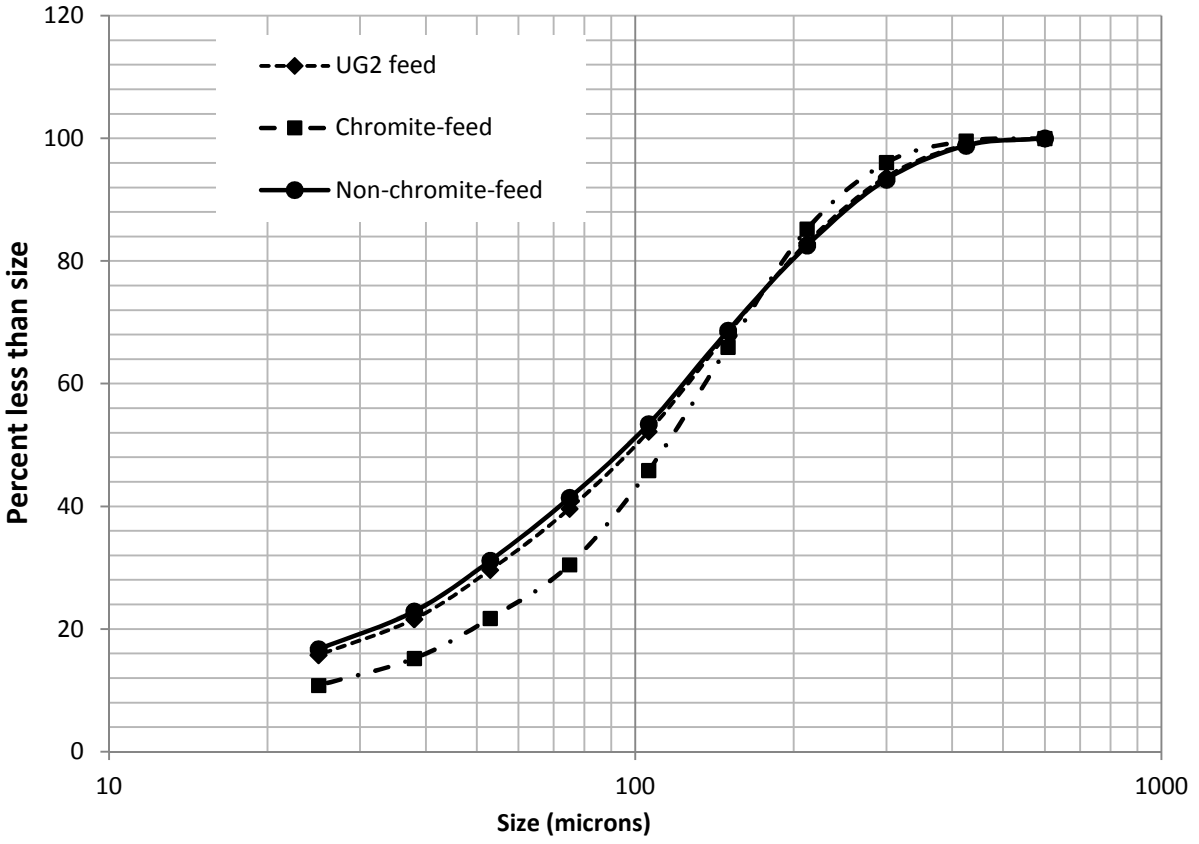


Figure 4.2 Particle Size Distribution of UG2 ore, chromite and non-chromite

4.4 Experimental method

Milling tests were carried out in accordance with the laboratory operating conditions specified in **Table 4.1**. The experiments were designed after completion of the DEM simulations that helped in selecting the actual ball milling tests variables.

Table 4.1 Laboratory operating conditions

<table>
<tr><td>Mill dimensions</td><td colspan="2">Diameter: 0.4 m
Length: 0.8 m (4 independent sections of 0.2 m)</td></tr>
<tr><td rowspan="2">Liner configuration</td><td colspan="2">Number 12
Height :15 mm Length: 400 mm</td></tr>
<tr><td>Trapezoidal (L1)
45° face angle
top width: 3 mm
bottom width: 33 mm</td><td>Trapezoidal (L2)
75° face angle
top width: 3 mm
bottom width: 20 mm</td></tr>
<tr><td>Test conditions</td><td colspan="2">Ball filling J: 30 %
Slurry filling U: 75 % of void volume
Slurry volume fraction f_c: 0.09
Mill speed: 60%, 65%, 70%, 75%...critical speed
Ball size: 20 mm and 30 mm</td></tr>
</table>

4.5 Sample collection

Samples were weighed wet while still in the collection bucket, then pressure filtered, using tared filter paper before being placed on a pan and in an oven for drying over night at a temperature of about 65°C. The dried samples were then re-weighed and the percent solids calculated. Care was taken to ensure that no portion of the dried samples were lost.

4.6 Density measurement

The standard procedure used to determine mono size chromite content grades, using ICP is often lengthy and expensive. A simple way to quickly get the chromite content grade is by measuring the mono size fraction densities. Individual sample densities were measured with the help of an analytical gas Pycnometer (AccuPyc version II 1340). This device provides a high precision measurement of density of powders, solids and slurries using a gas displacement

technique. Inert gases, such as helium or nitrogen, are used as the displacement medium. The sample was first weighed on a balance, and then sealed in the instrument compartment of known volume. Thereafter, the appropriate inert gas was admitted, and then expanded into another precision internal volume. The pressures before and after expansion were measured and used to compute the sample volume. Dividing this volume into the sample weight gives the gas displacement density.

4.7 Experimental programme

In order to achieve the objectives of this research work, the experimental programme was divided in three parts. The first part dealt with the particle size distribution analysis and chemical characterization of the feed and product samples. This part involved also tests aimed at determining the effect of mill speed and ball size on mill power draw and milling kinetics. The results are discussed in Chapter 5. The second part dealt with the measurement of density of size fraction samples of feed and products, in order to derive a relationship between the chromite grade and the density. The results are discussed in Chapter 6. The third part dealt with tests aimed at establishing separate milling kinetics of chromite and non-chromite minerals in the PGM ore. The results are discussed in Chapter 7. The S & B obtained in Chapter 7 are used in Chapter 8 to validate a matrix transformation model.

Chapter 5 Effect of operating variables on the ball milling

Batch milling tests were conducted in order to identify the effect of operating variables on the relative grinding rates of chromite and non-chromite particles. Following variables were regarded: ball size (mm), mill speed (% of critical speed) and lifter face angle (°). The variables that were regarded are ball size (mm), mill speed (% of critical speed) and liner profile. The entire ball milling test results on the ball milling variables can be found in **Appendix A.3**.

5.1 Effect of the lifter face angle on the mill power draw

The face angle of a lifter is a key criterion in optimising the motion of balls and their impact on the mill shell. The effect of three lifter face angles (45°, 75° and 90°) on power draw at different percent critical speed was studied in order to optimize the ball mill performance. The experimental tests were carried out without any slurry added to the ball mill. Only steel balls were loaded. The ball filling was set at 30 % of the mill volume. The results are shown in **Fig. 5.1.** It can be seen that the power draw increases gradually as the lifter face angle decreases from 90° to 45°; but quickly decreased beyond 70-80 % of the critical speed. The maximum power draw was also reached at different speeds. This is a clear indication that the actual higher speed depends also on the geometry of the lifter used. These results agreed fairly well with the DEM simulation predictions.

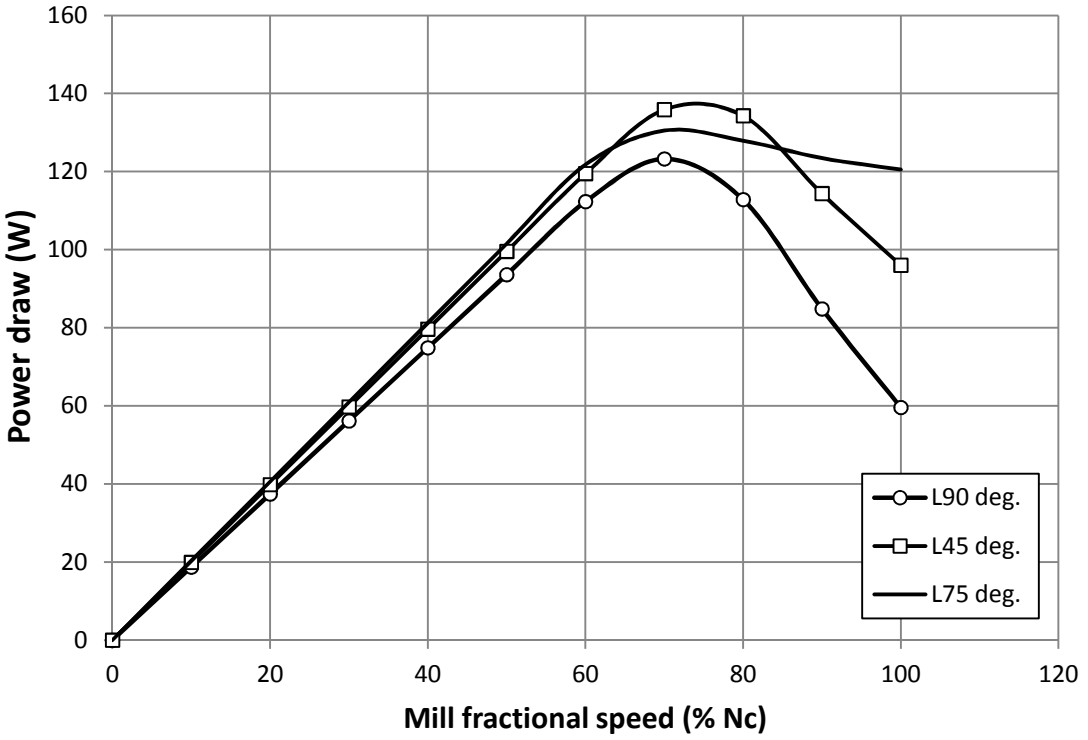


Figure 5.1 Experimentally measured power

5.2 Ball size and power draw sensitivity tests

The power draw sensitivity testing was done in order to determine the appropriate specific energy consumption to achieve the optimal size reduction of chromite and non-chromite components within the UG2 ore sample. The UG2 ore particles need to be reduced to 80 % - 75 µm. This is because PGM-bearing minerals are locked in the coarser (more than about 100 µm) silicate particles. As a result, they cannot be floated selectively. On the other hand, amount of chromite slimes (- 38 µm) should be minimized as much as possible. These tests were conducted with two ball sizes: 20 mm and 30 mm at three specific energy consumptions: 5 kWh/t, 10 kWh/t and 20 kWh/t. Milling with small balls (20 mm) results in fine grinding as compared to milling with large balls (30 mm), for the same amount of energy input, as shown in **Fig. 5.2** for non-chromite **and Fig. 5.3** for chromite. This can be explained in that small balls have larger total surface area, and consequently, larger grinding zones and higher milling rate.

However, use of small balls may be a challenge for breaking large particles. For a feed ore containing ore that is too big and strong to be properly nipped and fractured by small balls, larger balls should be used to increase the rate of breakage as it has been suggested by Austin *et al*. (1984). The particle size distributions were also compared in terms of the specific energy consumption. It appears that milling with 10 kWh/t reduced the non-chromite size to 80 % less than 75 microns without overproducing the chromite slimes.

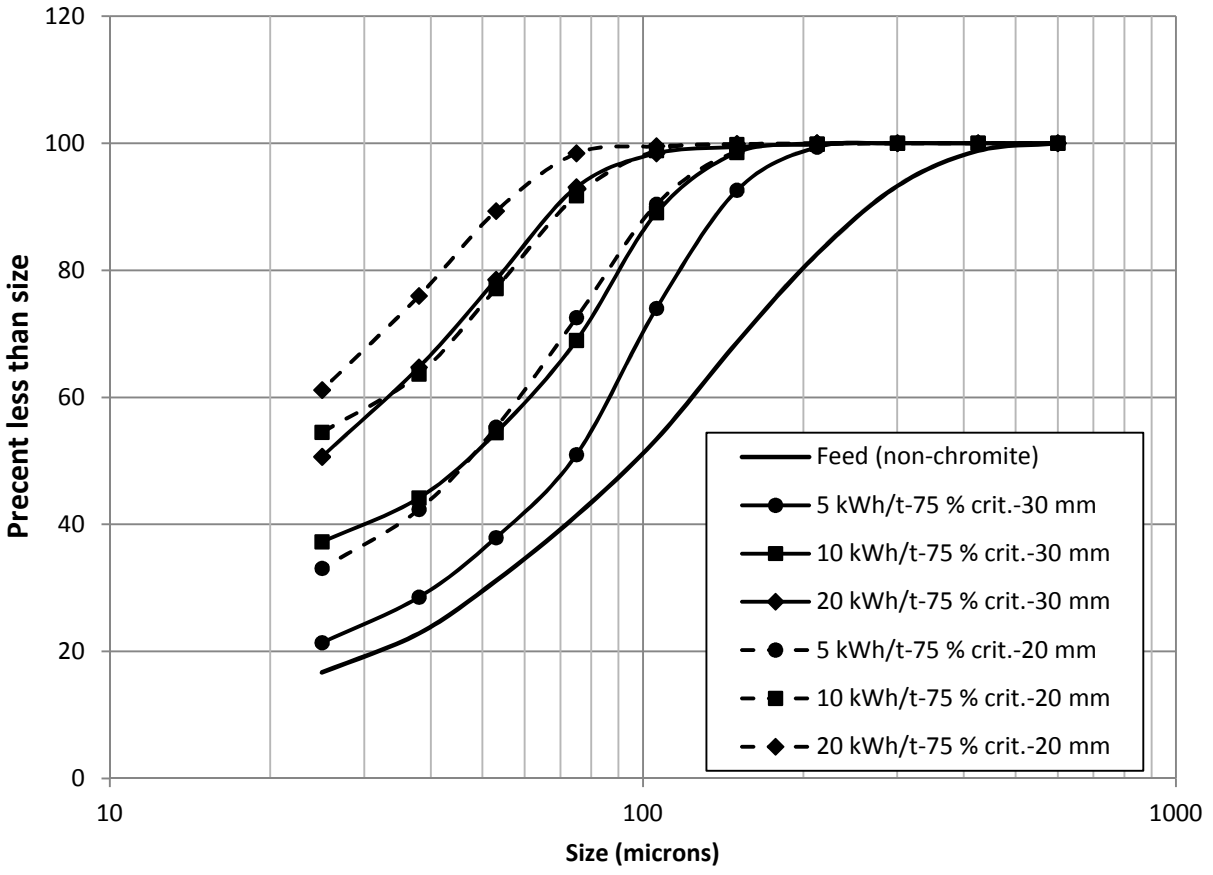


Figure 5.2 Effect of ball size and specific energy consumption on the non-chromite particle size distributions

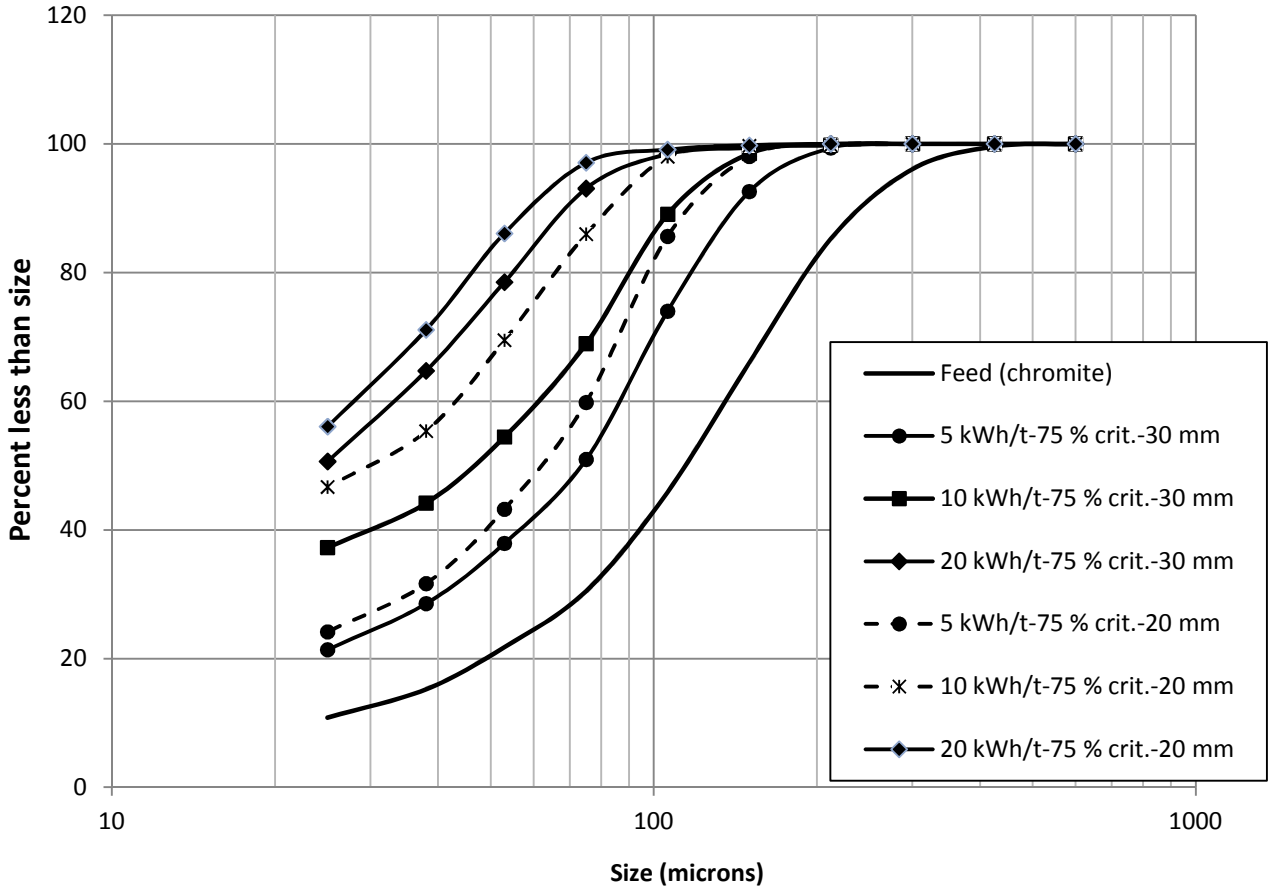


Figure 5.3 Effect of ball size and specific energy consumption on the chromite particle size distributions

5.3 Effect of percent critical speed

To investigate the effect of mill speed on the ball milling of chromite and non-chromite, we performed 6 experiments at three mill speeds (65 %, 670 % and 75 % of critical speed) at 10 kWh/t and two ball sizes (20 and 30 mm ball). The results are shown in **Fig. 5.4** for non-chromite and **Fig. 5.5** for chromite. It can be seen that the mill speed has only little effect on the milling products. It is accepted that with different conditions (load volume, percent solids, and slurry holdup) this conclusion may not hold.

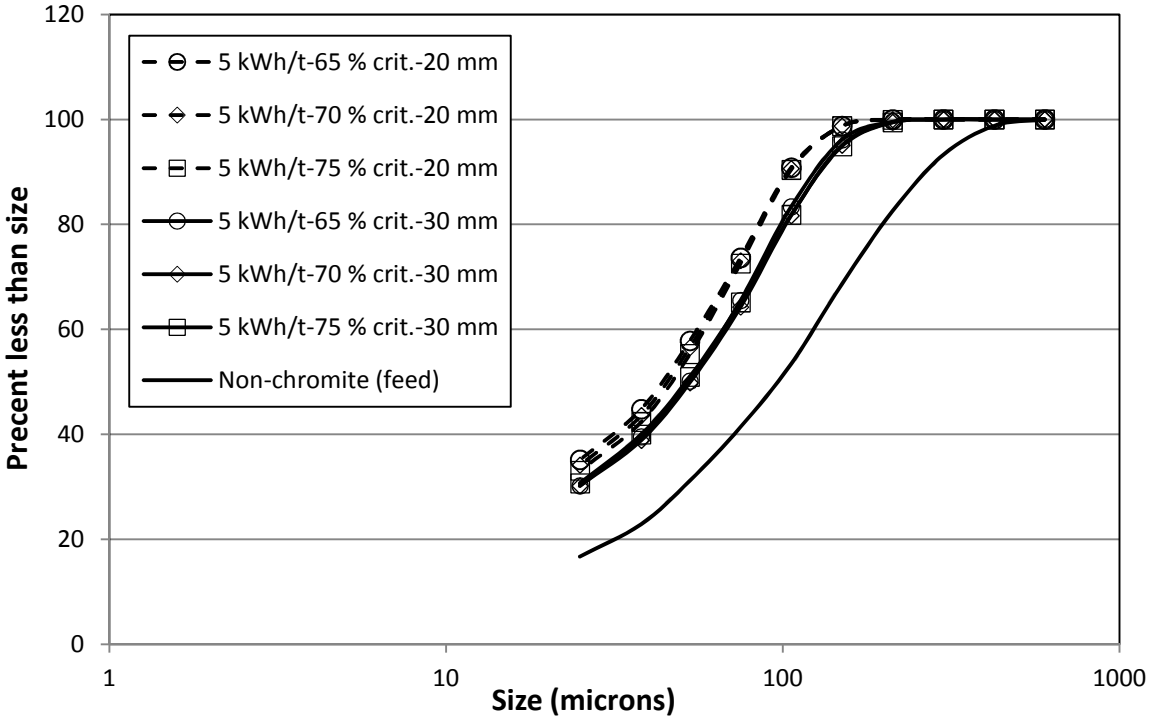


Figure 5.4 Effect of percent critical speed on the non-chromite particle size distributions (20 mm balls: dot lines and 30 mm balls: solid lines)

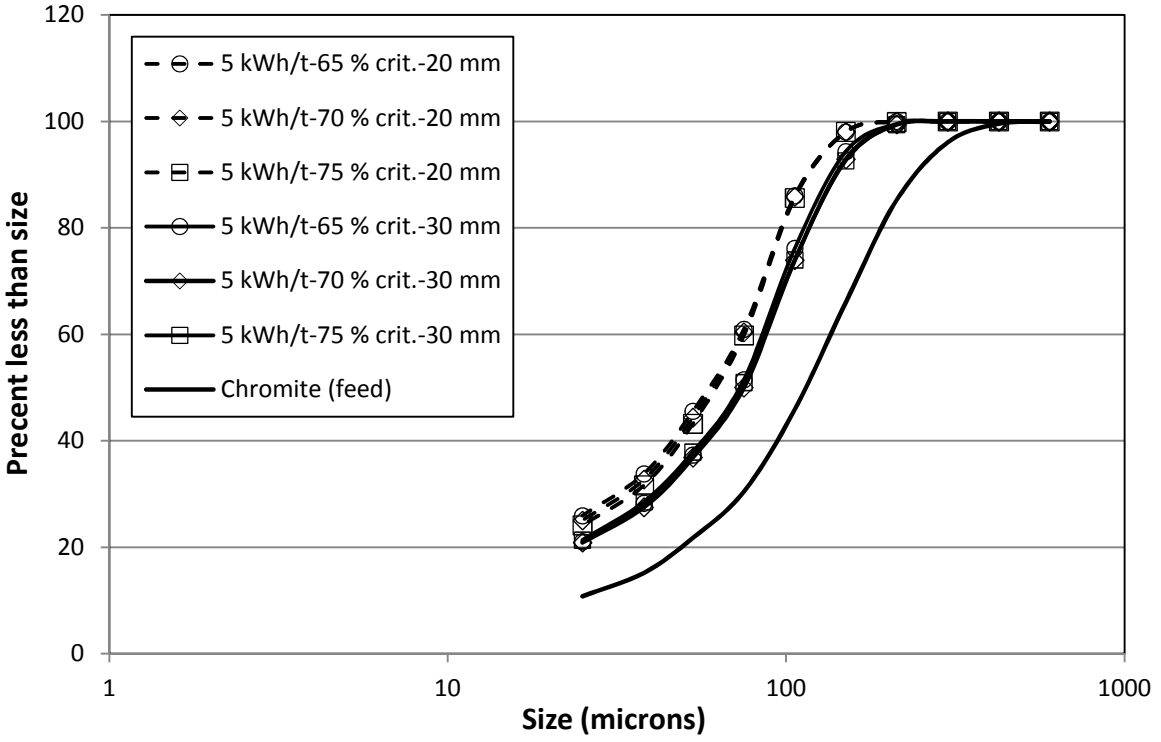


Figure 5.5 Effect of percent critical speed on the chromite particle size distributions (20 mm balls: dot lines and 30 mm balls: solid lines)

5.4 Conclusion

The following conclusions were drawn on the basis of the results obtained:

- For the grinding of the UG2 ore to 80 % passing 75 µm, the required specific energy was found to be 10 kWh/t
- The power draw was less sensitive to change in mill speed in the range considered in this work. Thus, 75 % of critical speed was chosen as the optimum mill speed
- The mill power draw increases gradually as the liner face angle decreases from 90° to 45°. The peak power draw was reached with use of 45° face angle liners
- Ball milling with 20 mm balls results in a finer grind compared to ball milling with 30 mm balls

In the next chapter, a simple model for estimating the chromite concentration by use of particle density measurements will be developed.

Chapter 6 Modelling of chromite grade as a function of density

Given that the main objective of the milling tests was to identify the effect of operating variables on the relative grinding rates of chromite and non-chromite particles, it was important to get a simple and cheap way of measuring their relative concentrations within the UG2 ore samples. A simple model relating the chromite concentration to the measured particle density in different size fractions of a UG2 ore sample was developed and it is presented in this Chapter.

6.1 Mineral distributions in the UG2 ore

The UG2 is typically composed of chromite rocks, pyroxenite rocks, pegmatoid rocks and anorthosite rocks. A distinctive feature of these rocks is their densities. Chromite rock type ($FeO.Cr_2O_3$) has a S.G. of about 4.2, which is significantly higher than that of pegmatoid and pyroxenite (both with S.G. of about 3.2), and anorthosite (about 2.8).

6.2 Chromite distribution in the UG2

The feed material was sized and submitted for the 4E (Pt, Pd, Rh and Au) and chromite analyses at Mintek. **Table 6.1** shows the assays of the original UG2 sample ore. It can be seen that the sample had high content of chromite (about 16 %).

Table 6.1 Chemical analysis of the UG2 ore sample

	mass	Au	Pt	Pd	Rh	Cr_2O_3	4E
Size Fractions	g	ppm	ppm	ppm	ppm	%	ppm
-600+425	1.2	<0.1	0.1	<0.1	<0.1	6.5	0.3
-425+300	5.4	<0.1	0.4	0.4	<0.1	10.4	0.9
-300+212	10.3	<0.1	0.2	0.1	<0.1	17.4	0.4
-212+150	15.3	<0.1	0.5	0.3	<0.1	21.0	0.8
-150+106	16.1	<0.1	0.8	0.3	<0.1	21.2	1.2
-106+75	11.7	<0.1	1.2	0.6	0.14	19.6	1.8
-75+53	9.3	<0.1	1.4	0.8	0.21	15.7	2.2
-53+38	9.6	<0.1	1.4	0.8	0.24	13.3	2.2
-38+25	5.3	<0.1	3.0	1.7	0.66	11.5	4.7
-25	15.8	<0.1	4.8	2.3	0.83	10.2	7.9
Total mass per 100g of sample	100.0	<1.0	13.6	7.4	1.33	16.3	22.4

Table 6.1 shows particle size distributions of chromite, non-chromite and 4E in the UG2 sample. It is clear that the chromite trend is very different from that of the non-chromite. The 4E that are associated with the fine interstitial silicate and sulphide minerals material between the chromite grains tend to concentrate in the finer fractions. The milling products were also sized and submitted for chromite analysis at the Mintek's Analytical Services Division. This was done in order to see how the chromite content was affected by the milling variables. The results are shown in **Table 6.2.**

Table 6.2 Chromite assays grade (in percent)

Size(microns)	Feed	30 mm ball diameter		20 mm ball diameter	
		5 kWh/t	10 kWh/t	5 kWh/t	10 kWh/t
-600 +425	6.46	-	-	-	-
-425 +300	10.40	-	-	-	-
-300 +212	17.40	14.65	17.08	17.33	16.35
-212 +150	21.00	18.70	18.34	18.45	18.45
-150 +106	21.20	21.32	20.91	20.10	20.73
-106 +75	19.60	20.39	20.72	19.90	20.40
-75 +53	15.70	16.88	18.00	17.40	19.00
-53 +38	13.30	15.72	17.08	15.90	18.33
-38 +25	11.50	14.02	14.88	14.20	16.19
-25	10.20	13.77	14.00	14.00	15.94

The relationship between the chromite grade and particle size was also interrogated. It can be seen that coarser fractions contain more chromite as compared to fine fractions, with higher concentrations of chromite situated around 106 µm. It was difficult to get the necessary mass of sample in the coarser fractions for chromite assays and density measurement. This explains why coarser fractions above 212 microns are not represented in **Table 6.2.** Conversely, the measured particle densities are presented in **Table 6.3.** The particle densities were measured by use of a gas pycnometer as described in Chapter 4.

Table 6.3 Measured densities (g per cm^3)

Size(microns)	Feed	30 mm ball diameter		20 mm ball diameter	
		5 kWh/t	10 kWh/t	5 kWh/t	10 kWh/t
-600 +425	3.30	-	-	-	-
-425 +300	3.39	-	-	-	-
-300 +212	3.60	3.49	3.54	3.54-	3.57-
-212 +150	3.68	3.59	3.62	3.66	3.66
-150 +106	3.68	3.67	3.64	3.67	3.67
-106 +75	3.55	3.6	3.63	3.63	3.63
-75 +53	3.43	3.5	3.55	3.56	3.56
-53 +38	3.35	3.46	3.48	3.51	3.51
-38 +25	3.27	3.35	3.39	3.41	3.41
-25	3.21	3.49	3.31	3.31	3.31

In Fig. 6.1, the measured density is plotted against the particle size. This suggests a linear relationship between density and particle size. It can also be seen that the chromite grade goes higher in coarse particle sizes.

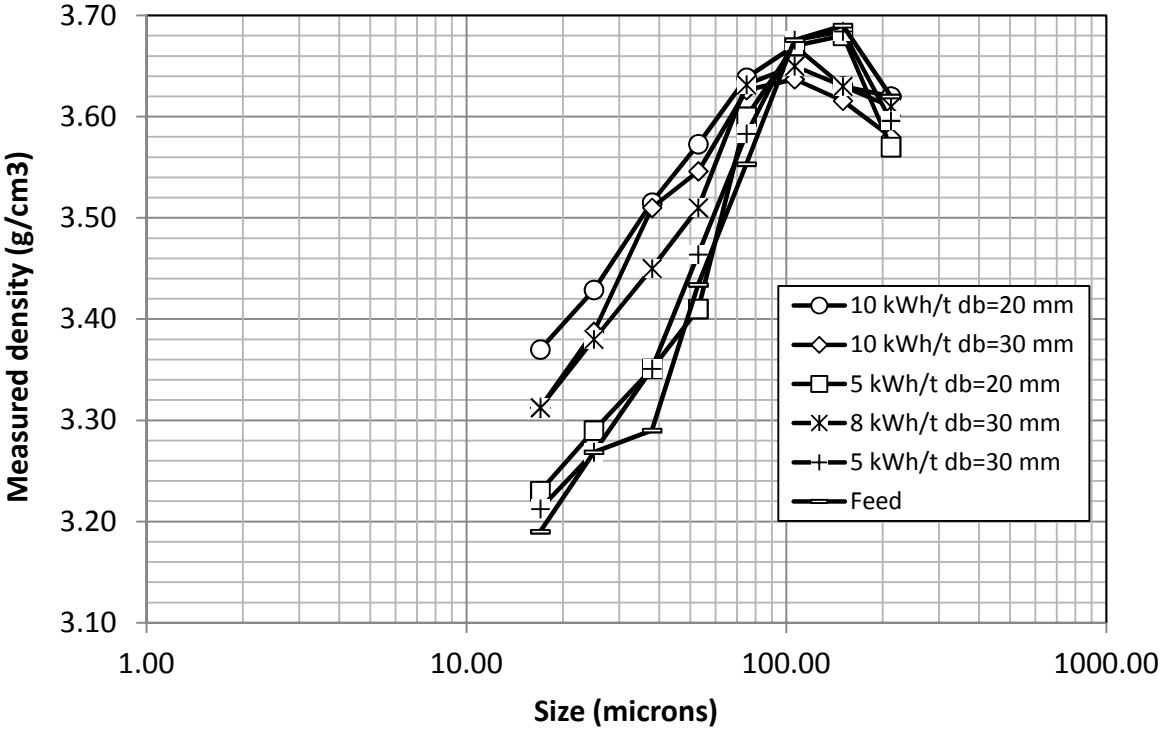


Figure 6.1 Measured density as a function of grain size

6.3 Modelling the chromite grade as a function of particle density

Mathematically, density is defined as mass divided by volume.

$$\rho = \frac{m_{tot}}{v} \qquad (6.1)$$

If we assume the UG2 ore to be constituted of two distinct components: the chromite and the non-chromite components. **Eq. (6.1)** becomes

$$\rho = \frac{m_{tot}}{\frac{m_1}{rho_1} + \frac{m_2}{rho_2}} \qquad (6.2)$$

where chromite is indicated by subscript 1 and non-chromite is indicated by subscript 2

If a and b express the fractions of chromite and non-chromite particles in the UG2 ore sample, given by

$$a = \frac{m_1}{m_{tot}} \quad and \quad b = \frac{m_2}{m_{tot}} \qquad (6.3)$$

$$with \quad a + b = 1$$

Equation (6.2) becomes then

$$\rho = \frac{1}{\frac{a}{rho1} + \frac{1-a}{rho2}} \qquad (6.4)$$

We derive a as follows

$$a = \frac{\left(\frac{1}{\rho} - \frac{1}{rho_2}\right)}{\left(\frac{1}{rho_1} - \frac{1}{rho_2}\right)} \qquad (6.5)$$

The grade of Chromite particles within the UG2 ore is then given by

$$C = 100 \times \beta \times \frac{\left(\frac{1}{\rho} - \frac{1}{rho_2}\right)}{\left(\frac{1}{rho_1} - \frac{1}{rho_2}\right)} \qquad (6.6)$$

where β is a correction factor that depends on the ore texture, densities of minerals, packing arrangement and some unknown parameters. If these factors are disregarded, then beta is equal to 1.

Eq. (6.6) becomes then

$$C = 100 \times \frac{\left(\frac{1}{\rho} - \frac{1}{rho_2}\right)}{\left(\frac{1}{rho_1} - \frac{1}{rho_2}\right)} \qquad (6.7)$$

The variable ρ was determined from direct measurement of sample particle's densities, using a gas pycnometer. The remaining variables (rho1 and rho2) were estimated using the Excel Subroutine Solver that minimizes the residual error between the measured and predicted chromite grades. The values found for rho1 and rho2 were 4.32 and 3.24 respectively. If these values are inserted into **Eq. (6.7)** the model becomes:

$$a = 100 \times \frac{\left(\frac{1}{\rho} - \frac{1}{3.24}\right)}{\left(\frac{1}{4.32} - \frac{1}{3.24}\right)} \qquad (6.8)$$

The measured chromite concentrations were plotted against the estimated ones in **Fig. 6.2**. It can be seen that there is close agreement between the measured and the model predicted chromite concentrations. The few discrepancies were believed to be mainly due to sampling and handling errors. Therefore, this model can be reliably used to predict the chromite concentrations along the size fractions for the actual UG2 sample.

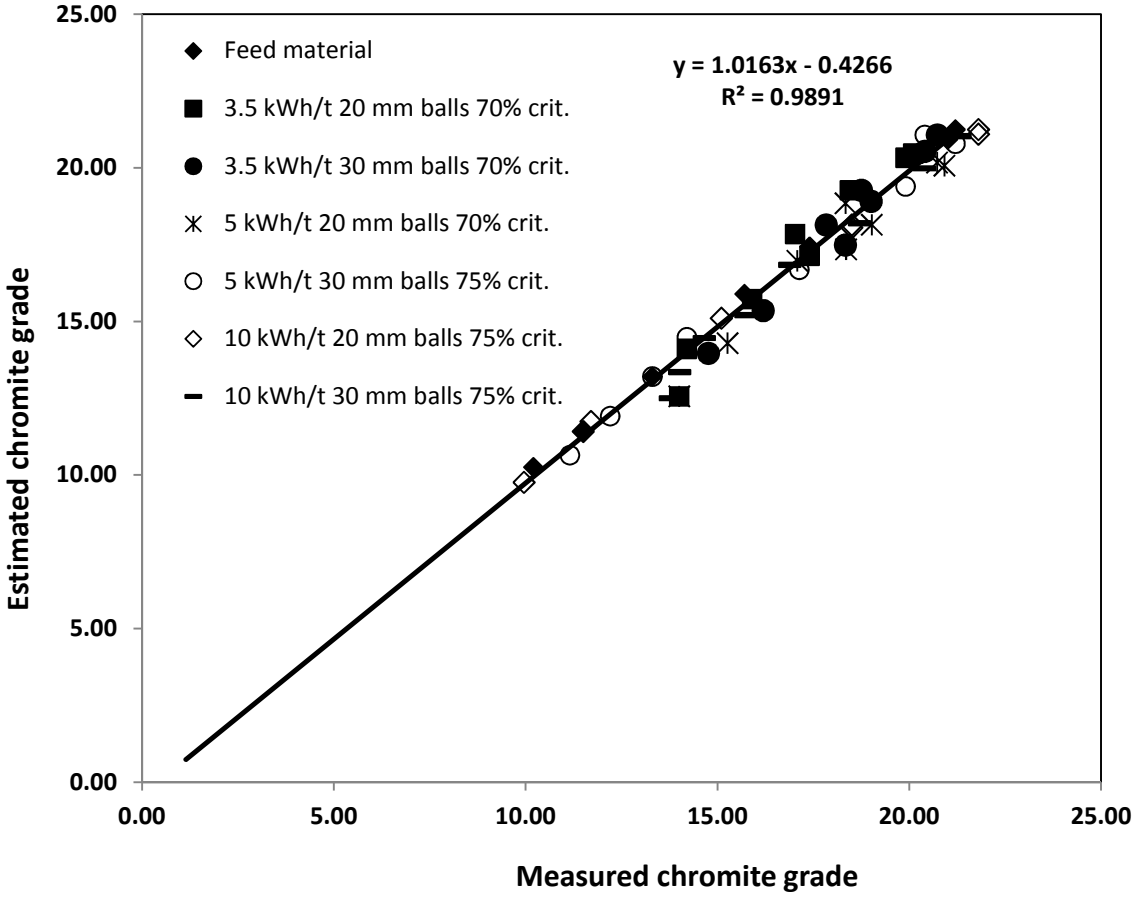


Figure 6.2 Measured chromite grade (abscissa) versus estimated chromite grade (ordinate)

Chapter 7 Milling Kinetics

In this Chapter, we separately present an analysis of the ball milling kinetics of UG2 ore as a binary mixture of chromite and non-chromite components. This was done in order to quantify the milling kinetics of each individual component and, subsequently to develop a binary grinding process model. The binary model is presented in Chapter 8. The milling tests were conducted on a sample previously ground with a Koppern High Pressure Grinding Roll (HPGR) to -600 µm. The feed material and some milling products were submitted for size-by-assay analyses in order to determine the chromite content in each size fraction. The non-chromite content in each size fraction was subsequently calculated. For the remaining milling products, the particle densities were determined by using model **Eq. (6.8)**.

The one-size fraction method by Austin *et al.* (1984) for measuring the Selection and Breakage Functions was used to determine the breakage and selection function parameters. To this end, four different monosize fractions were prepared and wet ground batch wise using a laboratory-scale ball mill at Mintek: - 600 +425µm, - 425 + 300 µm, - 300 + 212 µm and, - 212 + 150 µm. After the sample and the balls were loaded to the ball mill, it was run for 2 different time intervals (0.5 and 20 minutes). The short time provided data more strongly related to the Breakage Function for the ore since not much secondary breakage is expected. Ideally there should have been several tests at longer times, but shortage of time made this impossible.

The total individual composite samples for each test were carefully removed from the mill. They were weighed wet while still in the collection bucket, then pressure filtered, using tared filter paper before being placed on a pan and finally in an oven for drying over night at a temperature of about 65°C. The dried samples were then re-weighed and a representative sample was taken for

particle size distribution determination. Then, the feed for the next grinding period was the material retained on the screens, combined with the rest of the mill contents. Details on the milling kinetics data can be found in **Appendix A.4**.

7.1 Simulation of the grinding process

The Matlab simulator code by Bwalya (2012) that directly translates the population balance model, **(Eq. (2.15))** was used to generate the simulated product size distribution. The flowchart of the calculation procedure is shown in **Fig. 7.1**. In order to tune this simulator with the actual grinding process, the breakage function parameters (**β, γ and Φ**) and selection function parameters **(α)**, determined from the experimental tests according to the one-size method by Austin *et al.*(1984), were pre-entered into the code. The selection Function parameter **a** was then estimated by the simulator by minimising the sum of squared errors (SSEs) between the predicted and experimental product size distributions. Finally, the $\mathbf{b_{i,j}}$ functions were then back-calculated by the simulator.

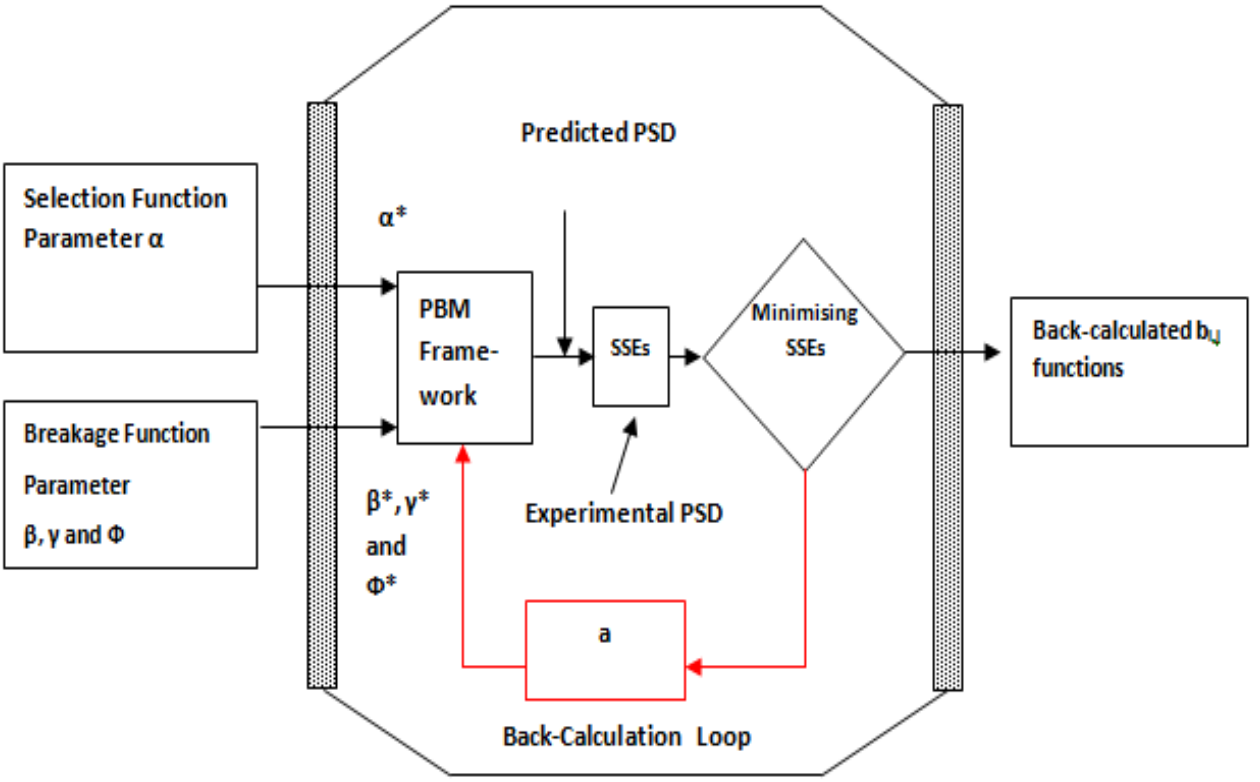


Figure 7.1 Schematic representation of the simulator used

7.2 Results and discussions

This section presents the results and discussions on the milling kinetics modelling of chromite and non-chomite components within the UG2 ore. The batch tests were performed on the UG2 ore sample with two different media sizes, 20 and 30 mm balls, according to Austin *et al*. (1984). The overall objective was to establish the grinding rates of chromite and non-chromite within the UG2 ore sample, and compare them. This was done through the determining of the Selection and Breakage (S and B) Functions.

7.2.1 Determination of the Selection Function parameters

7.2.1.1 UG2 ore Selection Function

The size-dependence of the Selection Function parameters **Eq. (2.3)** was used to derive numerically the rate of breakage of the UG2 ore. The experimental mass percents retained on the top screen were plotted against the grinding time t on a log-linear scale for all feed sizes and both media sizes: 20 mm and 30 mm. **Fig. 7.2** shows the grinding results of UG2 ore plotted in first order varying four different mono sized fractions, and ground batch-wise for 0.5 and 20 minutes. The breakage process was assumed to follow a first order kinetic model for all feed sizes.

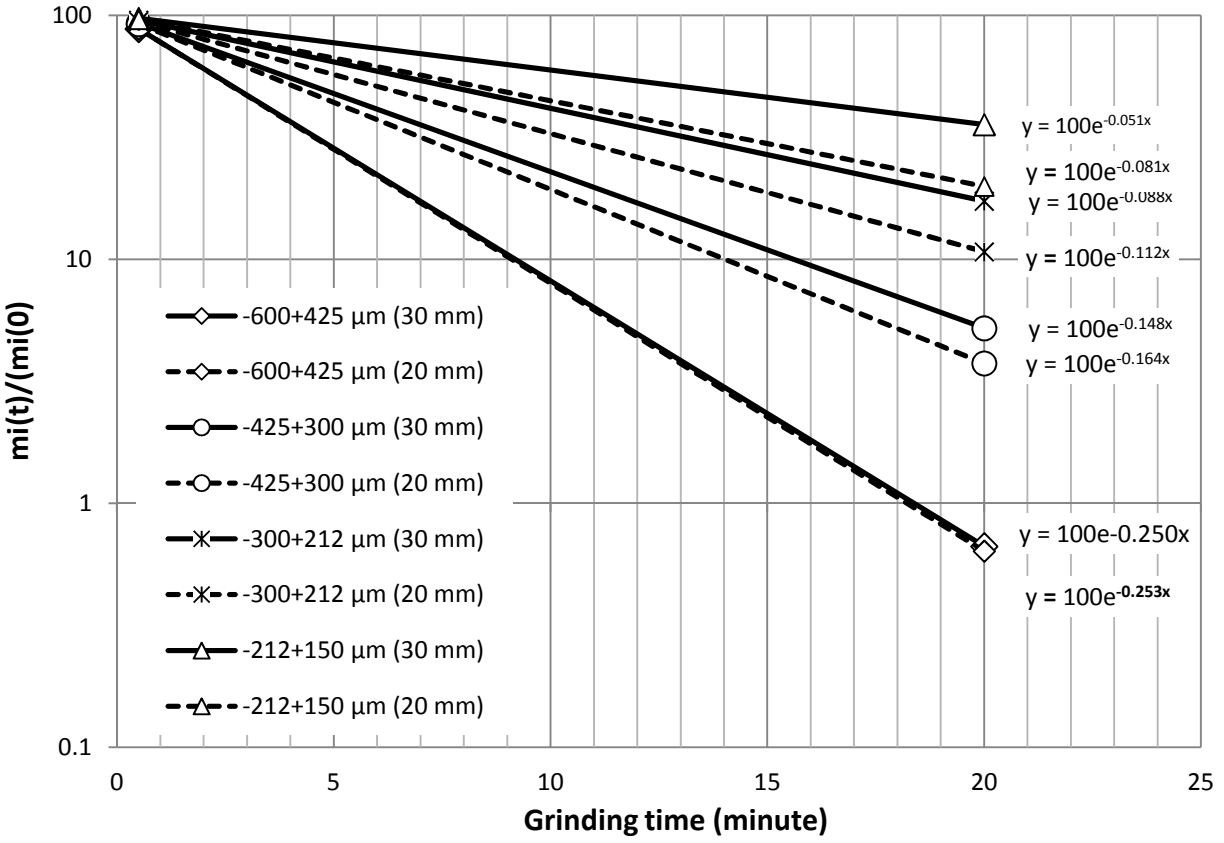


Figure 7.2 First-order plots for various feed sizes of UG2 ore ground in a laboratory-scale ball mill

7.2.1.2 Chromite Component Selection Function

Fig. 7.3 shows the grinding results of the Chromite component obtained from plotting the mass percentage retained on the top screen against grinding time t on a log-linear scale for all the feed sizes and two media sizes, 20 mm and 30 mm.

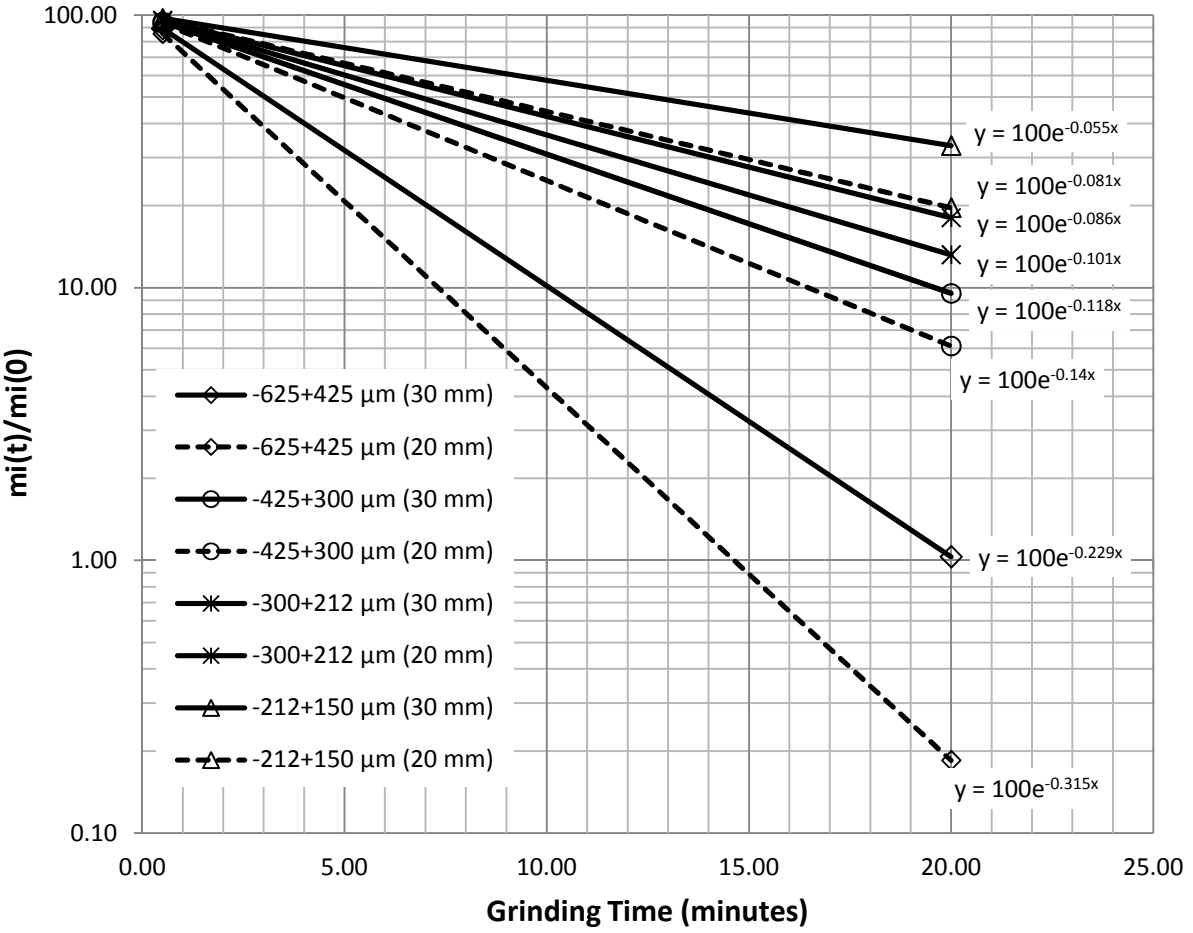


Figure 7.3 First-order plots for various feed sizes of Chromite Component ground in a laboratory-scale ball mill

7.2.1.3 Non-chromite Component Selection Function

Fig. 7.4 shows the grinding results of the non-chromite component obtained from plotting the mass percentage retained on the top screen against grinding time t on a log-linear scale for all the feed sizes and two media sizes, 20 mm and 30 mm.

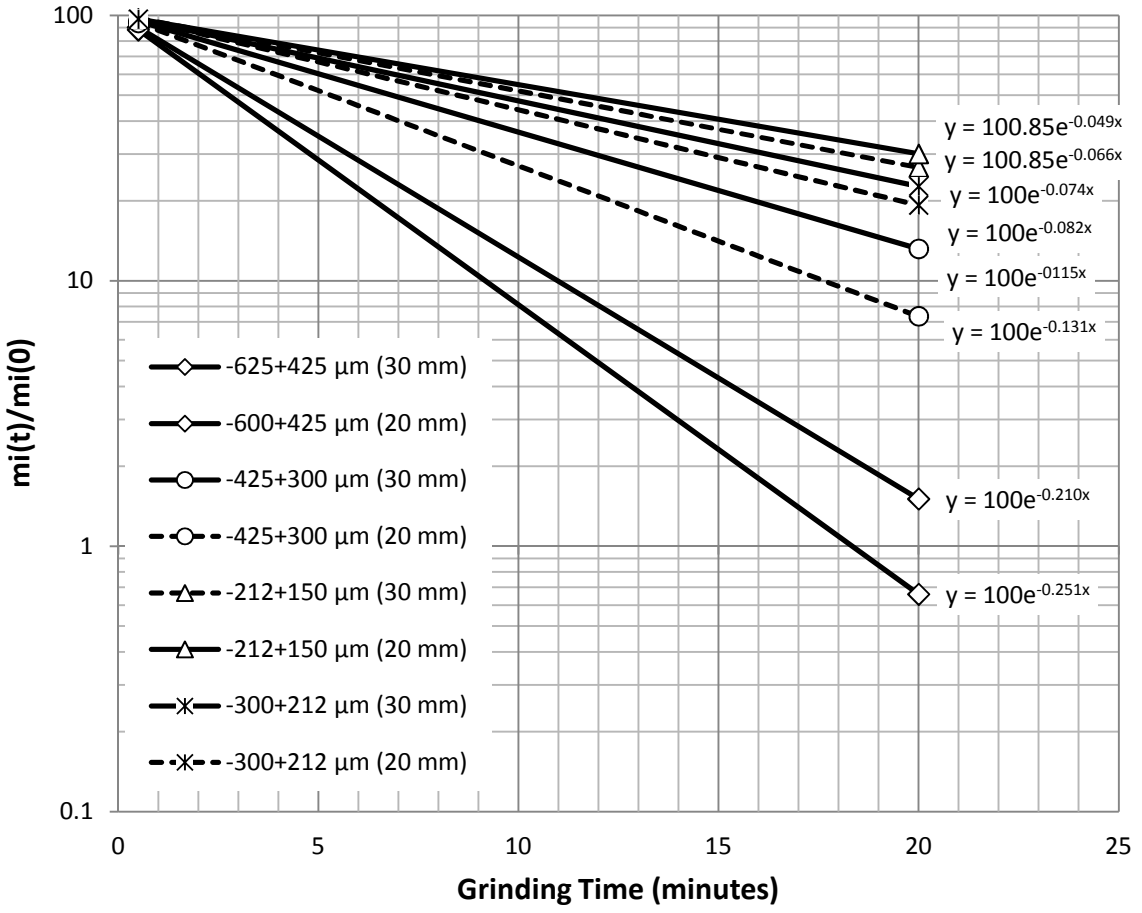


Figure 7.4 First-order plots for various feed sizes of Non-Chromite Component ground in a laboratory-scale ball mill

The graphical procedure of the full determination of all parameters associated with the selection function is given in **Fig. 2.2** (Austin *et al.,* 1984). Clearly, our data is in the low-particle-size linear region, i.e. $S = ax^{alpha}$. Both the 20 mm

and 30 mm curves are assumed to be linear over the full range that is, before the xm (the size at which the maximum value of S occurs). With respect to our data, the values of lamda (Λ) and gamma (γ) could not be determined. This is because all the feed sizes were not coarser. In other words, the breakage took place in the normal region where the media are large enough to break the particles efficiently. In this way, the appropriate S values for abnormal breakage region were not described, as the maximum values for S were not reached. In turn, the values of a and alpha (α) were determined using a power function from **Fig. 7.5** (ball diameter = 20 mm) and **Fig. 7.6** (ball diameter = 30 mm).

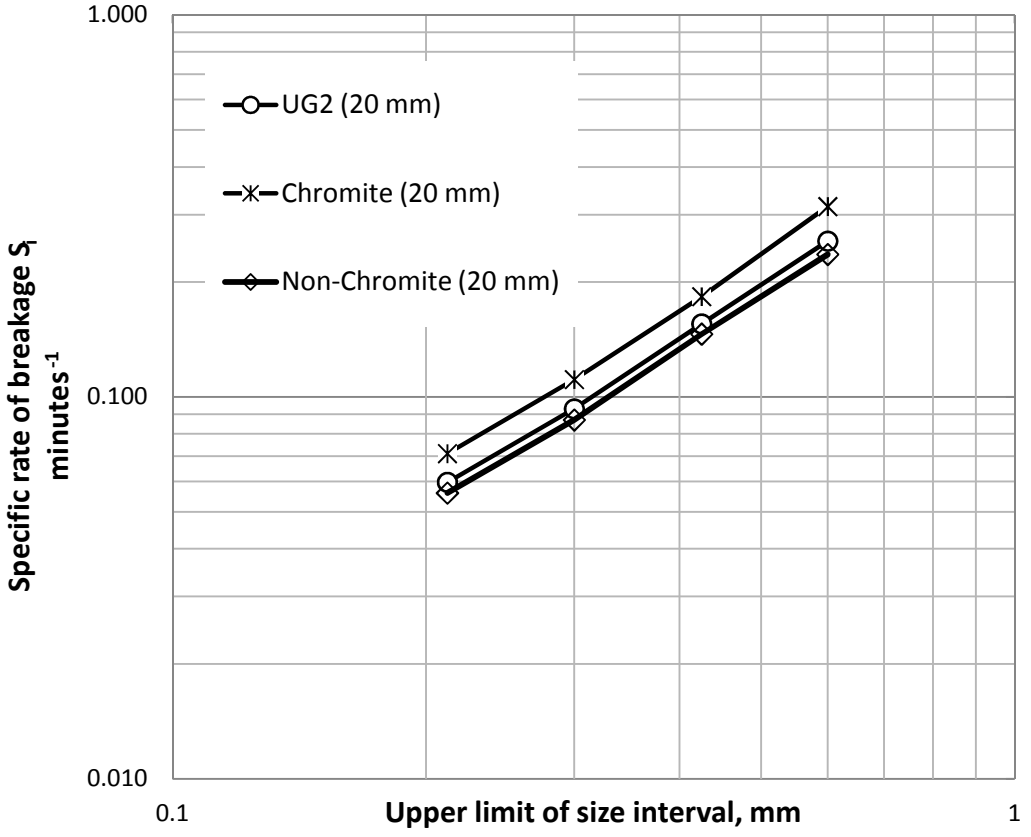


Figure 7.5 Specific rates of breakage of UG2 ore, Chromite Component and Non-Chromite Component as a function of particle size (Ball diameter = 20 mm)

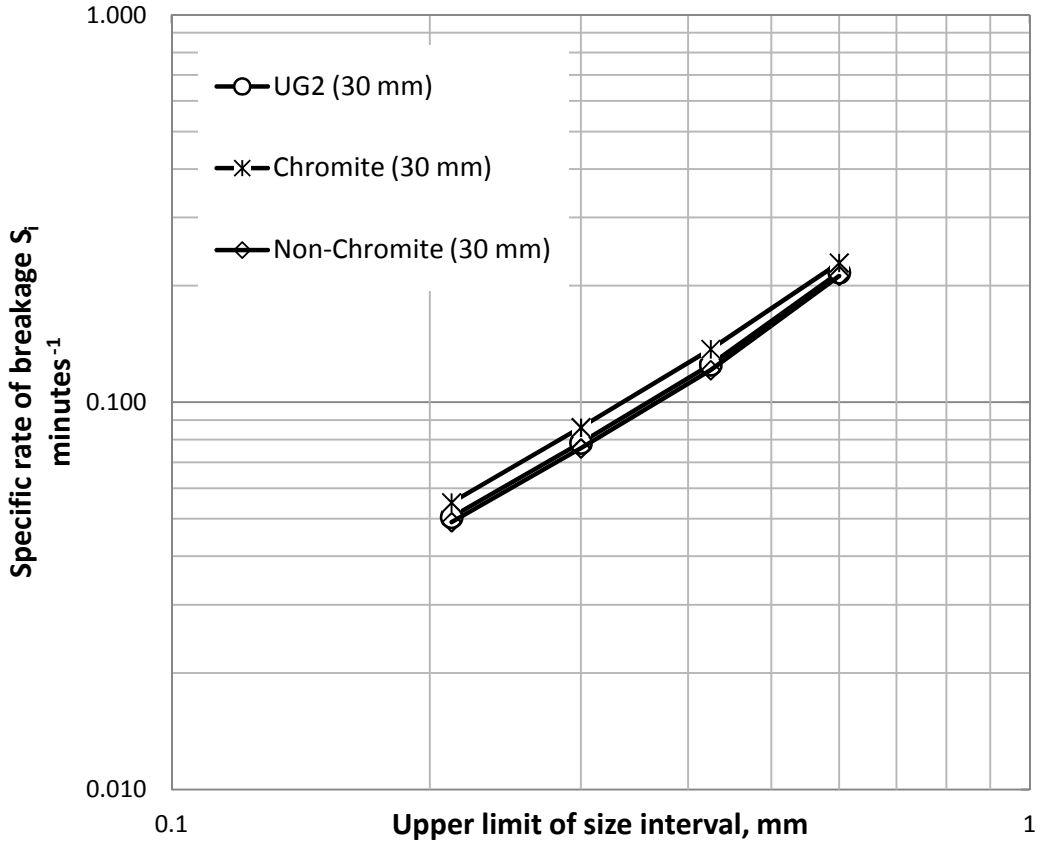


Figure 7.6 Specific rates of breakage of UG2 ore, Chromite Component and Non-Chromite Component as a function of particle size (Ball diameter = 30 mm)

The Selection Function parameters are summarized in **Table 7.1**.

Table 7.1 Selection Function descriptive parameters

Parameters	**UG2 ore**		**Chromite Component**		**Non-Chromite Component**	
Ball diameter	20 mm	30 mm	20 mm	30 mm	20 mm	30 mm
α	1.405	1.392	1.432	1.368	1.393	1.401
a	0.518	0.427	0.639	0.452	0.478	0.419

Figs. 7.5 and 7.6 show also that the magnitudes of the Selection Function for all feed sizes are inversely proportional to the ball size. Austin et al. (1984) stated

that if balls with the smaller diameter are used for the same ball filling (J=30%), to grind relatively small particles, the rate of ball on ball contacts per unit time increases. This is owing to the fact that smaller balls have higher total surface area, which results in the rate of breakage of smaller sizes being higher for smaller ball diameters. These results fully agree with our DEM simulation results in **Section 3.3**. Small balls exhibited larger dynamic angle of repose, higher shoulder position, higher power draw and therefore will grind faster than larger balls. Faster breakage (i.e. higher value of Si) was obtained for the chromite component, whereas slower breakage was obtained for the non-chromite component. The breakage rate of the UG2 obtained ore was between the breakage rates of chromite component and non-chromite component.

7.2.2 Determination of the breakage function parameters

7.2.2.1 UG2 ore Breakage Function

The B-II calculation procedure of the primary breakage function as proposed by Austin et al. (1984) was used to generate the breakage function parameters. This method suggests use of shorter grinding times, which result in 20–30% broken materials out of the top size before re-breakage. Austin and Luckie (1971) further stated that up to 65% broken material will still provide accurate enough good data to be used with this procedure. The values of cumulative breakage distribution function were fitted by **Eq. (2.13)**. All the feed materials were considered to be normalizable ($\delta = 0$) for simulation purposes. This means that the fraction appearing at sizes less than the initial feed size is independent of the initial feed size. The cumulative breakage distribution functions of UG2 ore, chromite component and non-chromite component at different initial feed sizes are shown in **Figs 7.6, 7.7 and 7.8**.

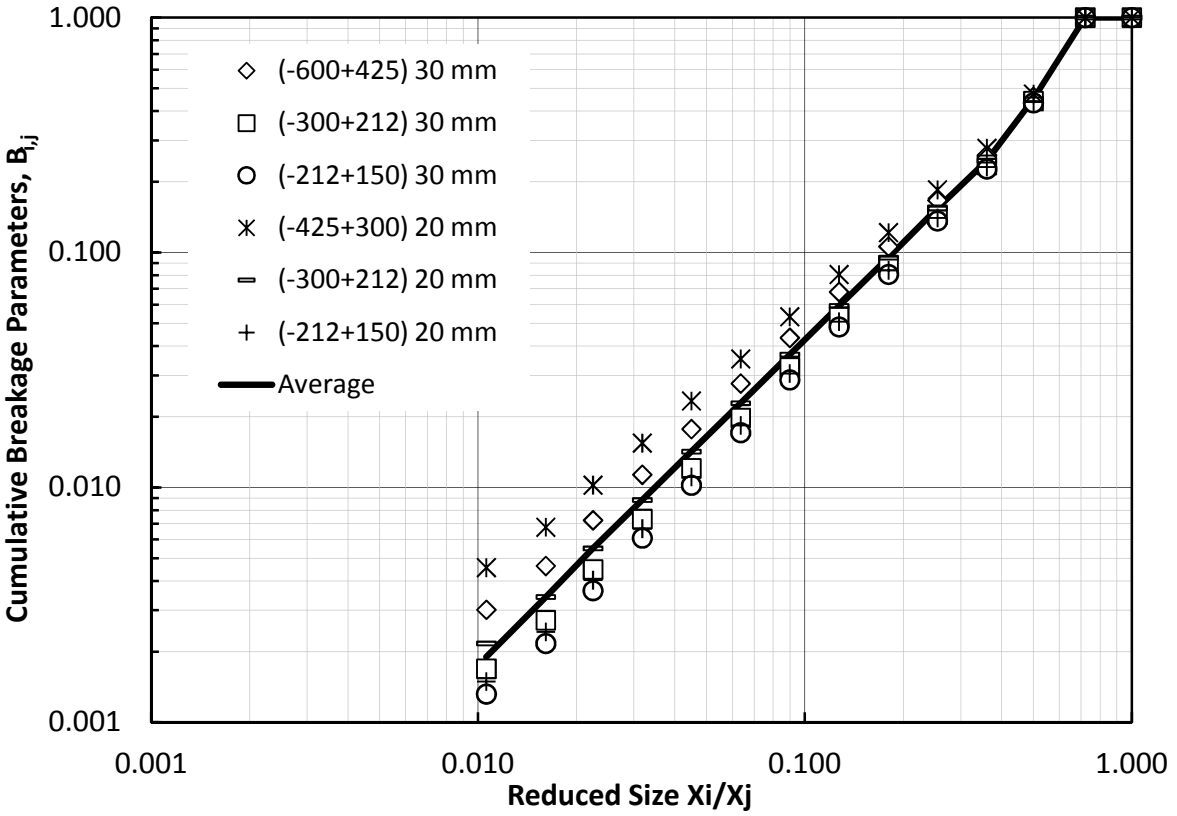


Figure 7.6 Breakage Function Distributions for various sizes of UG2 ore

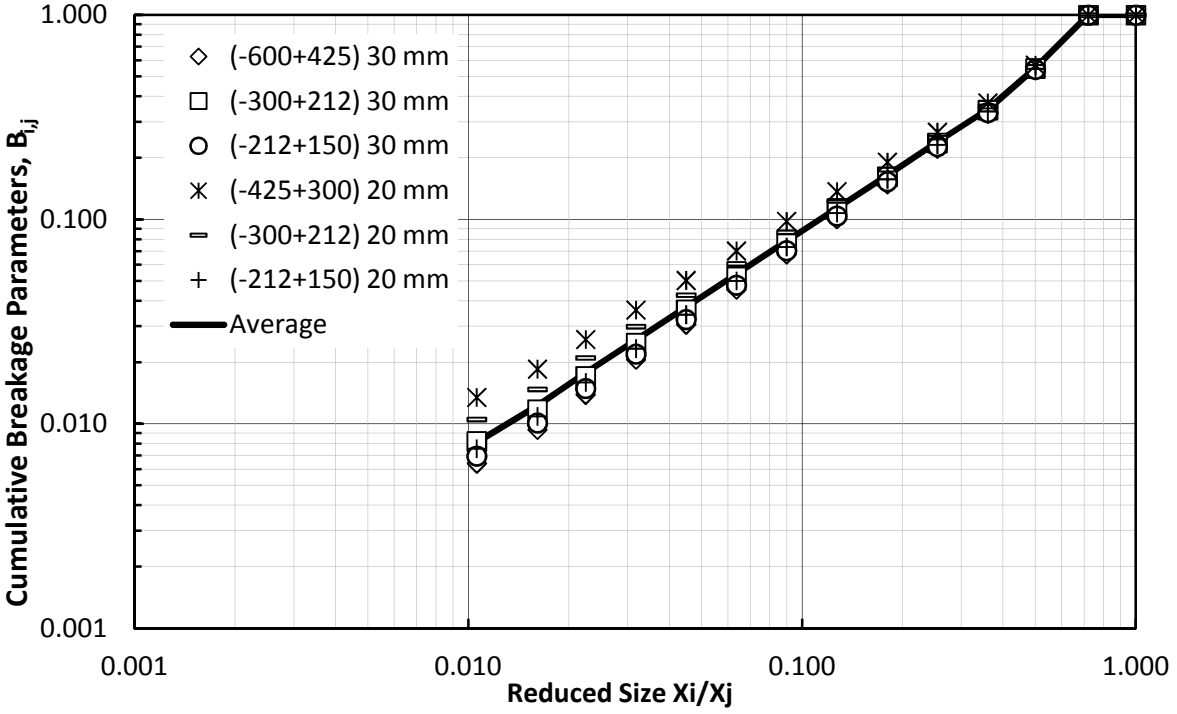


Figure 7.7 Breakage Function Distributions for various sizes of chromite component

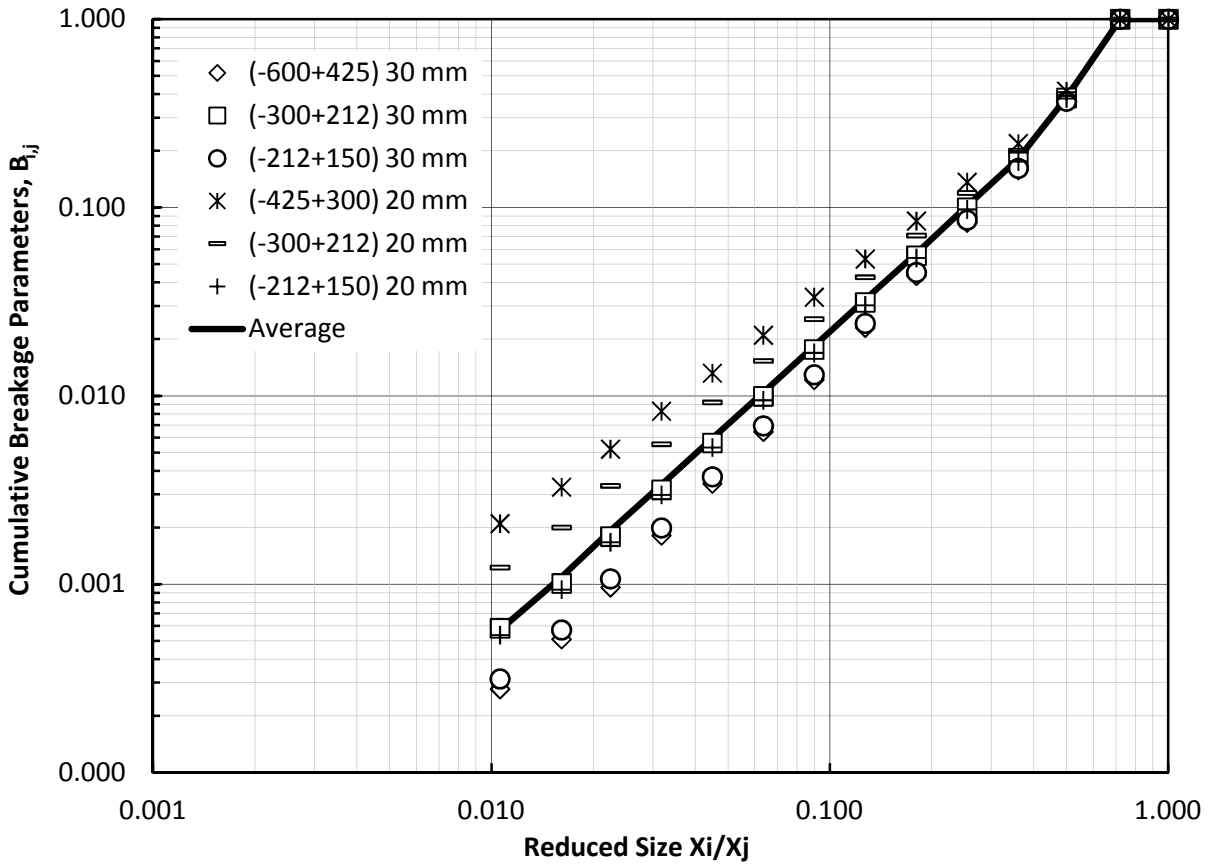


Figure 7.8 Breakage Function Distributions for various sizes of non-chromite component

The B_{ij} values obtained were fitted to the empirical model in **Eq. (2.13)** (Austin *et al*., 1984), and the model parameters: β, γ and ϕ for the UG2 ore were then evaluated. The Breakage Function parameters are listed in **Tables 7.2 and 7.3**.

Table 7.2 The primary breakage distribution parameters obtained for short grinding times (ball diameter = 20 mm)

Particle Size (μm)	UG2 Ore			chromite component			non-chromite component		
	β	γ	Φ	β	γ	Φ	β	γ	Φ
-600+425	6.20	1.19	0.62	7.90	1.04	0.75	5.35	1.12	0.56
-425+300	6.20	1.29	0.62	7.90	1.11	0.75	5.35	1.20	0.56
-300+212	6.20	1.40	0.62	7.90	1.18	0.75	5.35	1.27	0.56
-212+150	6.20	1.47	0.62	7.90	1.23	0.75	5.35	1.30	0.56

Table 7.3 The primary breakage distribution parameters obtained for short grinding times (ball diameter = 30 mm)

Particle Size (μm)	UG2 Ore			chromite component			non-chromite component		
	β	γ	Φ	β	γ	Φ	β	γ	Φ
-600+425	6.00	1.24	0.60	7.40	0.96	0.71	5.30	1.19	0.55
-425+300	6.00	1.27	0.60	7.40	1.02	0.71	5.30	1.17	0.55
-300+212	6.00	1.30	0.60	7.40	1.09	0.71	5.30	1.12	0.55
-212+150	6.00	1.37	0.60	7.40	1.13	0.71	5.30	1.15	0.55

In order to compare the Breakage of the UG2 ore, chromite component and non-chromite component, their respective average Cumulative Breakage Function Distribution were plotted together in **Fig. 7.9**. It can be seen that the chromite component is reduced more rapidly to lower sizes as compared to the non-chromite component. The UG2 ore Breakage Distribution shows an average behaviour of these two components.

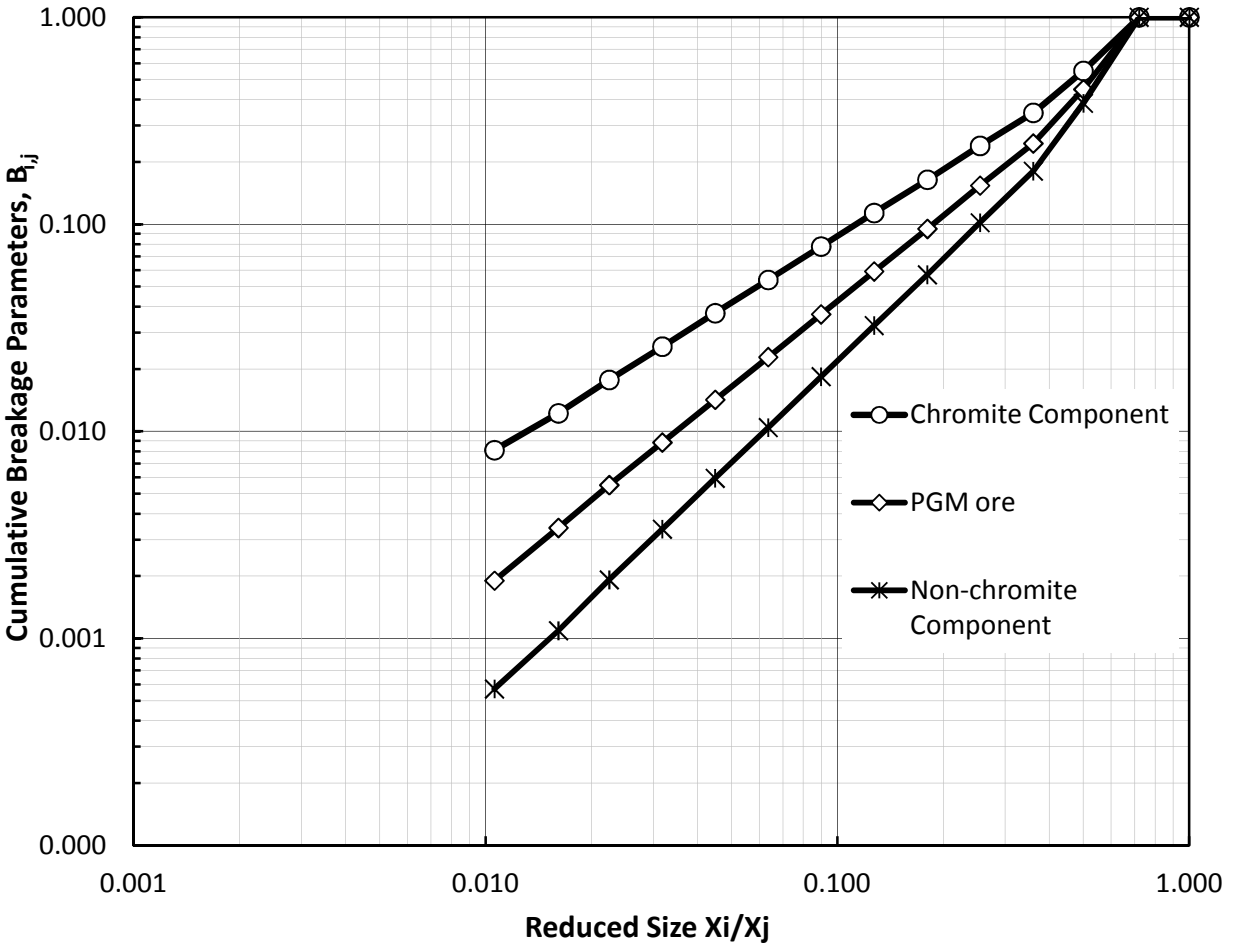


Figure 7.9 Comparison of the Cumulative breakage distribution functions (UG2 ore, Chromite Component and Non-Chromite Component)

The average breakage function parameters are listed in the Table below.

Table 7.4 Breakage Function descriptive parameters

Breakage Function parameters	UG2 ore		chromite component		non-chromite component	
Ball diameter	20 mm	30 mm	20 mm	30 mm	20 mm	30 mm
β	**6.20**	**6.00**	**7.90**	**7.40**	**5.35**	**5.30**
γ	**1.34**	**1.30**	**1.14**	**1.05**	**1.22**	**1.16**
Φ	**0.62**	**0.60**	**0.75**	**0.71**	**0.56**	**0.55**

The Breakage distribution parameters are listed in **Table 7.3**. The value of γ was smaller for the Chromite component, indicating that the higher relative amounts of progeny chromite fines were produced from the breakage, compared to the non-chromite. This is also indicated by the values of Φ. Large values of Φ were obtained for the chromite component, indicating that larger fraction of chromite fines were produced in a single fracture event.

7.2.3 Particle size distributions

The parameters (α, a and γ) were estimated by the optimization model that seeks the best combination of these parameters in order to minimize the residual error between the experimental and predicted product size distributions. The parameters of the Selection and Breakage Functions evaluated from the experimental data were used as initial guesses to the model in the parameter search process.

7.2.3.1 UG2 ore particle size distributions

The measured and predicted size distributions for all the milling products are given in **Figs. 7.10 a-f**. It can be seen that there is a reasonable agreement between the measured size distributions, shown as markers in the plotted graphs, and the simulated size distributions, shown as solids lines. This suggests that the Selection and Breakage Functions parameters obtained can be used for continuous operation mass balance. In most cases, the predictions gave a relatively coarser product for the shorter grinding time of 0.5 min. Similar results were also presented by Chimwani *et al*. (2012) based on the experiments they did on a UG2 ore. One can also notice that ball milling with 20 mm balls gave finer products as compared to ball milling with 30 mm balls. This is explained in that smaller balls have higher total surface areas, as compared to larger balls.

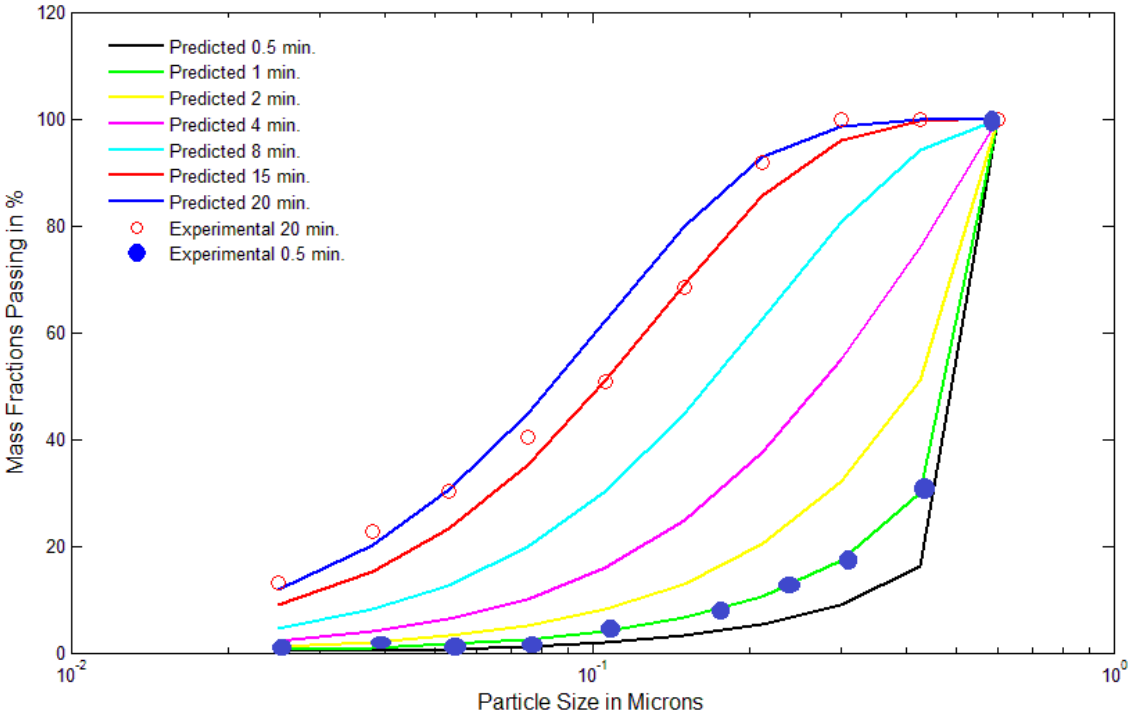


Figure 7.10a Measured and predicted particle size distributions corresponding to 20 mm balls and feed size: -212 + 150 µm

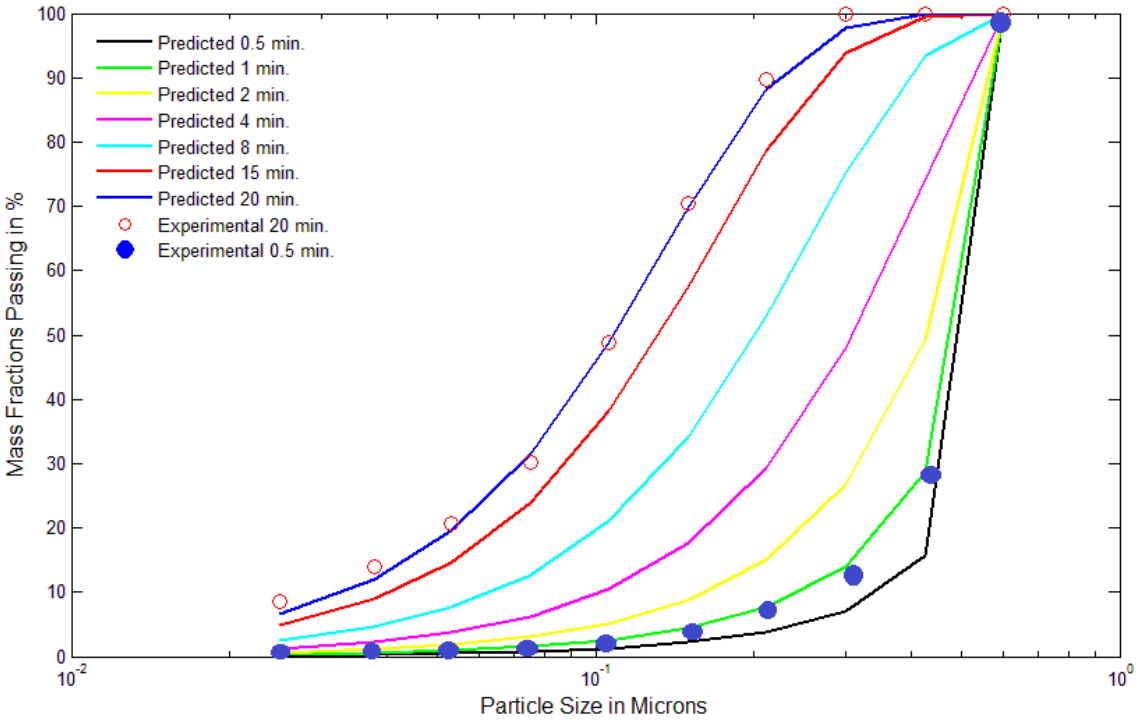


Figure 7.10b Measured and predicted particle size distributions corresponding to 20 mm balls and feed size: - 300 + 212 µm

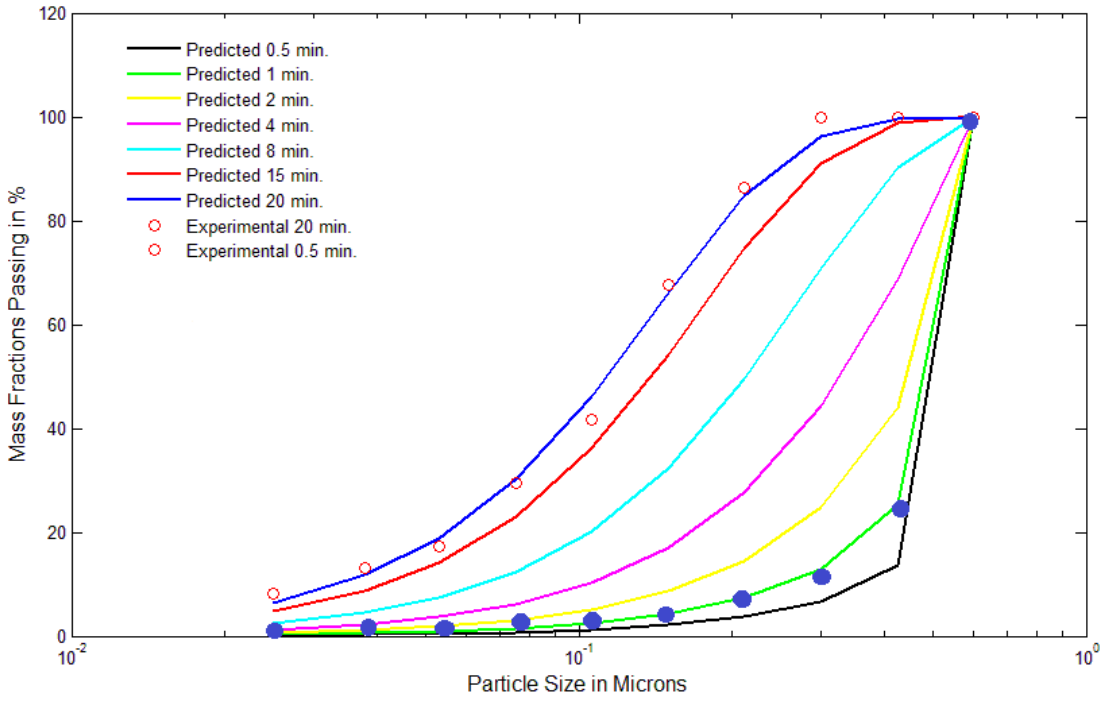


Figure 7.10c Measured and predicted particle size distributions corresponding to 20 mm balls and feed size: - 425 + 300 µm

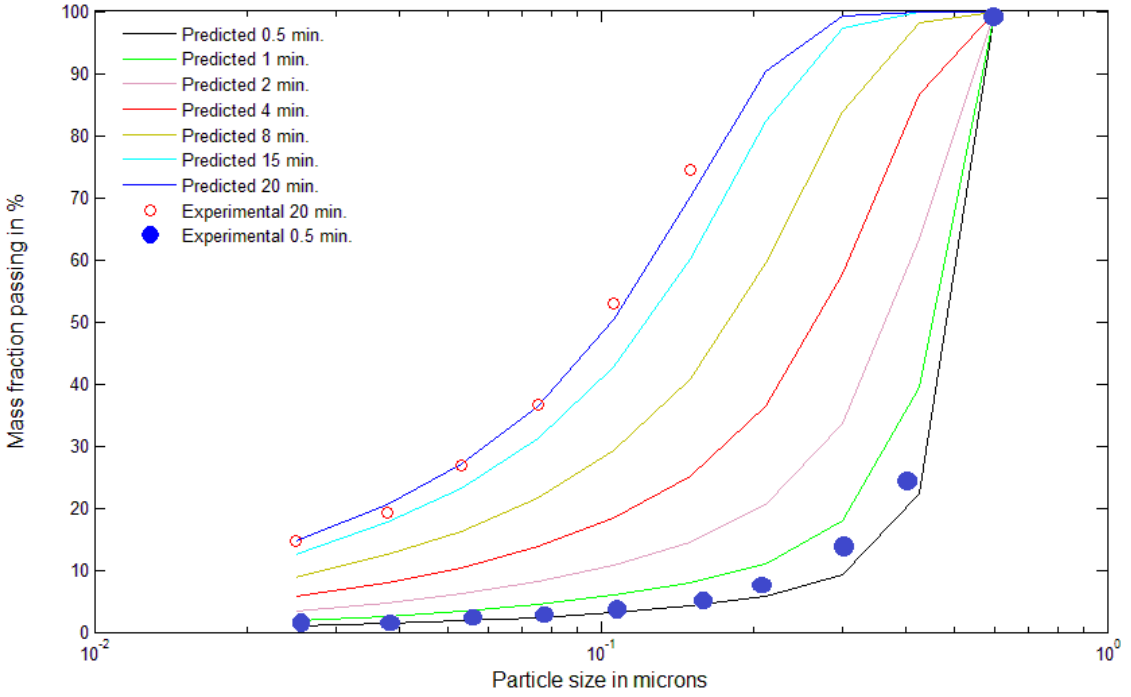


Figure 7.10d Measured and predicted particle size distributions corresponding to 30 mm balls and feed size: -212 + 150 µm

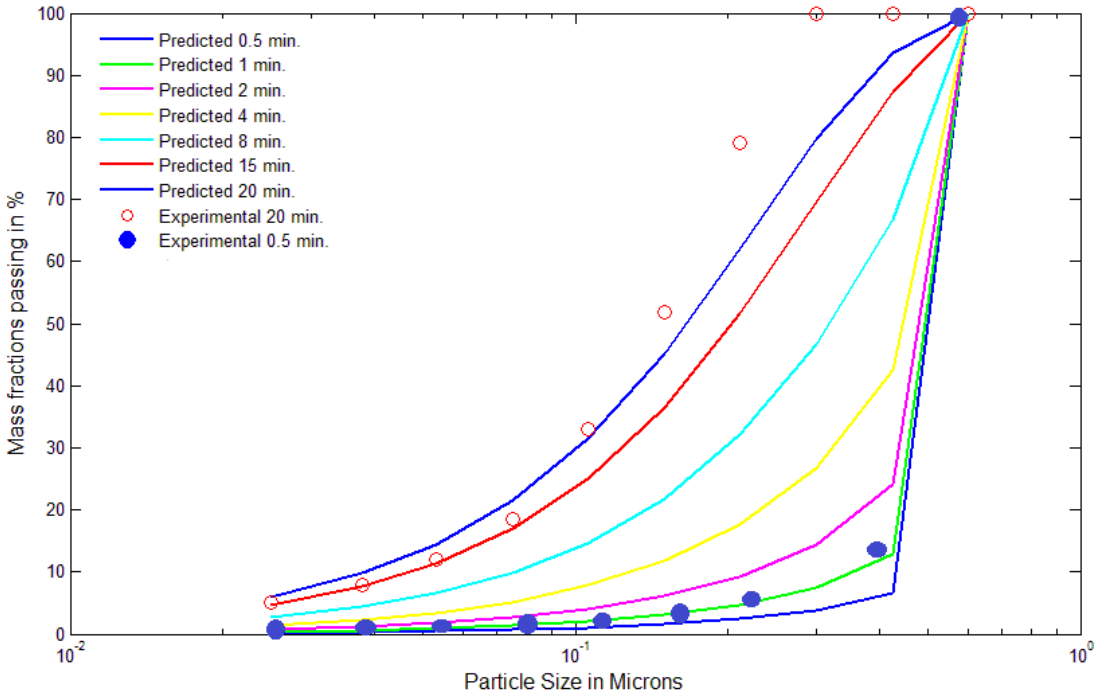


Figure 7.10e Measured and predicted particle size distributions corresponding to 30 mm balls and feed size: - 300 + 212 µm

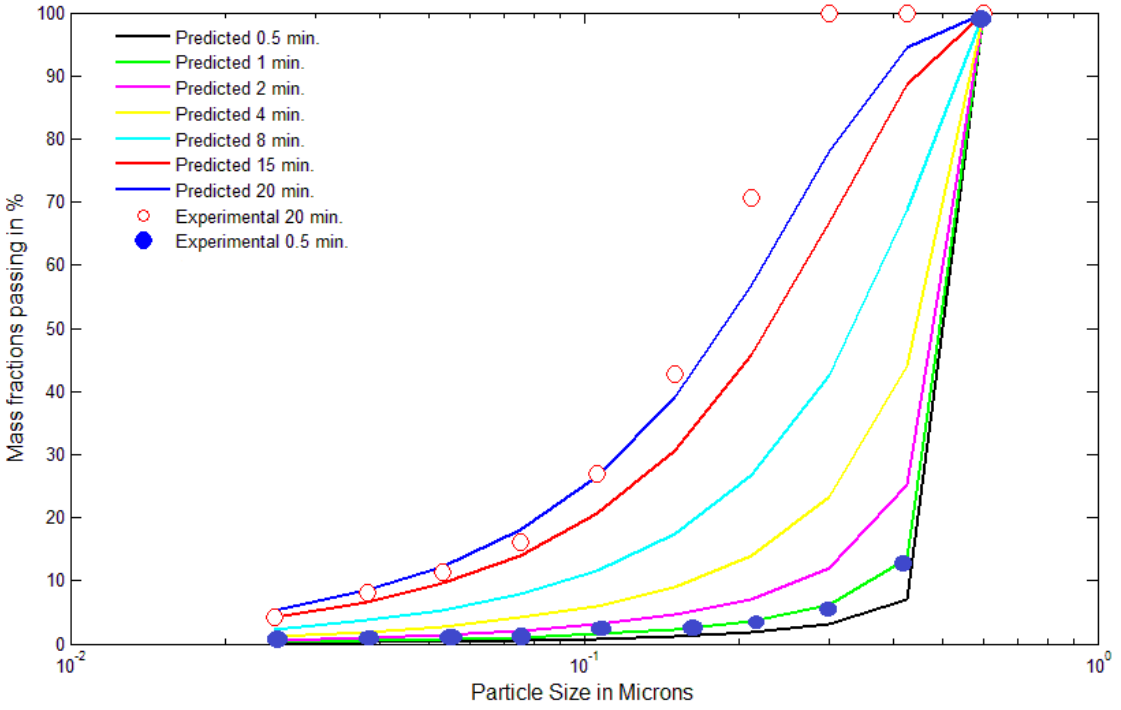


Figure 7.10f Measured and predicted particle size distributions corresponding to 30 mm balls and feed size: - 600 + 425 µm

7.2.3.2 Chromite component particle size distributions

The measured and predicted size distributions for all feed materials are given in **Figs. 7.11 a-f**. The measured size distributions, shown as markers in the plotted graphs, and the simulated size distributions, shown as solids lines matched well. This suggests that the Selection and Breakage Functions parameters obtained can be used to understand the behaviour of the Chromite Component during the ball milling of the UG2 ore. As previously, the predictions gave a relatively coarser product for the shorter grinding time of 0.5 min. Comparing the Selection and Breakage Functions of the UG2 ore (α = 1.31 a = 0.49, γ = 1.34, β = 6.00 and Φ = 0.62) and that of the Chromite Component (α = 1.40, a = 0.54, γ = 1.05, β = 5.30 and Φ = 0.71), one can conclude that the chromite component is significantly softer than the UG2 ore. It turns out that the breakage rate of the chromite component is higher than that of the UG2.

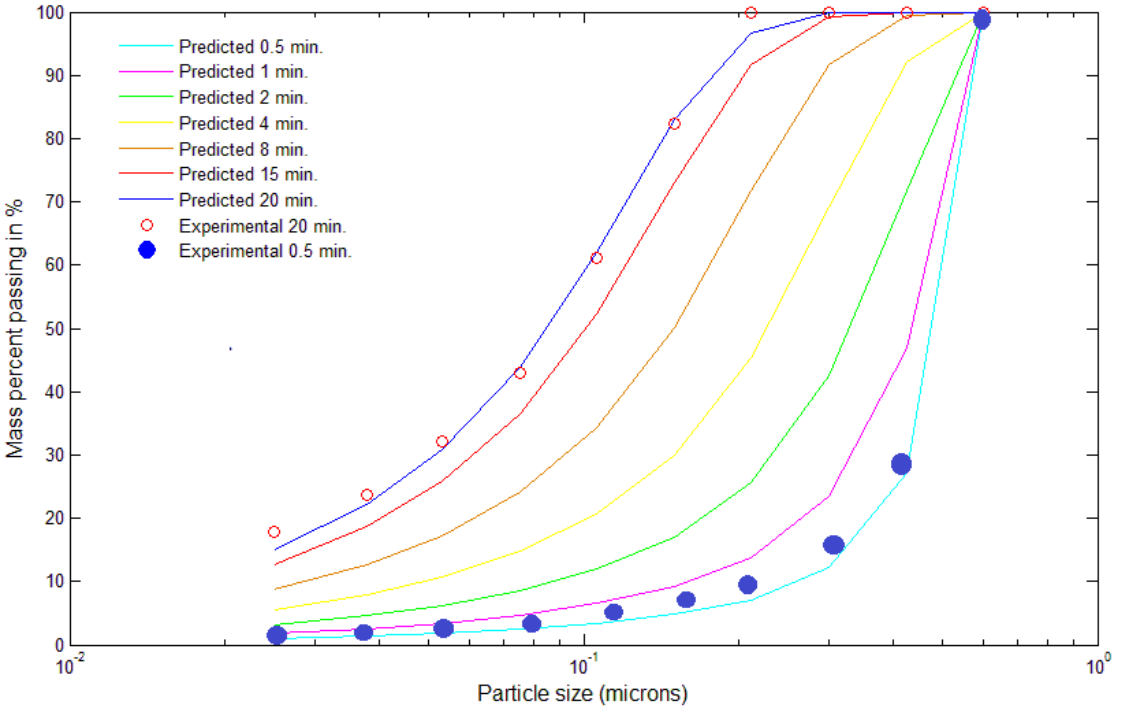


Figure 7.11a Measured and predicted particle size distributions corresponding to 20 mm balls and feed size: -212 + 150 µm

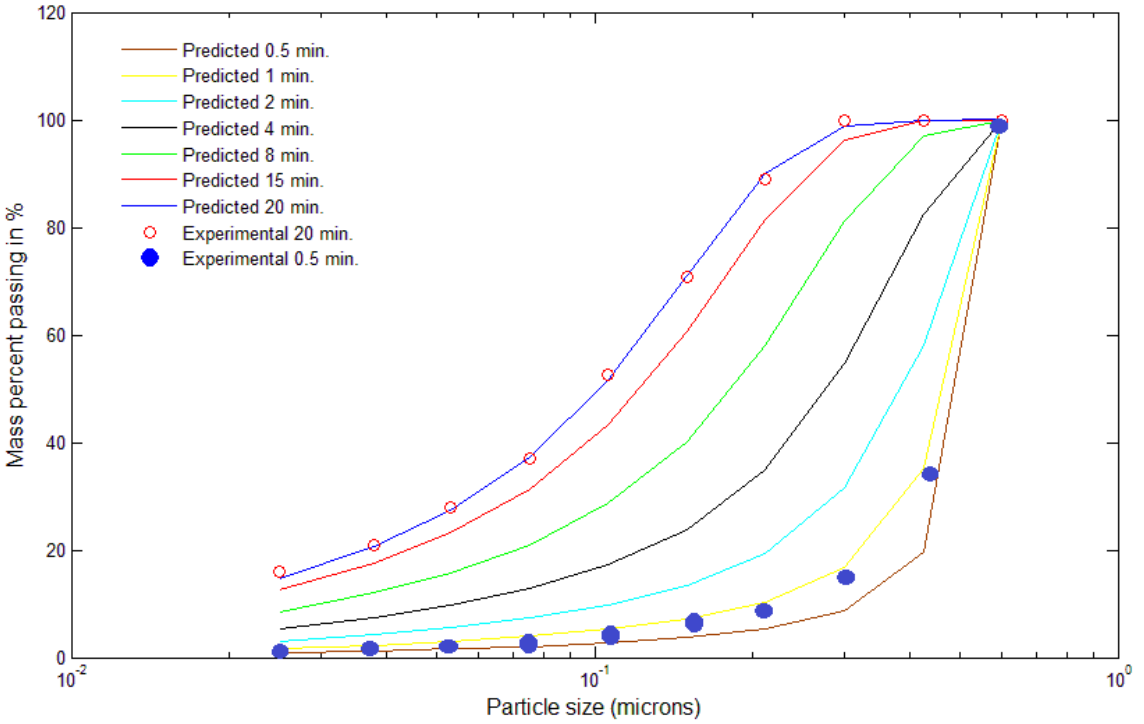


Figure 7.11b Measured and predicted particle size distributions corresponding to 20 mm balls and feed size: - 300 + 212 µm

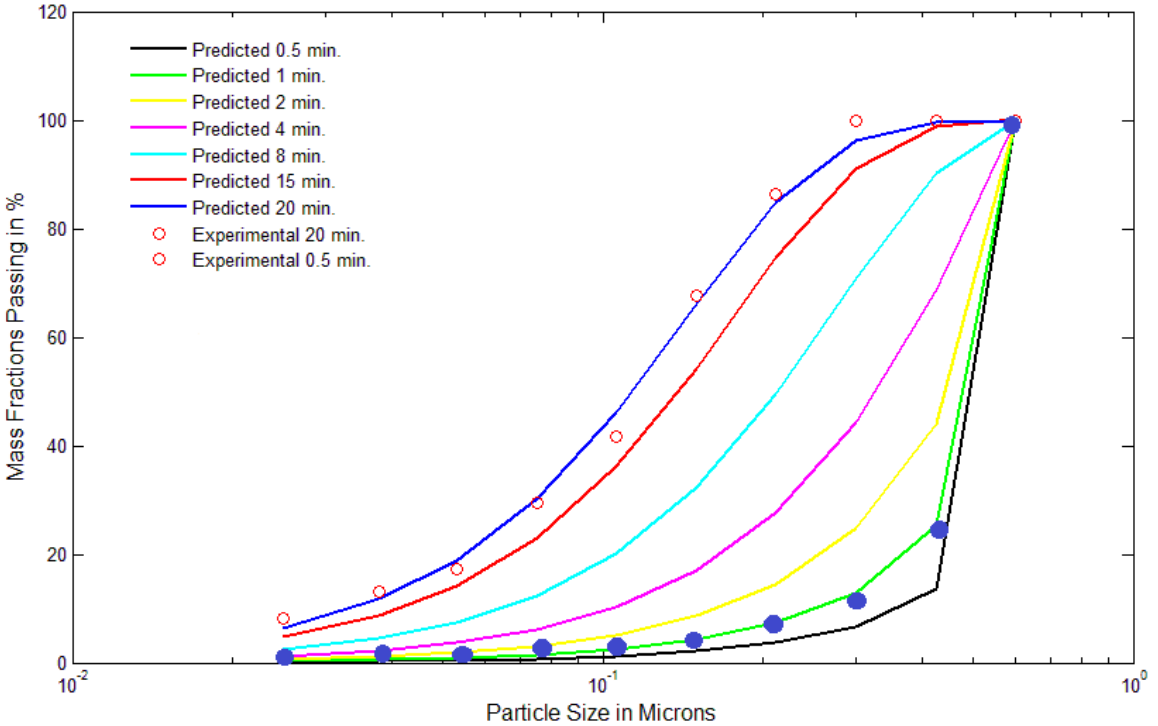


Figure 7.11c Measured and predicted particle size distributions corresponding to 20 mm balls and feed size: - 425 + 300 µm

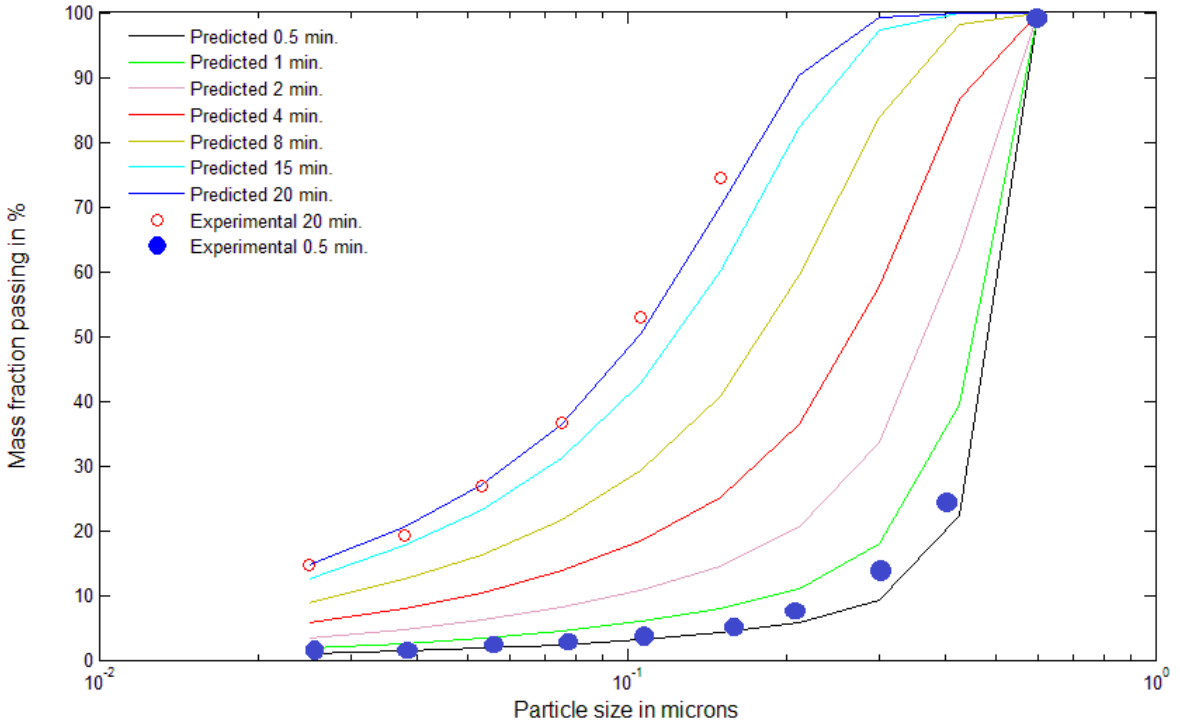


Figure 7.11d Measured and predicted particle size distributions corresponding to 30 mm balls and feed size: -212 + 150 µm

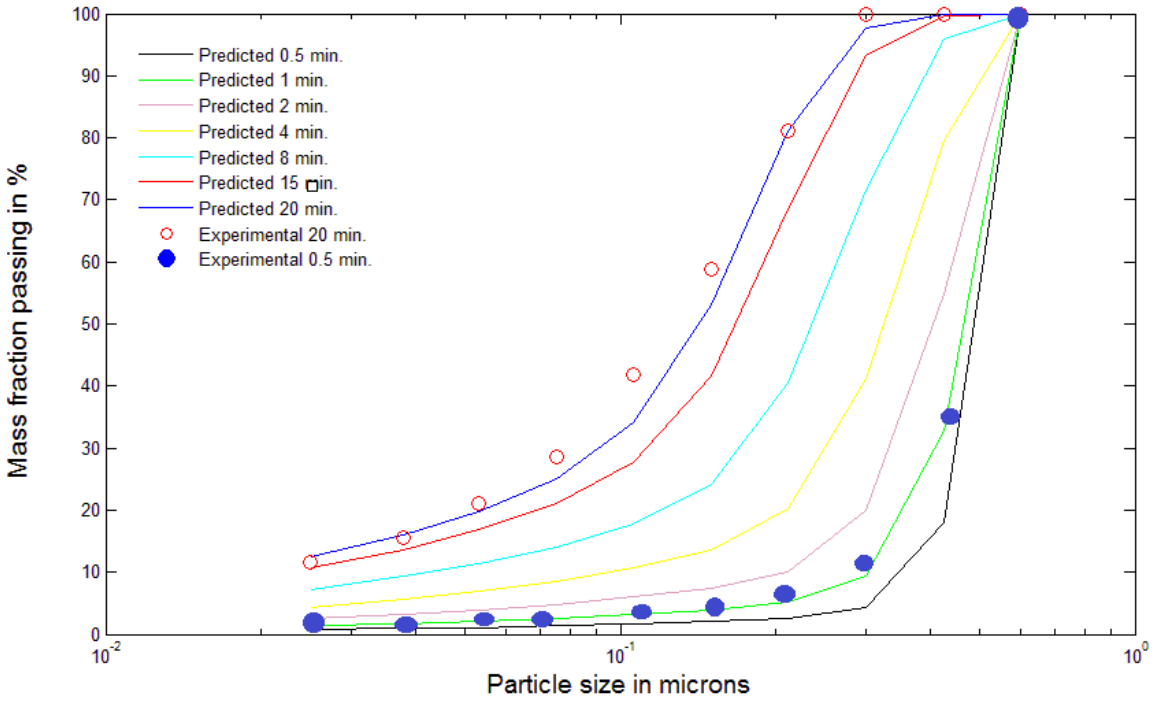


Figure 7.11e Measured and predicted particle size distributions corresponding to 30 mm balls and feed size: - 300 + 212 µm

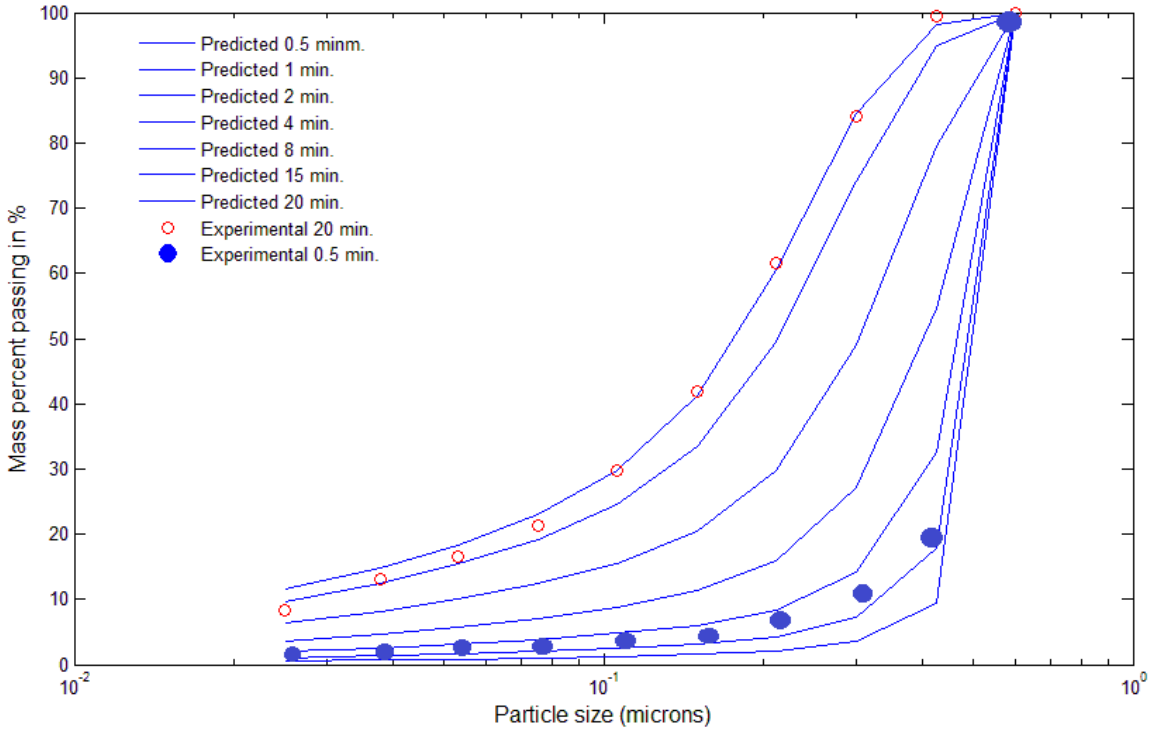


Figure 7.11f Measured and predicted particle size distributions corresponding to 30 mm balls and feed size: - 600 + 425 µm

Chapter 8 Matrix modelling of a closed circuit ball milling

In this Chapter, we develop and present a binary matrix model of a closed circuit ball milling for the UG2 ore. Such a model can help searching for optimal operating conditions of the secondary milling circuit so that a preferential milling of the non-chromite component within the UG2 ore is achieved. This model provides therefore ways of improving the milling circuit by preventing over grinding the chromite component. Let's recall that the UG2 ore has a high content of chromite that results in operational problems in the downstream smelting process. There is then a need to minimise the fine chromite particles in the milling product prior to flotation. In the previous chapter, the $\mathbf{S_i}$ and $\mathbf{b_{ij}}$ Functions were determined for the UG2 ore, in which the chromite and non-chromite components were treated individually. In this chapter, these values were used to model the ball milling circuit, using the matrix modelling approach. The perfectly mixed ball mill model was assumed. This work takes into account only the solid particles. The water system is not treated.

8.1 Flowsheet setup

The closed circuit ball milling design consisted of a ball mill and a classifier (hydrocyclone), as shown in **Fig. 8.1**.

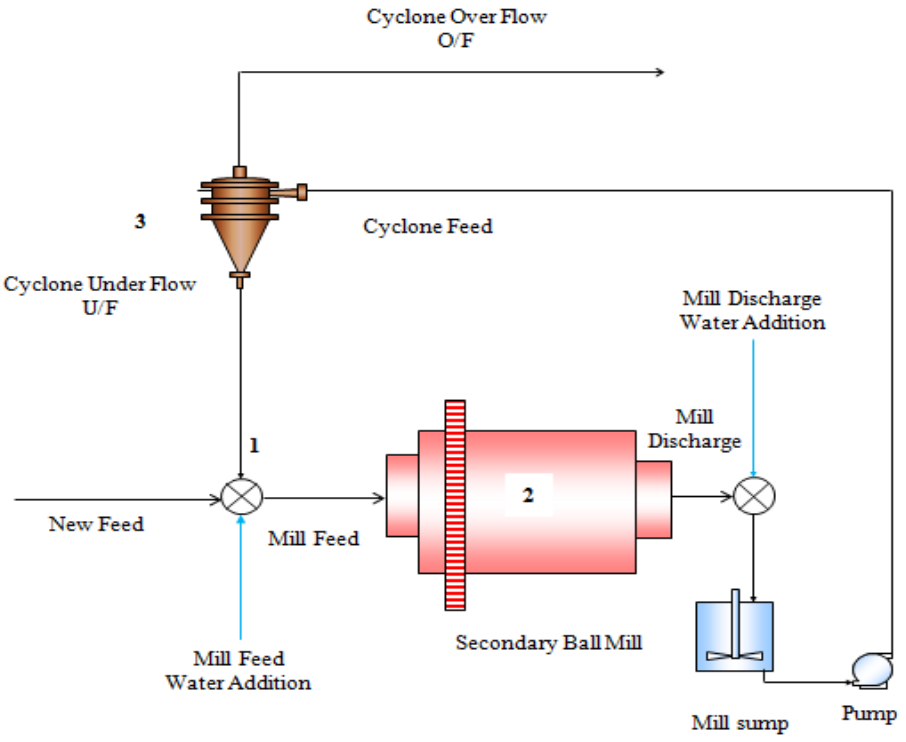


Figure 8.1 Secondary ball milling closed circuit

8.2 Steady-state mass Balancing

The system of material in the ball milling closed circuit is shown in the Figure above. The mass conservation should be carried for all devices and the matrix transformation of incoming and outgoing flows written. The mass balance will then be solved for points 1, 2 and 3.

8.2.1 Mass balance around point 1

The mass balance around the mixing point, as shown in **Fig. 8.2**, can be written as follows

$$F_U + F_{NF} = F_M \tag{8.1}$$

$$\mathrm{F}_U \, \mathbf{p}_\mathbf{U} + \mathrm{F}_{NF} \, \mathbf{p}_\mathbf{NF} = F_M \mathbf{p}_\mathbf{F} \tag{8.2}$$

where p_U, p_{NF} and p_F are weight fractions of size class i; and F_U, F_{NF} and F_M are the mass flows of cyclone underflow, ball mill new feed and mill feed.

Dividing both sides of **Eq. (8.2)** by F_M , one gets

$$\frac{F_U}{F_M}\mathbf{p_U} + \frac{F_{NF}}{F_M}\mathbf{p_{NF}} = \mathbf{p_M} \tag{8.3}$$

Or

$$\alpha\mathbf{p_U} + (1-\alpha)\mathbf{p_{NF}} = \mathbf{p_M} \tag{8.4}$$

where $\alpha = \frac{F_U}{F_M}$ and $1-\alpha = \frac{F_{NF}}{F_M}$

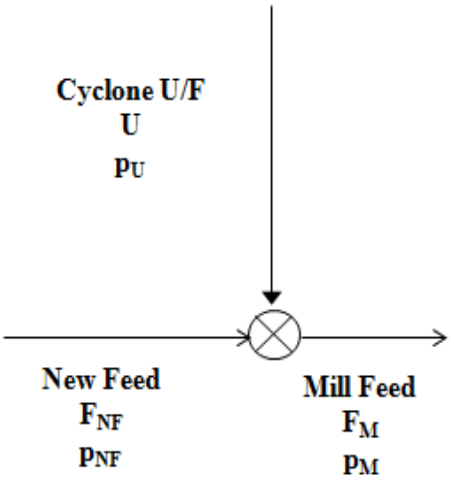


Figure 8.2 Mixing point mass balance

8.2.2 Mass balance around point 2

The mass balance was conducted around the ball mill, on class i. The general model for continuous ball milling operation is shown in **Fig. 8.3**.

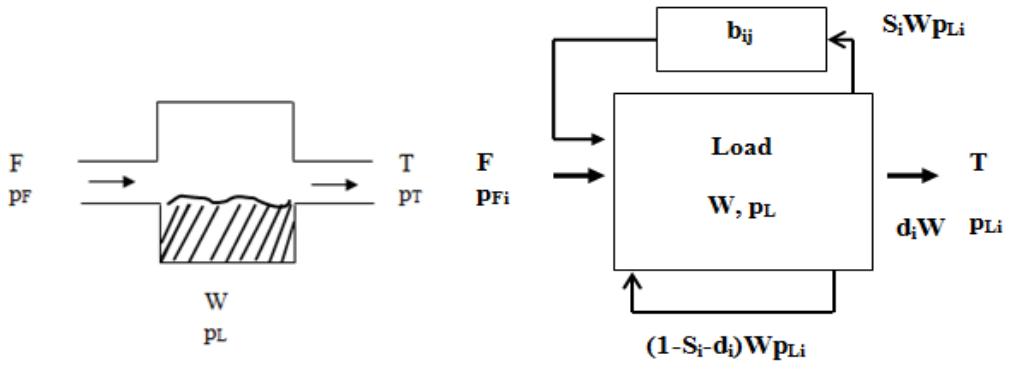


Figure 8.3 Continuous ball milling schematic

The dynamic mass balance on class i is given by the following relationship

$$Fp_{Fi} + W\sum_{j=1}^{i-1} b_{ij} s_j p_{Lj} = d_i W p_{Li} + s_i W p_{Li} + \frac{d}{dt}(W p_{Li}) \tag{8.5}$$

Dividing Eq. (8.3) by F and using matrix notation, one gets

$$p_{FM} + \theta B S p_L = \theta(D+S)\,p_L + \frac{d}{dt}(\theta p_L) \tag{8.6}$$

where $\theta = \frac{W}{F}$ is the average residence time of the material in the mill

B, **S** and **D** are breakage, selection and discharge matrices respectively, of dimension **2N x 2N**.

If the mill is assumed to be perfectly mixed and that there is not classification at the outlet, solving **Eq. (8.6)** for steady state conditions (i.e. $\frac{d(\theta p_L)}{dt} = 0$), one gets

$$\mathbf{p_L} = \frac{1}{\theta}(\mathbf{D} + \mathbf{S} - \mathbf{BS})^{-1}\mathbf{p_{FM}} \tag{8.7}$$

Equation **(8.7)** becomes, with $\mathbf{D} = \frac{\mathbf{I}}{\theta}$

$$\mathbf{p_T} = \theta \mathbf{D} \mathbf{p_L} = \mathbf{D}(\mathbf{D} + \mathbf{S} - \mathbf{BS})^{-1} \mathbf{p_{FM}} \tag{8.8}$$

The transformation matrix of the ball mill **T** is given as follows

$$\mathbf{T} = \left[\theta(\mathbf{D} + \mathbf{S} - \mathbf{BS})\right]^{-1} \tag{8.9}$$

8.2.3 Mass balance around the cyclone

The mass balance was also conducted around the cyclone. The schematic of the cyclone flows is shown in **Fig. 8.4**. Here, $p_{CF,}$ p_U and p_O are the mass percents of the cyclone feed, the underflow and overflow respectively. F_{CF}, U and O denote the flow rate of the cyclone feed, the underflow and overflow respectively. R_F denotes the fraction of the feed that bypassed to the underflow.

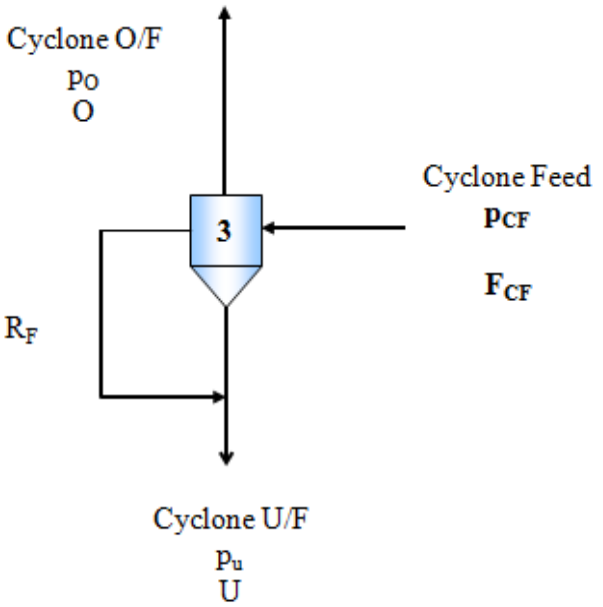


Figure 8.4 Cyclone mass balance

The recovery of feed solids to underflow in the size class i (R_{ui}) is given by **Eq. (8.10)**. The cyclone unit can be also described by the partition curve model shown in **Fig 8.5.**

$$R_{ui} = R_f + (1 - R_f) \times \left(1 - e^{-0.693 \times \left(\frac{x_i}{x_{50c}} \right)^m} \right) \tag{8.10}$$

where

R_f is the water recovery to the underflow (which is assumed to be the same as the recovery of the finest particles)

m is parameter indicating the sharpness of separation and is related to the slope (shown as A/B in **Fig. 8.5**) of the R_{ui} curve at the point of inflection

x is the particle size (m)

x_{50c} is the corrected cut size (m)

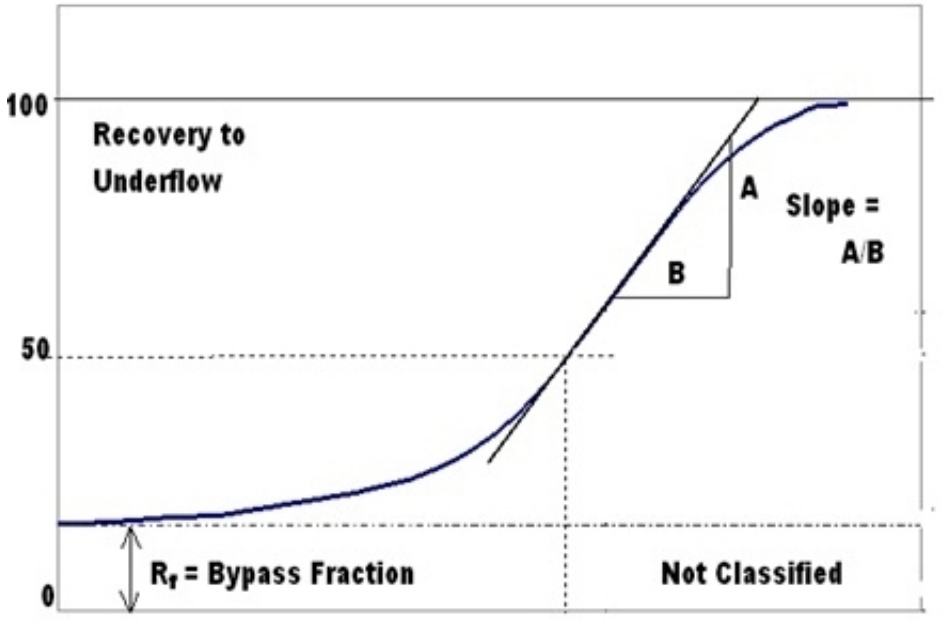


Figure 8.5 Cyclone partition curve (Plitt, 1976)

The effect of particle density on the cut size is given by (8.11)

$$x_{50c} = k_1 \cdot (\rho_{ore} - \rho_{UF})^{k_2} \tag{8.11}$$

where ρ_{ore} is the specific gravity of the cyclone feed material. $\rho_{U/F}$ is the specific gravity for the liquid phase. It normally takes value around the water density. k_1 and k_2 are dimensionless calibration factor. K_2 can take values between -1 and -0.5. For a binary UG2 ore, according to Plitt (1976) we can define the ratio of cut size for the chromite and non-chromite components as follows

$$\frac{x_{50c_chromite}}{x_{50c_non-chromite}} = \left(\frac{\rho_{chromite} - \rho_{UF}}{\rho_{non-chromite} - \rho_{UF}} \right)^{k_2} \tag{8.12}$$

Where the specific gravities of the chromite and non-chromite components ($\rho_{chromite}$ and $\rho_{non-chromite}$) are about 4.32 and 3.24, respectively. Particular attention should be paid to the choice of cut-sizes.

The mass flow rate of the cyclone underflow can be given by

$$U\mathbf{p}_{\mathbf{U}} = \mathbf{C}F_{CF}\mathbf{p}_{\mathbf{CF}} \tag{8.13}$$

The mass flow rate of the cyclone overflow can be then derived as follows

$$O\mathbf{p}_{\mathbf{O}} = (\mathbf{I} - \mathbf{C})F_{CF}\mathbf{p}_{\mathbf{CF}} \tag{8.14}$$

Combining **Eqs. (8.4) and (8.13)**, with $F_M = F_{CF}$ one can get

$$U\mathbf{p}_{\mathbf{U}} = \mathbf{CT}F_{NF}\left[\alpha\mathbf{p}_{\mathbf{U}} + (1-\alpha)\mathbf{p}_{\mathbf{NF}}\right] \tag{8.15}$$

We can also write, with I the identity matrix

$$\mathbf{I}U\mathbf{p}_{\mathbf{U}} = \mathbf{CT}F_{NF}\left[\alpha\mathbf{p}_{\mathbf{U}} + (1-\alpha)\mathbf{p}_{\mathbf{NF}}\right] \tag{8.16}$$

Then

$$U\mathbf{p}_{\mathbf{U}} = \left(\mathbf{I} - \alpha\mathbf{CT}\right)^{-1}\mathbf{CT}(1-\alpha)F_{NF}\mathbf{p}_{\mathbf{NF}} \tag{8.17}$$

Finally, combining **Eqs. (8.13)** and **(8.14)**, $\mathbf{p_O}$ can be derived as follows

$$O\mathbf{p}_{\mathbf{O}} = \left(\mathbf{I} - \mathbf{C}\right)\mathbf{C}^{-1}U\mathbf{p}_{\mathbf{U}} \tag{8.18}$$

We can also write

$$O\mathbf{p}_{\mathbf{O}} = \left(\mathbf{I} - \mathbf{C}\right)\mathbf{C}^{-1}\left(\mathbf{I} - \alpha\mathbf{CT}\right)^{-1}\mathbf{CT}(1-\alpha)F_{NF}\mathbf{p}_{\mathbf{NF}} \tag{8.19}$$

8.3 Matrix representations

This Section shows the form of matrices that have been used for the matrix modelling of a closed circuit ball milling process of a binary material. The vectors mass fraction $\mathbf{p_{FM}}$ and $\mathbf{p_T}$ of size i at time t and time 0 respectively are shown below. These are **2N x 1** vectors**.** The first half Nth elements denote the chromite component and the last half Nth elements denote the non-chromite component.

$$\mathbf{p}_{\mathbf{M}} = \begin{bmatrix} p_{x1} \\ p_{x2} \\ \vdots \\ p_{xN} \\ p_{yN+1} \\ \vdots \\ p_{y2N} \end{bmatrix} \quad \text{and} \quad \mathbf{p}_{\mathbf{T}} = \begin{bmatrix} p_{x'1} \\ p_{x'2} \\ \vdots \\ p_{x'N} \\ p_{y'N+1} \\ \vdots \\ p_{y'2N} \end{bmatrix}$$

S is a diagonal matrix with diagonal elements S_i, I = 1, 2 ...2N. For a binary compound, **S** can be represented by the following matrix.

$$\mathbf{S} = \begin{bmatrix} S_{x1} & 0 & 0 & 0 & 0 & 0 \\ \vdots & \ddots & \vdots & \vdots & \vdots & \vdots \\ 0 & 0 & S_{xN} & 0 & 0 & 0 \\ 0 & 0 & 0 & S_{yN+1} & 0 & 0 \\ \vdots & \vdots & \vdots & \vdots & \ddots & \vdots \\ 0 & 0 & 0 & 0 & 0 & S_{y2N} \end{bmatrix}$$

B is a lower triangular matrix with elements b_{ij}, $2N \geq i > j \geq 1$. For a binary ore, B can be represented by the following matrix.

$$\mathbf{B} = \begin{bmatrix} 0 & 0 & \dots & 0 & 0 & 0 & 0 & \dots & 0 & 0 \\ b_{x21} & 0 & \dots & 0 & 0 & 0 & 0 & \dots & 0 & 0 \\ b_{x31} & b_{x32} & \dots & 0 & 0 & 0 & 0 & \dots & 0 & 0 \\ \dots & \dots & \dots & 0 & 0 & 0 & 0 & \dots & 0 & 0 \\ b_{xN1} & b_{xN2} & \dots & b_{xNN-1} & 0 & 0 & 0 & \dots & 0 & 0 \\ 0 & 0 & \dots & 0 & 0 & b_{yN+1N} & 0 & \dots & 0 & 0 \\ 0 & 0 & \dots & 0 & 0 & b_{yN+2N} & b_{yN+2N+1} & \dots & 0 & 0 \\ \dots & \dots & \dots & 0 & 0 & \dots & \dots & \dots & 0 & 0 \\ 0 & 0 & \dots & 0 & 0 & b_{y2NN} & b_{y2NN+1} & \dots & b_{y2N2N-1} & 0 \end{bmatrix}$$

The discharge matrix can be represented as follows

$$\mathbf{D} = \begin{bmatrix} D_{x1} & 0 & 0 & 0 & 0 & 0 \\ \vdots & \ddots & \vdots & \vdots & \vdots & \vdots \\ 0 & 0 & D_{xN} & 0 & 0 & 0 \\ 0 & 0 & 0 & D_{yN+1} & 0 & 0 \\ \vdots & \vdots & \vdots & \vdots & \ddots & \vdots \\ 0 & 0 & 0 & 0 & 0 & D_{y2N} \end{bmatrix}$$

Similarly the cyclone partition curve coefficients matrix can be represented as follows

$$\mathbf{C} = \begin{bmatrix} C_{x1} & 0 & 0 & 0 & 0 & 0 \\ \vdots & \ddots & \vdots & \vdots & \vdots & \vdots \\ 0 & 0 & C_{xN} & 0 & 0 & 0 \\ 0 & 0 & 0 & C_{yN+1} & 0 & 0 \\ \vdots & \vdots & \vdots & \vdots & \ddots & \vdots \\ 0 & 0 & 0 & 0 & 0 & C_{y2N} \end{bmatrix}$$

8.4 Model calibration

The sliming of chromite during flotation imposes some constraints to be taken into account during ball milling. The model parameters were determined based on the model predictions and were adjusted so as to minimise the chromite slimes (- 38 µm) in the overflow stream, and to promote preferential grinding and preferential classification. The ball milling was assumed to be perfectly mixed. Given the S and B data, after the mass balance, the average residence time obtained for the solids in the ball mill (**θ**) was 7.2 minutes.

The cyclone parameters were chosen as realistic as possible. A very coarse cut-size (greater than 100 µm) is not desirable for non-chromite particles. This is

because PGMs associated with BMS are locked in the coarse non-chromite particles (mostly silicates) and cannot be floated selectively. This will lead undoubtedly to PGM losses in the secondary flotation circuit. The calculated chromite and non-chromite components cut-sizes obtained were 54.88 µm and 66.82 µm respectively, for k_1 = 100 (chosen arbitrarily to get reasonable values for the cut-sizes) and k_2 = -0.5. The ratio of chromite cut-size to non-chromite cut-size was about 0.82. The sharpness of separation (m) and the bypass to the underflow (R_f) were assumed to be independent of the mineral type (m=3 and R_f=15 per cent).

8.5 Mass Balancing

To evaluate the performance of the grinding circuit model Eq. (8.19), mass balancing studies were carried out by using 100 tons per hour as fresh ball mill throughput. The average residence time obtained for the solids in the ball mill (**θ**) was 7.2 minutes. The mass balance was also aimed to validate the matrix grinding circuit model. The total mass balance of solids in the grinding circuit is given in **Table 8.1**.

Table 8.1 Grinding circuit mass balance (tons per hour)

Ore/ Mineral	Fresh Feed	Mill Feed	Mill Discharge	Cyclone Feed	Cyclone U'flow	Cyclone O'flow	Circulating load
UG2 ore	100.00	540.27	540.27	540.27	440.27	100.00	440.27
Chromite	16.26	105.99	105.99	105.99	89.73	16.26	551.86
Non-chromite	83.74	434.28	434.28	434.28	350.54	83.74	418.61

The higher circulating load of the chromite component tells us that most of the chromite fed to the circuit, are recycled from the cyclone to the ball mill.

8.6 Computer simulation

8.6.1 Ball milling and cyclone classification options for UG2 ores

Simulations were run in excel to explore the milling and classification options for UG2 ore. Four scenarios were examined. In the first scenario, the actual measured selection functions (Si) of chromite and non-chromite, provided by the batch milling tests were used together with the calculated cut-size of chromite and non-chromite (a). In the second scenario the average measured selection function of chromite and non-chromite were used together with the calculated cut-sizes of chromite and non-chromite (b). In the third scenario the average calculated cut-size of the chromite and non-chromite was used together with the measured Si (c). In the fourth scenario the average measured selection function and average calculated cut-size of chromite and non-chromite were used (d).

8.6.2 Simulation results

The different particle size distributions of the cyclone overflow for different scenarios are presented in **Fig. 8.6**.

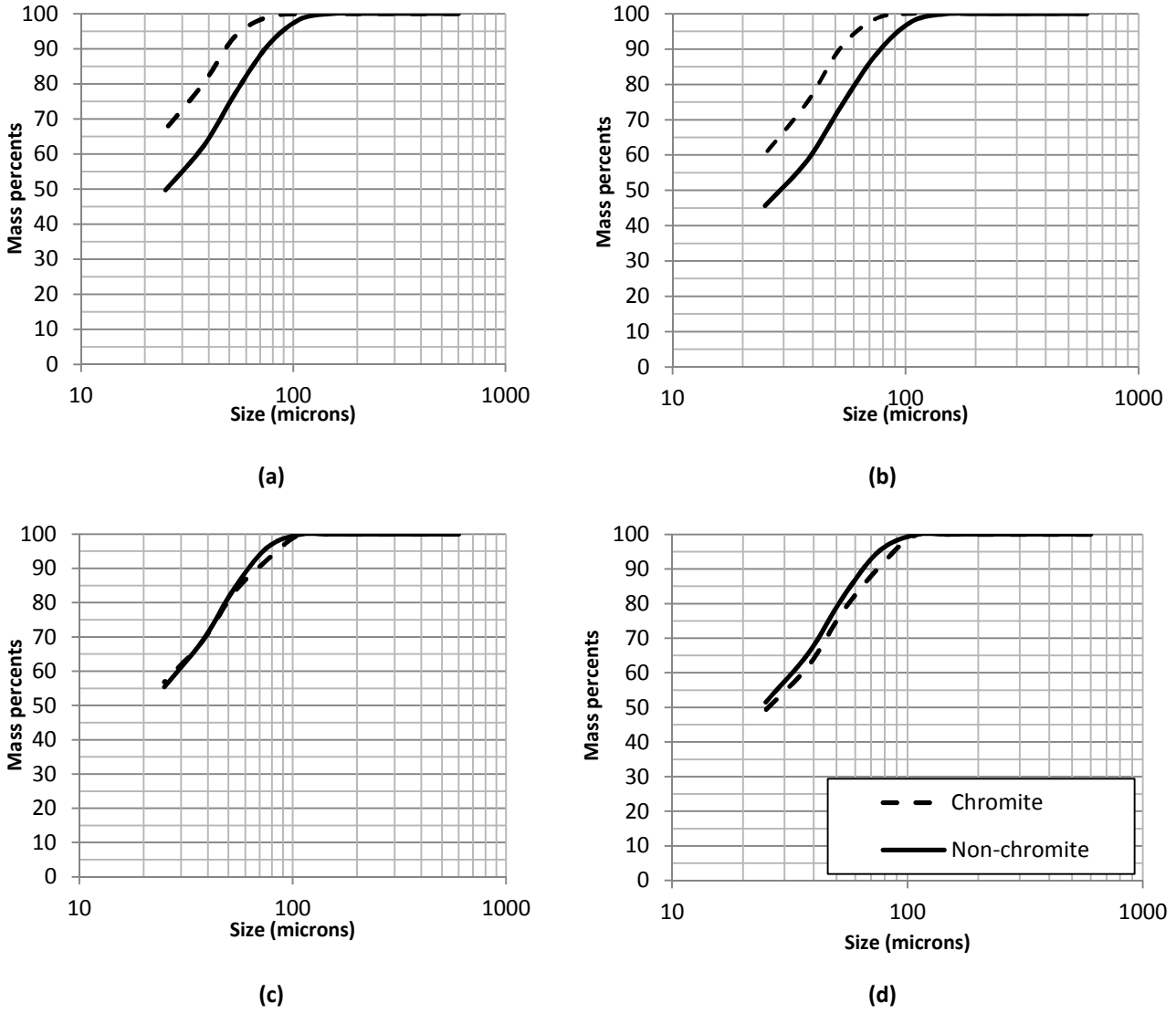


Figure 8.6 Showing chromite and non-chromite particle size distributions in the Cyclone overflow stream for different scenarios

It can be seen that there is a clear interval between the particle size distributions of chromite and non-chromite in **Fig. 8.6(a)** and **Fig. 8.6(b).** Use of the average values of Si [scenario (b)] led to a decrease in fine particles (-38 µm) in the cyclone O/F product of about 8 %. It is obvious that the change in the selection function values affected the simulated grinding quality, since the selection function depend on the milling conditions. It can also be seen that the cyclone overflow stream contains fine chromite particles and coarse non-chromite particles (with locked PGMs). This is undoubtedly the result of using different

cyclone efficiencies for chromite and non-chromite. It is evident that the results will be significantly improved by increasing the cyclone efficiency.

In **Fig. 8.6(c)** and Fig. **8.6(d)**, the average cut-size was used for both chromite and non-chromite. As a result, there is not a clear interval between the particle size distributions of chromite and non-chromite in the cyclone O/F. Again, use of the average values of Si [scenario (d)] led to a decrease in fine particles (-38 μm) in the cyclone O/F product of about 5 %.

With respect to the above scenarios, the second scenario gave good results in terms chromite slimes minimisation during ball milling and separate classification of products at the cyclone. In order to optimise the milling circuit of UG2 ores, the simulations showed that overgrinding of both UG2 components (chromite and non-chromite) should be avoided by applying the same milling conditions. Also, different efficiencies for chromite and non-chromite should be applied at the cyclone.

8.7 CONCLUSION

The matrix model developed can be useful to provide insight into individual mineral behaviour in milling circuits by using routine laboratory batch milling test results. Simulations showed that operating the ball mill circuit in closed circuit with a cyclone can provide good results in terms of preferential grinding and classification for the UG2 ore components. The best option to pursue for the milling circuit of UG2 ores is to apply the same milling conditions (overgrinding should be avoided) for both UG2 components and differential cyclone efficiencies. Such information can play a useful role in guiding the optimisation of grinding circuits. The model can be implemented on integrated grinding circuit models. This will result in the improvement of actual industrial platinum ore flowsheets and chromite sliming in the downstream processes. An open circuit operation of the UG2 ore mill should offer more significant benefits compared to

the closed circuit option. The open circuit option would help saving energy spent on recycling and chromite overmilling in the close circuit; however, this aspect was not considered in this research work.

Chapter 9 Conclusions and Recommendations

An understanding of the UG2 ore milling process and factors affecting it have been enhanced. The data collected from the mill at Mintek were analysed. The information gathered included effect of rotational mill speed, liner profile, ball size and specific power consumption on the grinding and the chromite behaviour along the size fractions. The mill power draw reached the peak with use of the 45° face angle liners whereas, use of square face angle liners resulted in the mill drawing the least power within the mill speed range considered in this work. In connection with the actual research work conducted, 45° face angle liners would be recommended for the milling of UG2 ore. The results also indicated that small balls enhanced considerably the grind as compared to large balls with the same specific energy input. Suffice to say that the use of small balls or a graded ball charge is advisable, to gain both in capacity and efficiency. In addition, the results indicated that the mill rotational speed has very little impact on the grinding process for the conditions considered in this work. These findings agree with our DEM simulation predictions.

A model that relates the chromite content to the size fraction density was developed successfully. This indicated that the chromite content along the size fractions can be determined easily knowing their relative densities.

Further, the UG2 grindability and the distribution of primary daughter fragments was determined for the linear S & B grinding model for conventional ball mills. The Selection and Breakage Functions model parameters as affected by ball size for the chromite and non-chromite components were estimated. These data were used to develop a matrix transformation model of a standard closed grinding circuit. Such a model can be very beneficial for platinum producers in their quest to optimize. It gives a very good insight into individual mineral

behaviour in the milling circuits. It is however recommended that further work be undertaken to optimise the joint integrated milling-flotation performance at the same time.

References

Austin, L.G., 1982. Rate Equations for Non-Linear Breakage in Mills Due to Materials Effects. Powder Technology, pp. 127 – 133

Austin, L.G., Klimpel, R.R., 1984. Modelling for Scale- up of Tumbling Ball Mills: Control '84. Society of Mining Engineers of the AIME, New York, pp. 167 – 184

Bond, F.C., 1961. Crushing and Grinding Calculations, Part 1, British Chemical Engineers, vol. 6, pp. 378 – 385

Bryson, M., 2004. Mineralogical control of minerals processing circuit design. The South African Institute of Mining and Metallurgy, vol. 104, no. 6, p. 307

Chimwani, N., Glasser, D., Hildebrandt, D., Metzger, M.J., Mulenga, F.K., 2012. Determination of the milling parameters of a platinum group minerals ore to optimize product size distribution for flotation purposes. Minerals Engineering, vol. 43–44, pp. 67–78

Cleary, P. W., 2006. Review of DEM and its industrial applications. Orlando, USA

Cundall, P.A., Strack, O.D.L., 1979. A discrete numerical model for granular assemblies. Geothechnique, vol. 29, no. 1, pp. 47 – 65

Daellenbach, C.B., 1985. Chromium-Chromite. Proceedings of Bureau of Mines Briefing Held at Oregon State University, Corvallis, OR, June 4-5, 1985

Fuerstenau, D.A., 1986. Material transport in ball mills: Effect of discharge end design. Powder Technology, vol. 46, pp. 273 – 279

Fuerstenau, D.W., Kapur, P.C., Velamakanni, B., 1990. A multi-torque model for the effects of dispersants and slurry viscosity on ball milling. International Journal of Mineral Processing, vol. 28, no. 1 – 2, pp. 81 – 98

Gardner, R.P., 1975. A Two Mechanistic Approach for the Comminution of Material that exhibits Heterogeneous Breakage Characteristics. Powder Technology, 12:247-258

Güler, T., Akdemir, Ü., 2011. Statistical Evaluation of Flotation and Entrainment Behavior or an Artifical Ore. Transactions of Nonferrous Metals Society of China, vol 22, pp 199−205

Hay, M.P., Schroeder, G., 2005. Use of the SUPASIM flotation model in optimizing Impala's UG2 circuit. Minerals Engineering, vol 18, pp 772-784

Hogg, R., Fuerstenau, D.W., 1972. Power relationships for tumbling mills. SME – AIME Transactions, vol. 252, pp. 418 – 423

http://www.mathworks.com/help/optim/ug/constrained-nonlinear-optimization-algorithms.html

Jonsén, P., Pålsson, B., Tano, K., Berggren, A., 2010. Prediction of mill structure behaviour in a tumbling mill. Technology and Development, Boliden Minerals, SE-93681 Boliden, Sweden

Kalala, J.T., Breetzke, M., Moys, M.H., 2007. Study of the influence of liner wear on the load behaviour of an industrial dry tumbling mill using the Discrete Element Method (DEM). International Journal of Mineral Processing, vol. 86, no. 1/4, pp. 33 – 39

Katubilwa, F.M., Moys, M.H., 2011. Effect of ball size distribution on milling rate. Minerals Engineering, vol. 22, no. 13, pp. 1583 – 1288

Kendall, T., 2003. Platinum 2003: Johnson Matthey plc., London

King, R.P., 2000. Technical notes 8 grinding

Levin, J., 1989. Observations on the Bond standard grindability test, and a proposal for a standard grindability test for fine materials. Journal of the South African Institute of mining and Metallurgy, vol. 89, no. 1, pp. 13 – 21

Liddell, K., 2009. 25 Years of UG2 concentrators. A celebration of Technology Conference. Mintek 75', Randburg

Liddell, K.S., Moys, M.H., 1988. Effects of mill speed and filling on the behaviour of the load in a rotary grinding mill. The South African Institute of Mining and Metallurgy, pp. 49 – 57

Loveday, B.K., 2010. The small pebble process for reducing ball and power consumption in secondary grinding. XXV International Mineral Processing Congress (MPC) 2010 Proceedings, Brisbane, QLD, Australia, 6 – 10 September 2010

Lynch, A.J., Whiten, W.J. & Narayanan, S.S., 1986. Ball mill models: Their evolution and present status. Arbiter Symposium 48-66

Maharaj, L., 2011. Optimal design of a secondary milling circuit for treating chromite-rich UG2 platinum ores. PhD thesis, University of KwaZulu-Natal

Mailula, T., Bradshaw, D., Harris, P., 2003. The effect of copper sulphate addition on the recovery of chromite in the flotation of UG2 ore. The South African Institute of Mining and Metallurgy, vol. 103, no. 2, p. 143

Mainza, A.P., 2004. Differential classification of dense material in a three-product cyclone. Minerals Engineering, vol. 17, pp. 573 – 579

Makokha, A.B., Moys, M.H., 2006. Effect of cone-lifters on the discharge capacity of the mill product Case study of a dry laboratory scale air-swept ball mill. Minerals Engineering, vol. 20, no. 2, pp. 124 – 131

Mckenzie, A., 1996. The presence of spinel during matte smelting. Proc. Trends in Base Metal Smelting and Refining, Johannesburg

McLaren, C.D., 1982. The platinum-group chemistry and mineralogy of the UG-2 chromite layer of the bushveld complex. Economic Geology, vol. 77, pp. 1848 – 1866

Meaders, R., MacPherson, A., 1964. Technical design of autogenous mills. Mining Engineering, pp. 81 – 83

Modelling of entrainment in industrial flotation cells: Water recovery and degree of entrainment: Water recovery and degree of entrainment [J]. Minerals Engineering, 2006, 19: 1191−1203.

Morrell, S., 1993. The prediction of power draw in wet tumbling mills, PhD. Thesis, University of Brisbane.

Neethling, S.J., Cilliers, J.J., 2009. The entrainment factor in froth flotation: model for particle size and other operating parameter effects. Int. J. Miner. Process. Vol 93, pp 141–148

Penberthy, C.O., 2000. The recovery of platinumgroup elements from the UG-2 chromite, Bushveld Complex – A mineralogical perspective. Mineralogy and Petrology, vol. 68, pp. 213 – 222

Plitt, L.R., 1976. A mathematical Model for the Hydrocyclone Classifier. CIM Bulletin, vol. 69, p. 114

Powell, M., 1988. A survey of the milling and mill-lining practice of South Afican gold mines. Mintek Report M350/25, Johannesburg

Powell, M., 1991. The design of rotary-mill liners, and their backing materials. Journal of the South African Institute of mining and Metallurgy, vol. 91(2) , pp. 63 – 75

Powell, M., Vermeulen, L., 1994. The Influence of Liner Design on the Rate of Production of fines in a Rotary Mill. Minerals Engineering, Vol. 7, Nos 2/3, pp. 169-183

Powell, M., Weerasekara, N., Cole, S., LaRoche, R., Favier, J., 2011. DEM modelling of liner evolution and its influence on grinding rate in ball mills. Minerals Engineering, Vol. 24, Nos 3/4, pp. 341-351

Schumann, R., 1960. Energy Input and Size Distribution in Comminution. Trans. A.I.M.E., vol. 217, pp. 22-25.

Tangsathitkulchai, C., 2003. The effect of slurry rheology on fine grinding in a laboratory ball mill. International Journal of Mineral Processing, vol. 69, pp. 29 – 47

U.S. Geological Survey (USGS), 2011. Mineral Commodity Summaries. http://www.usgs.gov:http://www.polinares.eu/docs/d2-1/polinares_wp2_annex2_factsheet1_v1_10.pdf, Retrieved July 2012

Vermeulen, L.A., 1986. Contribution to ball wears and ball size distributions in tumbling ball mills. Powder Technology vol. 46, pp. 281-285

Appendices

A.1 Wits DEM Simulator Graphic User Interface (GUI)

A.1.1 Getting started with Wits DEM Simulator

Upon launching the simulator, a window similar to **Fig. A.1.1 (a)** pops up with several functionalities.

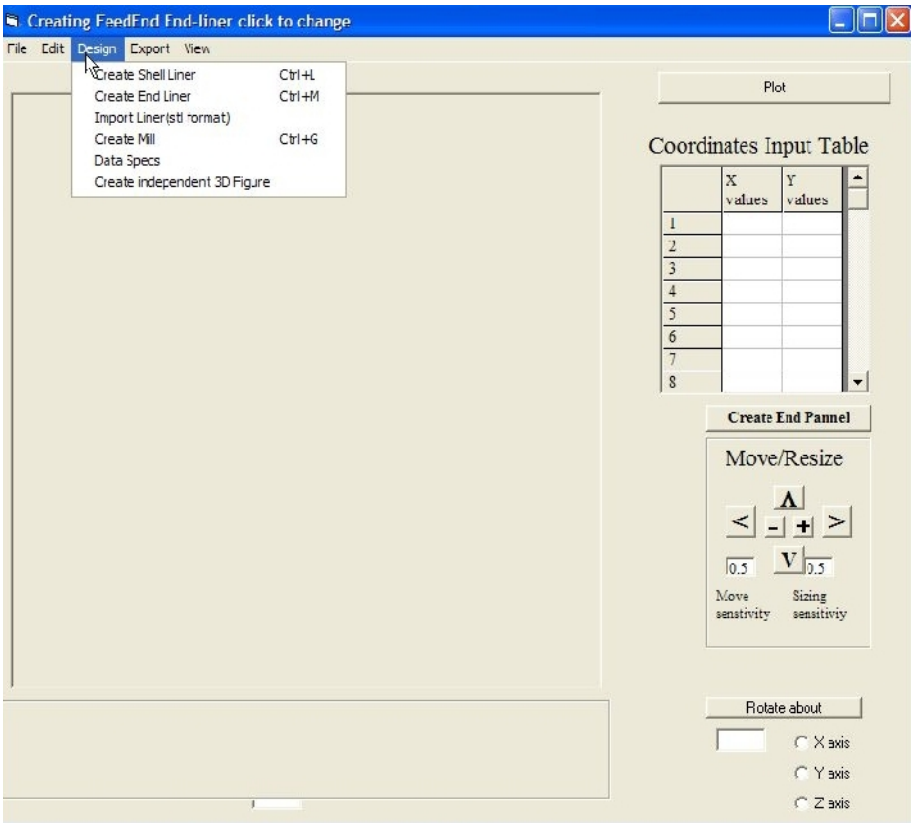


Figure A.1.1 (a) DEM Simulator presentation

Text boxes are quite self-explanatory and straightforward. However, one of the first things to do is to draw the profile of lifters to be used. To do that, one clicks the 'Design' button that brings up **Fig. A.1.1 (b)** below. A Click on 'create end panel' button under 'design' button calls up text boxes where one specifies the

liner profile coordinate points in the Coordinates Input Table. These points are the result of the cutaway view of the liner profile and the x-y plane. For example, the points (0, 0), (0, 1.5), (2, 1.5) and (2, 0) correspond to the square lifter. Once the profile of the lifter is designed, enter the mill diameter, the mill length, the liner length and the number of liners and then press the create mill button under design button to view the full shape.

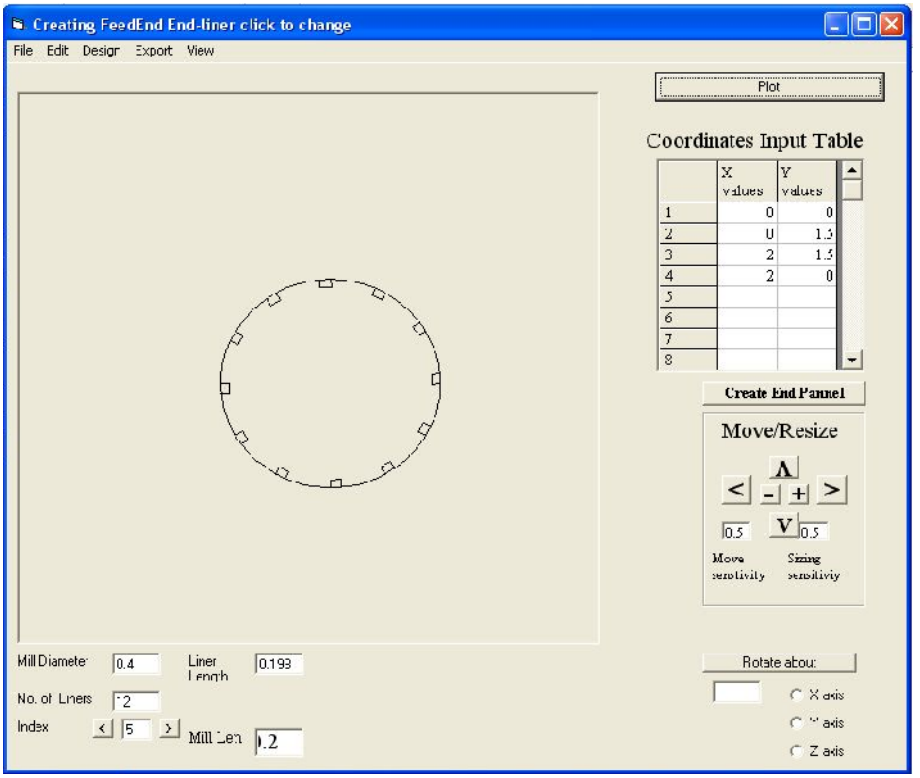


Figure A.1.1 (b) DEM software presentation

A.1.2 Formatting input and output data

Upon termination of the design of lifters, one can enter all information pertaining to milling conditions and DEM parameters by pressing the 'Data Specs' button in **Fig. A.1.2**. Then the Ball size distribution used and the contact parameters are defined. The software also loads with materials of different densities.

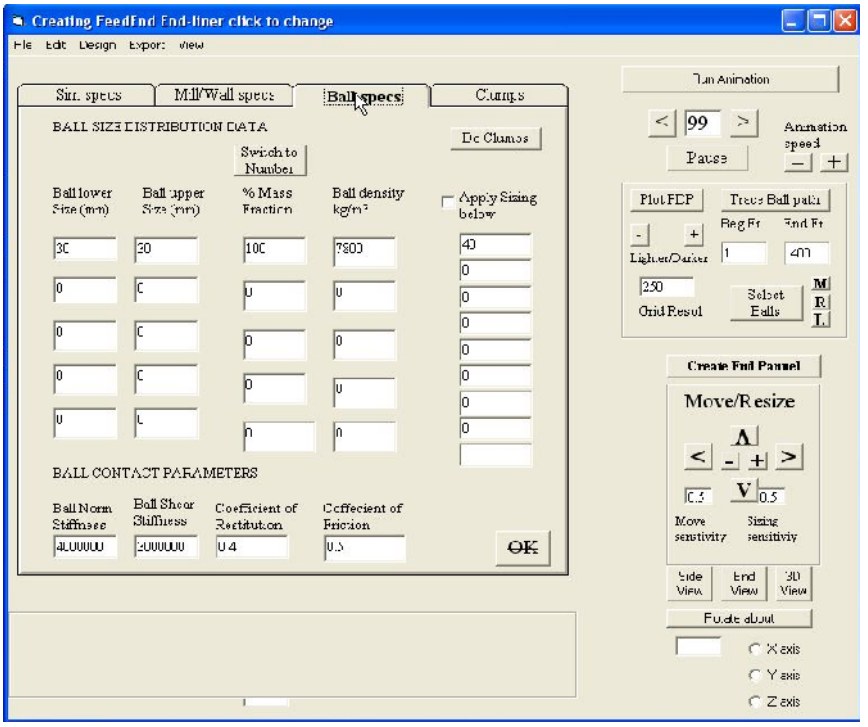


Figure A.1.2 DEM software presentation

A.1.3 Post simulation steps

After the simulation data are generated, in the 'View' panel, one can click on 'Run Animation' to see different frames, as shown in **Fig. A.1.3**. The desired Animation speed can also be set. The simulated mill can be viewed from different angles by pressing on 'Side View', 'End View' or in 3D by pressing on '3D View'. It is also possible to follow the trajectory of a single ball by pressing 'Select the balls'.

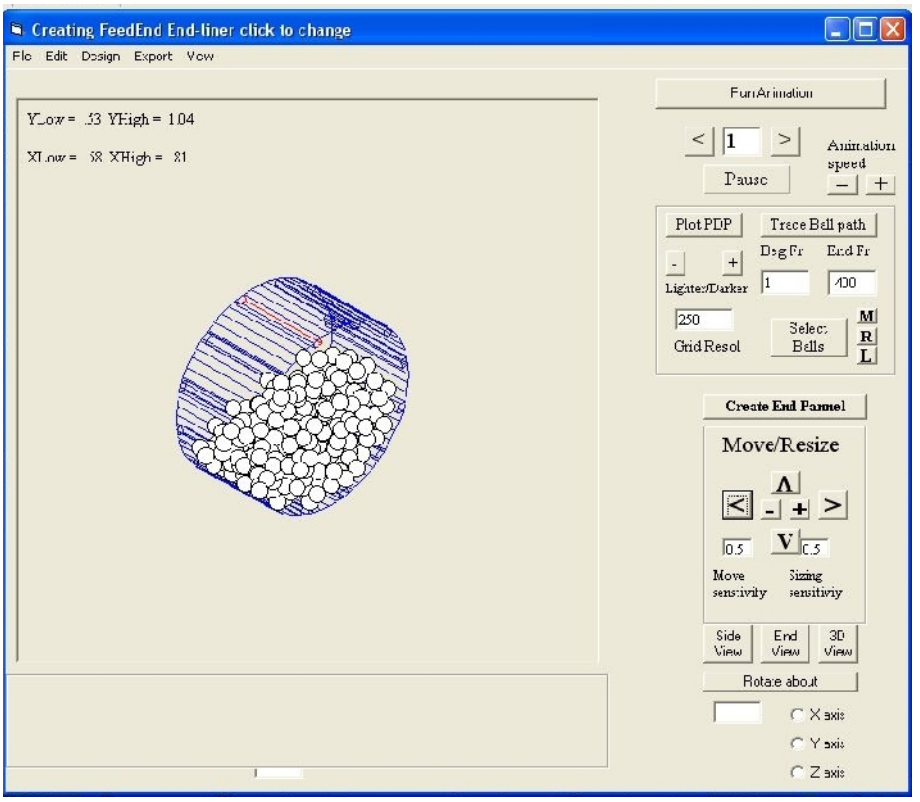


Figure A.1.3 DEM software presentation

A.1.4 DEM results collection

The first and foremost result of DEM simulation is a picture of actual charge motion followed by force distribution, power draw and impact energy spectra. The charge motion image is given by either DEM frames shown as stills or as a video [(a) below] or the particle paths for consecutive frames (b) or by the position density plots (PDP) (showing the occupancy of any point in the mill by ball centres during a revolution).

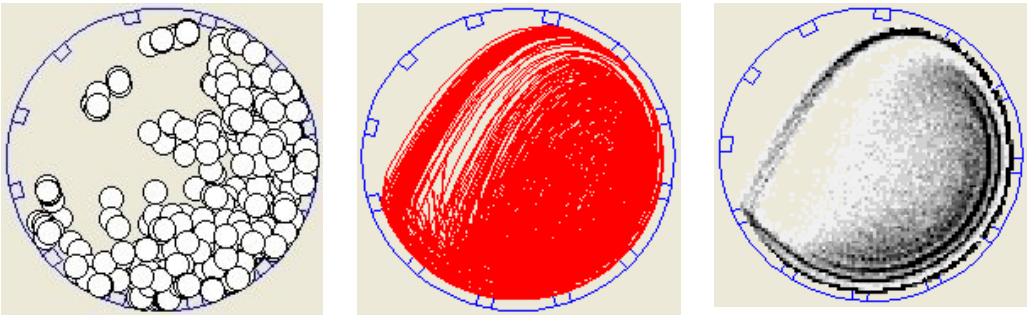


Figure A.1.4 DEM frames, particle paths for consecutive frames, position density plots (PDP) (ball diameter = 30mm)

A.2 Mineralogical data

This section contains data of the UG2 ore sample used in this research work. The UG2 ore sample characterisation was carried out at the mineralogy division of Mintek. The mineralogical content was determined by using modal analysis. This simple technique consists in counting number or measuring surface of mineral occurrence along a series of traverse line across a given thin or polished section of an ore. In order to understand the representation of the distribution and volume percent of PGM grains in an ore sample, it is important to first have a solid understanding of a few basic terms that apply. **Table A.2.1** gives the terminology used at Mintek when discussing such data.

Table A.2.1 Mintek internal mineralogical terms

L	Liberated PGMs
SL	PGMs associated with liberated BMS (Base Metal Sulfides)
SG	PGMs associated with BMS locked in Silicate or Oxide gangue particles
AG	PGMs attached to Silicate or Oxide gangue particles
SAG	PGMs associated with BMS attached to Silicate or Oxide gangue particles
G	PGMs locked within Silicate or Oxide gangue particles

Tables A.2.2 and **A.2.3** show the PGM grains mode of occurrence in the UG2 ore sample, obtained by use of the modal analysis.

Table A.2.2 PGM grains mode of occurrence in the UG2 ore sample

	L	SL	SG	AG	SAG	G
BMS association						
Pentlandite	-	9	6	-	24	-
Chalcopyrite		3	1	-		
Pyrite	-	1	-	-	2	-
Galena	-	-	-	-	1	-
Gangue association						
Plagioclase	-	-	2	5	9	2
Orthopyroxene		-	2	1	12	
Amphibole	-	-	2	3	2	1
Mica	-	-	-	-	2	-
Chromite	-	-	-	1	2	1
Clinopyroxene	-	-	1	1	-	1

Table A.2.3 Volume weight percent of PGM grains mode of occurrence in the UG2 ore sample

Mineral association	PGM Vol. %	PGM grains	PGM grains <3µm ECD
L	55.9	34	2
SL	4.7	13	6
SG	2.5	7	4
AG	9.0	11	5
SAG	26.7	27	15
G	1.2	5	2
	100.0	97	34

A.3 Ball milling test results data

This section contains contain the ball milling test results data that were generated at Mintek. (**Tables A.3.1-3.2**) were obtained from the wet ball milling tests at Mintek with the following conditions: Ball filling J = 30 %, slurry filling U = 75 %, mill speed Nc = 60, 65 and 70 % of critical speed and ball sizes: 20 mm and

30 mm. The specific energy consumption was also varied. The 45° lifters were used.

Table A.3.1a Particle Size Distribution of UG2 ore sample using 30 mm balls

Specific power consumption		5 kWh/t			10 kWh/t		
Size (microns)	Feed	60 % crit.	65% crit.	70 % crit.	60 % crit.	65% crit.	70 % crit.
600	100	100	100	100	100	100	100
425	83.83	100	100	100	100	100	100
300	69.32	100	100	100	100	100	100
212	53.36	99.58	99.46	99.43	99.83	99.89	99.86
150	39.8	95.83	94.75	94.54	97.31	99.41	99
106	28.35	82.26	80.47	80.63	85.68	93.64	92.6
75	23.7	63.37	62.06	62.98	67.9	82.02	83.66
53	16.76	48.18	47.84	48.95	52.33	67.69	69.58
38	12.44	37.82	37.08	38.21	40.67	54.51	55.91
25	2.39	28.79	28.75	29.24	31.73	44.98	46.41

Table A.3.1b Particle Size Distribution of UG2 ore sample using 30 mm balls

Size (microns)	Feed	Specific power consumption				
		3.5 kwh/t	4 kwh/t	5 kwh/t	10 kwh/t	20 kwh/t
600	100.00	100.00	100.00	100.00	100.00	100.00
425	83.83	100.00	100.00	100.00	100.00	100.00
300	69.32	100.00	100.00	100.00	100.00	100.00
212	53.36	98.99	98.70	99.46	99.89	100.00
150	39.80	92.96	93.77	94.75	99.41	99.65
106	28.35	78.46	80.31	80.47	93.64	99.04
75	23.70	61.05	63.85	62.06	82.02	95.74
53	16.76	44.11	47.57	47.84	67.69	83.09
38	12.44	34.48	37.32	37.08	54.51	70.30
25	2.39	25.57	29.02	28.75	44.98	56.05

Table A.3.2a Particle Size Distribution of UG2 ore sample using 20 mm balls

Specific power consumption		5 kWh/t			10 kWh/t		
Size (microns)	Feed	60 % crit.	65% crit.	70 % crit.	60 % crit.	65% crit.	70 % crit.
600	100.00	100.00	100.00	100.00	100.00	100.00	100.00
425	83.83	100.00	100.00	100.00	100.00	100.00	100.00
300	69.32	100.00	100.00	100.00	100.00	100.00	100.00
212	53.36	99.91	99.97	99.97	100.00	99.86	100.00
150	39.80	98.63	99.03	99.14	99.87	99.79	99.99
106	28.35	89.70	90.92	91.67	96.03	98.73	99.84
75	23.70	70.67	72.59	74.79	92.86	91.00	98.80
53	16.76	53.53	55.29	58.13	78.18	76.16	90.98
38	12.44	40.79	42.45	45.18	63.37	62.59	75.08
25	2.39	31.77	33.22	34.67	50.28	53.49	58.74

Table A.3.2b Particle Size Distribution of UG2 ore sample using 20 mm balls

Size (microns)	Feed	Specific power consumption				
		3.5 kwh/t	4 kwh/t	5 kwh/t	10 kwh/t	20 kwh/t
600	100	100.00	100.00	100.00	100.00	100.00
425	83.83	100.00	100.00	100.00	100.00	100.00
300	69.32	100.00	100.00	100.00	100.00	100.00
212	53.36	99.84	100.00	99.91	99.86	100.00
150	39.8	97.87	98.79	98.63	99.79	99.87
106	28.35	87.30	91.00	89.70	98.73	99.48
75	23.7	68.85	75.40	70.67	91.00	98.25
53	16.76	49.34	57.21	53.53	76.16	88.93
38	12.44	37.46	45.00	40.79	62.59	75.38
25	2.39	28.05	34.72	31.77	53.49	60.54

A.4 Milling kinetics data

This section contains contain data that were used to model the milling kinetics. Data on the UG2 sample (**Tables A.4.1-4.2**) were obtained from the wet ball milling tests at Mintek with the following conditions: Ball filling J = 30 %, slurry filling U = 75 %, mill speed Nc = 65 % of critical speed and ball mill provided with 45° lifters. Data on the chromite component (**Tables A.4.3-4.4**) were derived from the UG2 samples by applying model **Eq. (6.7).** Finally, data on the non chromite component (**Tables A.4.5-4.6**) were obtained as a difference between the UG2 sample and the chromite component.

Table A.4.1 Mass percent of UG2 ore using 30 mm balls

sieve (mm)	0.5 min.				20 min.			
	.-600+425	.-425+300	.-300+212	.-212+150	.-600+425	.-425+300	.-300+212	.-212+150
	mass %	mass %	mass %	mass %	mass %	mass %	mass %	mass %
600	0	0	0	0	0	0	0	0
425	63.03	31.53	0	0	0.57	0.27	0	0
300	27.6	13.81	0	0	15.28	7.19	0	0
212	5.09	42.26	79.46	0	22.64	20.68	18.94	0
150	1.96	7.97	13.99	82.06	19.61	21.02	22.28	25.55
106	0.58	1.66	2.74	11.32	12.11	14.65	16.92	21.43
75	0.44	0.83	1.22	2.04	8.47	10.98	13.22	16.48
53	0.11	0.28	0.45	0.58	4.78	6.26	7.57	9.76
38	0.09	0.24	0.4	0.51	3.55	4.65	5.62	7.47
25	0.38	0.49	0.6	1.19	4.77	4.31	3.9	4.59
.-25	0.72	0.93	1.14	2.29	8.24	9.99	11.55	14.72
Total	100	100	100	100	100	100	100	100

Table A.4.2 Mass percent of UG2 ore using 20 mm balls

sieve (mm)	0.5 min.				20 min.			
	.-600+425	.-425+300	.-300+212	.-212+150	.-600+425	.-425+300	.-300+212	.-212+150
	mass %	mass %	mass %	mass %	mass %	mass %	mass %	mass %
600	0	0	0	0	0	0	0	0
425	43.3129	0	0	0	5.90078	0	0	0
300	38.8871	82.2	0	0	2.57963	5.35	0	0
212	5.90826	5.91	79.9	0	10.7833	13.92	11.08	0
150	4.60844	4.61	9.77	85.02	16.7154	16.72	18.26	17.64
106	3.51273	3.51	5.12	8.99	20.6527	20.65	18.16	21.28
75	1.78322	1.78	2.09	1.79	9.48825	9.49	15.46	18.16
53	0.73048	0.73	1.67	0.92	11.0653	11.07	9.14	10.84
38	0.50489	0.5	0.41	0.57	4.05744	4.06	7.04	8.31
25	0.45118	0.45	0.36	0.93	4.37598	4.38	4.91	5.9
.-25	0.30078	0.3	0.68	1.78	14.3812	14.38	15.96	17.88
Total	100	100	100	100	100	100	100	100

Table A.4.3 Mass percent of the chromite component using 30 mm balls

sieve (mm)	0.5 min.				20 min.			
	.-600+425	.-425+300	.-300+212	.-212+150	.-600+425	.-425+300	.-300+212	.-212+150
	mass %	mass %	mass %	mass %	mass %	mass %	mass %	mass %
212	53.75	74.40	76.28	66.35	29.34	24.85	20.99	0.00
150	26.97	18.27	17.50	11.93	27.98	27.57	27.19	32.23
106	8.80	4.24	3.78	2.37	15.68	17.34	18.74	24.54
75	5.45	1.70	1.37	0.55	10.84	12.78	14.47	18.65
53	0.87	0.39	0.32	0.31	4.86	5.79	6.58	8.77
38	0.52	0.23	0.21	0.52	3.08	3.68	4.17	5.73
25	2.05	0.39	0.29	0.94	3.98	3.36	2.78	3.39
.-25	1.60	0.39	0.23	17.03	4.24	4.71	5.08	6.70
Total	100.00	100.00	100.00	100.00	100.00	100.00	100.00	100.00

Table A.4.4 Mass percent of the chromite component using 20 mm balls

sieve (mm)	0.5 min.				20 min.			
	.-600+425	.-425+300	.-300+212	.-212+150	.-600+425	.-425+300	.-300+212	.-212+150
	mass %	mass %	mass %	mass %	mass %	mass %	mass %	mass %
212	30.81	15.41	77.88	0.00	16.21	13.61	10.23	13.24
150	29.16	58.05	11.56	86.93	20.31	18.67	19.26	18.24
106	23.38	16.53	6.38	9.68	21.45	26.09	21.67	17.61
75	10.28	5.98	2.26	1.67	12.63	12.12	18.65	10.63
53	3.10	1.87	1.33	0.63	9.91	12.17	9.49	7.01
38	1.66	0.99	0.25	0.31	4.94	4.17	6.83	4.65
25	1.21	0.81	0.18	0.40	4.48	4.97	5.26	15.57
.-25	0.39	0.39	0.17	0.38	10.10	8.22	8.61	43.88
Total	100.00	100.00	100.00	100.00	100.00	100.00	100.00	100.00

Table A.4.5 Mass percent of the non-chromite component using 30 mm balls

sieve (mm)	0.5 min.				20 min.			
	.-600+425	.-425+300	.-300+212	.-212+150	.-600+425	.-425+300	.-300+212	.-212+150
	mass %	mass %	mass %	mass %	mass %	mass %	mass %	mass %
212	54.40	77.70	79.89	8.97	26.71	22.17	18.81	0.05
150	20.13	14.09	13.52	76.82	22.94	22.37	21.95	25.08
106	5.85	2.87	2.60	10.50	14.29	15.73	16.80	21.21
75	4.60	1.49	1.20	1.88	10.00	11.80	13.14	16.32
53	1.21	0.53	0.47	0.51	5.74	6.83	7.64	9.83
38	1.02	0.48	0.43	0.42	4.31	5.12	5.71	7.58
25	4.32	0.96	0.64	1.01	5.79	4.75	3.98	4.67
.-25	8.48	1.88	1.26	0.11	10.21	11.22	11.98	15.26
Total	100.00	100.00	100.00	100.00	100.00	100.00	100.00	100.00

Table A.4.6 Mass percent of the non-chromite component using 20 mm balls

sieve (mm)	0.5 min.				20 min.			
	.-600+425	.-425+300	.-300+212	.-212+150	.-600+425	.-425+300	.-300+212	.-212+150
	mass %	mass %	mass %	mass %	mass %	mass %	mass %	mass %
212	26.67	33.60	80.21	0.12	12.24	14.78	11.13	6.77
150	24.96	25.33	9.50	84.58	14.12	17.59	18.21	16.63
106	19.20	19.11	4.93	8.86	17.96	21.53	17.97	20.38
75	10.03	9.97	2.07	1.81	11.36	9.88	15.28	17.71
53	4.27	4.28	1.72	0.97	13.39	11.66	9.12	10.52
38	10.17	3.04	0.43	0.62	7.64	4.29	7.05	8.12
25	2.77	2.76	0.38	1.02	5.28	4.60	4.89	4.87
.-25	1.92	1.91	0.76	2.03	18.01	15.67	16.36	15.00
Total	100.00	100.00	100.00	100.00	100.00	100.00	100.00	100.00

A.5 Matrix data

This section contains the key matrices that were used to check the validity of the closed circuit mill-cyclone model of a binary material. The matrices were of **20X20** dimensions. The upper half of matrices represents the chromite component, and the lower half of matrices represents the non-chromite component.

Table A.5.1 Binary Selection Function Matrix **S**

[I,j]	1	2	3	4	5	6	7	8	9	10	11	12	13	14	15	16	17	18	19	20
1	0.134		0	0	0	0	0	0	0	0	0	0	0	0	0	0	0	0	0	0
2	0	0.086	0	0	0	0	0	0	0	0	0	0	0	0	0	0	0	0	0	0
3	0	0	0.055	0	0	0	0	0	0	0	0	0	0	0	0	0	0	0	0	0
4	0	0	0	0.0337	0	0	0	0	0	0	0	0	0	0	0	0	0	0	0	0
5	0	0	0	0	0.0210	0	0	0	0	0	0	0	0	0	0	0	0	0	0	0
6	0	0	0	0	0	0.0131	0	0	0	0	0	0	0	0	0	0	0	0	0	0
7	0	0	0	0	0	0	0.0082	0	0	0	0	0	0	0	0	0	0	0	0	0
8	0	0	0	0	0	0	0	0.0056	0	0	0	0	0	0	0	0	0	0	0	0
9	0	0	0	0	0	0	0	0	0.0029	0	0	0	0	0	0	0	0	0	0	0
10	0	0	0	0	0	0	0	0	0	0.0019	0	0	0	0	0	0	0	0	0	0
11	0	0	0	0	0	0	0	0	0	0	0.121	0	0	0	0	0	0	0	0	0
12	0	0	0	0	0	0	0	0	0	0	0	0.076		0	0	0	0	0	0	0
13	0	0	0	0	0	0	0	0	0	0	0	0	0.0490	0	0	0	0	0	0	0
14	0	0	0	0	0	0	0	0	0	0	0	0	0	0.0295	0	0	0	0	0	0
15	0	0	0	0	0	0	0	0	0	0	0	0	0	0	0.0182	0	0	0	0	0
16	0	0	0	0	0	0	0	0	0	0	0	0	0	0	0	0.0112	0	0	0	0
17	0	0	0	0	0	0	0	0	0	0	0	0	0	0	0	0	0.0069	0	0	0
18	0	0	0	0	0	0	0	0	0	0	0	0	0	0	0	0	0	0.0490	0	0
19	0	0	0	0	0	0	0	0	0	0	0	0	0	0	0	0	0	0	0.0024	0
20	0	0	0	0	0	0	0	0	0	0	0	0	0	0	0	0	0	0	0	0.0015

Table A.5.2 Binary Breakage Function Matrix **B**

[I,j]	1	2	3	4	5	6	7	8	9	10	11	12	13	14	15	16	17	18	19	20
1	0	0	0	0	0	0	0	0	0	0	0	0	0	0	0	0	0	0	0	0
2	0.5301	0	0	0	0	0	0	0	0	0	0	0	0	0	0	0	0	0	0	0
3	0.2819	0.5319	0	0	0	0	0	0	0	0	0	0	0	0	0	0	0	0	0	0
4	0.1507	0.2843	0.5346	0	0	0	0	0	0	0	0	0	0	0	0	0	0	0	0	0
5	0.0808	0.1525	0.2867	0.5363	0	0	0	0	0	0	0	0	0	0	0	0	0	0	0	0
6	0.0433	0.0816	0.1534	0.2870	0.5352	0	0	0	0	0	0	0	0	0	0	0	0	0	0	0
7	0.0232	0.0438	0.0823	0.1540	0.2871	0.5365	0	0	0	0	0	0	0	0	0	0	0	0	0	0
8	0.0124	0.0234	0.0441	0.0824	0.1537	0.2872	0.5353	0	0	0	0	0	0	0	0	0	0	0	0	0
9	0.0068	0.0129	0.0242	0.0453	0.0844	0.1578	0.2941	0.5494	0	0	0	0	0	0	0	0	0	0	0	0
10	0.0031	0.0058	0.0109	0.0205	0.0381	0.0713	0.1328	0.2481	0.4516	0	0	0	0	0	0	0	0	0	0	0
11	0	0	0	0	0	0	0	0	0	0	0	0	0	0	0	0	0	0	0	0
12	0	0	0	0	0	0	0	0	0	0	0.5176	0	0	0	0	0	0	0	0	0
13	0	0	0	0	0	0	0	0	0	0	0.2732	0.5279	0	0	0	0	0	0	0	0
14	0	0	0	0	0	0	0	0	0	0	0.1457	0.2815	0.5333	0	0	0	0	0	0	0
15	0	0	0	0	0	0	0	0	0	0	0.0781	0.1509	0.2858	0.5359	0	0	0	0	0	0
16	0	0	0	0	0	0	0	0	0	0	0.0418	0.0807	0.1529	0.2868	0.5351	0	0	0	0	0
17	0	0	0	0	0	0	0	0	0	0	0.0224	0.0433	0.0820	0.1538	0.2870	0.5364	0	0	0	0
18	0	0	0	0	0	0	0	0	0	0	0.0120	0.0232	0.0439	0.0823	0.1536	0.2871	0.5353	0	0	0
19	0	0	0	0	0	0	0	0	0	0	0.0066	0.0127	0.0241	0.0452	0.0844	0.1578	0.2941	0.5494	0	0
20	0	0	0	0	0	0	0	0	0	0	0.0033	0.0064	0.0121	0.0226	0.0422	0.0789	0.1470	0.2747	0.5	0

Table A.5.3 Binary Partition Curve Coefficients Matrix **C**

[I,j]	1	2	3	4	5	6	7	8	9	10	11	12	13	14	15	16	17	18	19	20
1	1	0	0	0	0	0	0	0	0	0	0	0	0	0	0	0	0	0	0	0
2	0	1	0	0	0	0	0	0	0	0	0	0	0	0	0	0	0	0	0	0
3	0	0	1	0	0	0	0	0	0	0	0	0	0	0	0	0	0	0	0	0
4	0	0	0	0.99995	0	0	0	0	0	0	0	0	0	0	0	0	0	0	0	0
5	0	0	0	0	0.9915	0	0	0	0	0	0	0	0	0	0	0	0	0	0	0
6	0	0	0	0	0	0.9075	0	0	0	0	0	0	0	0	0	0	0	0	0	0
7	0	0	0	0	0	0	0.717111	0	0	0	0	0	0	0	0	0	0	0	0	0
8	0	0	0	0	0	0	0	0.530757	0	0	0	0	0	0	0	0	0	0	0	0
9	0	0	0	0	0	0	0	0	0.377712	0	0	0	0	0	0	0	0	0	0	0
10	0	0	0	0	0	0	0	0	0	0.279859	0	0	0	0	0	0	0	0	0	0
11	0	0	0	0	0	0	0	0	0	0	1	0	0	0	0	0	0	0	0	0
12	0	0	0	0	0	0	0	0	0	0	0	1	0	0	0	0	0	0	0	0
13	0	0	0	0	0	0	0	0	0	0	0	0	1	0	0	0	0	0	0	0
14	0	0	0	0	0	0	0	0	0	0	0	0	0	0.999683	0	0	0	0	0	0
15	0	0	0	0	0	0	0	0	0	0	0	0	0	0	0.979907	0	0	0	0	0
16	0	0	0	0	0	0	0	0	0	0	0	0	0	0	0	0.861744	0	0	0	0
17	0	0	0	0	0	0	0	0	0	0	0	0	0	0	0	0	0.658861	0	0	0
18	0	0	0	0	0	0	0	0	0	0	0	0	0	0	0	0	0	0.486539	0	0
19	0	0	0	0	0	0	0	0	0	0	0	0	0	0	0	0	0	0	0.355	0
20	0	0	0	0	0	0	0	0	0	0	0	0	0	0	0	0	0	0	0	0.274219

A.6 Cumulative weight percents of grinding circuit streams

This section comprises the cumulative weight percents vectors that were derived using the grinding circuit matrix model. These vectors are of **20X1** dimension. The first 10 elements are of the chromite component, and the ten last elements are of the non-chromite component.

Table A.6.1 Cumulative weight percents of grinding circuit streams

Size (microns)	Fresh Feed	Mill Feed	Mill Discharge	O' Flow	U' Flow
425	**0.07**	**0.06**	**0.04**	**0**	**0.06**
300	**0.57**	**0.60**	**0.5**	**0**	**0.61**
212	**1.76**	**2.10**	**1.93**	**0**	**2.20**
150	**3.13**	**4.14**	**4.16**	**0**	**4.44**
106	**3.27**	**4.44**	**4.57**	**0.14**	**4.79**
75	**2.50**	**3.01**	**3.03**	**1.08**	**3.16**
53	**1.42**	**1.21**	**1.01**	**1.51**	**1.14**
38	**1.06**	**0.73**	**0.63**	**1.87**	**0.63**
25	**0.72**	**0.39**	**0.32**	**1.61**	**0.29**
-25	**1.76**	**0.91**	**1.14**	**5.67**	**0.66**
425	**0.99**	**0.92**	**0.67**	**0**	**0.9**
300	**4.64**	**5.00**	**4.23**	**0**	**5.11**
212	**8.98**	**10.6**	**9.71**	**0**	**11.08**
150	**11.64**	**15.03**	**14.87**	**0.02**	**16.05**
106	**12.76**	**17.52**	**18.51**	**1.30**	**18.95**
75	**10.07**	**11.8**	**12.24**	**6.60**	**12.32**
53	**8.58**	**7.82**	**8.2**	**13.14**	**7.59**
38	**6.94**	**3.98**	**3.03**	**10.9**	**3.09**
25	**5.15**	**2.59**	**2.18**	**11.03**	**1.82**
-25	**13.99**	**7.15**	**9.02**	**45.13**	**5.10**
Total	**100**	**100**	**100**	**100**	**100**